

Gauge Boson Coupling Measurements in Final
States with a W Boson Produced with Additional
Photons using The ATLAS Detector

by

Miaoyuan Liu

Department of Physics
Duke University

Date: _____

Approved:

Alfred T.Goshaw, Supervisor

Steffen Bass

Glenn Edwards

Ashutosh Kotwal

Chris Walter

Dissertation submitted in partial fulfillment of the requirements for the degree of
Doctor of Philosophy in the Department of Physics
in the Graduate School of Duke University
2015

ABSTRACT

Gauge Boson Coupling Measurements in Final States with a W Boson Produced with Additional Photons using The ATLAS Detector

by

Miaoyuan Liu

Department of Physics
Duke University

Date: _____
Approved:

Alfred T.Goshaw, Supervisor

Steffen Bass

Glenn Edwards

Ashutosh Kotwal

Chris Walter

An abstract of a dissertation submitted in partial fulfillment of the requirements for
the degree of Doctor of Philosophy in the Department of Physics
in the Graduate School of Duke University
2015

Copyright © 2015 by Miaoyuan Liu
All rights reserved except the rights granted by the
Creative Commons Attribution-Noncommercial Licence

Abstract

This thesis presents a first measurement of triple gauge boson production $pp \rightarrow W(l\nu)\gamma\gamma + X$ with the ATLAS experiment at the LHC. A dataset collected from proton-proton collisions during 2012 is used for this study, corresponding to an integrated luminosity of 20.3 fb^{-1} . The measured cross section is compared to the most precise Standard Model predictions available and is used to set limits on anomalous quartic gauge couplings. Sensitivity studies are also presented for $W\gamma$ events produced in vector boson scattering. Results show a promising first observation of this Standard Model electroweak process with the pp collision dataset collected by the ATLAS experiment during 2012.

Contents

Abstract	iv
List of Tables	x
List of Figures	xiv
Acknowledgements	xxi
1 Introduction	1
2 Theory and Motivation	3
2.1 Introduction to the Standard Model	4
2.2 Electroweak sector and Gauge boson couplings	6
2.3 Anomalous gauge boson coupling	9
2.3.1 Overview	9
2.3.2 Parametrization of anomalous couplings	10
2.3.3 Unitarization procedure	14
2.4 $W\gamma\gamma$ production and vector boson scattering $W\gamma$	16
2.5 Monte–Carlo Event Generation	21
2.6 Summary	23
3 The LHC and the ATLAS experiment	25
3.1 Introduction to the LHC	26
3.2 Introduction to the ATLAS detector	31
3.2.1 Inner detector	31

3.2.2	Calorimeters	34
3.2.3	Muon system	38
3.2.4	Triggering system	39
3.3	Particle detection with the ATLAS detector	40
3.3.1	Reconstruction and identification of electrons and photons . .	41
3.4	Status and future plans for the LHC and ATLAS detector	46
4	The ATLAS Inner Tracker Monitoring and Upgrade	48
4.1	Description of the transition radiation tracker	49
4.1.1	Detection of charged particles with the TRT	49
4.1.2	Detector layout and gas mixture	51
4.2	Monitoring the performance of the TRT	54
4.2.1	Aging and other performance issues	54
4.2.2	Methods for monitoring the TRT	54
4.2.3	Summary of wire aging studies	61
4.2.4	Monitoring the TRT in future LHC runs	62
4.3	Plans for the replacing the ATLAS Inner Detector in Phase 2 upgrade	64
4.3.1	ATLAS Inner Tracker for HL-LHC	65
4.3.2	Particle detection with silicon strips	65
4.3.3	Tests of silicon strip tracker components	68
4.4	Summary	80
5	Measurement of $pp \rightarrow W\gamma\gamma + X$ Production	81
5.1	Data and Simulated samples	82
5.2	Event Selection	82
5.2.1	Event quality requirements	82
5.2.2	Triggering and object definitions	83

5.2.3	Kinematic cuts	88
5.3	$W\gamma\gamma$ Signal Extraction	93
5.3.1	Candidate events	93
5.3.2	Data-driven background estimation for fake photons and fake electrons	94
5.4	Summary of the measured $pp \rightarrow W(e\nu)\gamma\gamma + X$ signal	102
6	Interpretation of $pp \rightarrow W\gamma\gamma + X$ Measurement Results	109
6.1	Cross section measurement	110
6.1.1	Fiducial Region Definition	110
6.1.2	Acceptance and Efficiency	111
6.1.3	The Fiducial Cross-Section Measurement	113
6.1.4	Comparison to the SM theory prediction	117
6.2	Anomalous quartic coupling (aQGC) analysis	121
6.2.1	Limits extraction procedure	121
6.2.2	Unitarity constraint	124
6.2.3	Results	125
6.2.4	Comparison to other experiments	125
6.3	Results and Conclusions	129
7	Analysis of $W(e\nu) + \gamma$ Produced via Vector Boson Scattering in pp collisions	130
7.1	Analysis strategy	131
7.2	Event Selection and Signal Region Definitions	132
7.3	Background analysis	134
7.3.1	Inclusive selection of $W(e\nu)\gamma$	136
7.3.2	2 jet region of $W(e\nu)\gamma$	137
7.3.3	VBS region of $W(e\nu)\gamma$	138

7.4	Summary of the Event Yield	139
7.5	Conclusions and plans	140
8	Conclusions	142
A	Experimental data-driven methods	144
A.1	Tag and Probe method	144
A.1.1	General Method	144
A.1.2	Trigger efficiency in $W\gamma\gamma$	145
A.2	ABCD method	145
A.2.1	General Formunilam	145
A.2.2	Jet faking electrons in $W\gamma\gamma$	147
A.2.3	Jet faking electron and photon background in Vector Boson Scattering $W\gamma$	152
A.3	2D Template Fit Method	154
A.3.1	General Method	154
A.3.2	Template Determination	154
A.3.3	Signal-Leakage Corrections	154
A.3.4	Template Fit Method Results	158
A.3.5	Statistical Uncertainties Estimate	160
A.3.6	Systematic Uncertainties Estimate	163
A.3.7	Background Extrapolation for the Exclusive Selection in the Electron Channel	166
B	More on the interpretation of the measured $pp \rightarrow W\gamma\gamma + X$ results	168
B.1	Correction factors	168
B.1.1	Statistical Uncertainty of the Correction Factor	168
B.1.2	Systematic Uncertainty on Correction Factors	170
B.1.3	Statistical error on the systematic uncertainty	173

B.2 aQGC analysis	174
B.2.1 aQGC region optimization	174
B.2.2 Correction Factor for different aQGC scenarios	174
C TRT aging monitoring plots	177
D Event selection table for $W\gamma\gamma$ analysis	180
Bibliography	181
Biography	187

List of Tables

3.1	The main parameters of the inner detector. $r \times \Delta\phi$ is the transverse plane.	34
4.1	The aging parameters (10^{-5}) for runs with low instantaneous luminosity and runs with high instantaneous luminosity from Period B.	61
5.1	Results of the 2D template fit method using the inclusive event selection. For each category the result of the fit and the event yield is given. The yield column is the fitted normalizations for each component and the yield in signal region is the integrals in the isolated photon regions. The uncertainties are statistical only.	98
5.2	Expected number of background events in the electron channel with one real and one fake photon, two fake photons, and for the total fake photons background. $\gamma - jet$ category contains events with $p_T^\gamma > p_T^{jet}$, while it is the opposite for $jet - \gamma$	100
5.3	Number of candidate events in data passing the full selection of Section 5.2 in the electron and muon channels for the inclusive case. The number of background events from misidentified photons and leptons, as estimated from data, and from MC derived backgrounds are also shown. The subtraction of these backgrounds yields the measured signal in each channel, with statistical and systematic uncertainties.	103
5.4	Number of candidate events in data passing the full selection of Section 5.2 in the electron and muon channels for the exclusive case. The number of background events from misidentified photons and leptons, as estimated from data, and from MC derived backgrounds are also shown. The subtraction of these backgrounds yields the measured signal in each channel, with statistical and systematic uncertainties.	104
6.1	Definition of the fiducial region where the cross-section is evaluated. p_T^ν is the transverse momentum of the neutrino coming from the W decay. The jet veto is only applied in the exclusive selection.	111

6.2	Correction factor for the inclusive and the exclusive selection along with their statistical and relative systematic uncertainty in the electron channel. The statistical uncertainty on the systematic component is also given for completeness.	113
6.3	Fiducial cross-section measurements of the $pp \rightarrow l\nu\gamma\gamma$ process for two isolated photons with $p_T > 20$ GeV.	116
6.4	Parton to particle level correction factors $T_{N_{\text{jet}}}$ and $T_{\gamma_{\text{iso}}}$ for the different signal regions as obtained from SHERPA, and ALPGEN MC. In the upper part of the Table, only statistical errors are quoted. The lower part shows the SM parton to particle level correction factor averaged over both lepton flavours. SHERPA is used as the baseline and the deviation from ALPGEN is quoted as the systematic uncertainty.	119
6.5	Comparison of the cross-section measurements of the $pp \rightarrow l\nu\gamma\gamma$ process with the MCFM SM NLO predictions.	120
6.6	Expected and observed 95% limits obtained analyzing the full 2012 data sample for the f_{M2} , f_{M3} and f_{T0} aQGC parameters in each of the two decay channels studied and for the combination of the two.	126
7.1	Number of candidate events in the electron channel for the inclusive, 2 jet and VBS categories. The number of background events with misidentified photons and leptons, estimated from data driven techniques, and other backgrounds from simulated samples are also shown. Row ' $N_{\text{data}} - N_{\text{bkg}}$ ' shows the sum of $W\gamma$ QCD and $W\gamma$ VBS events. Number of $W\gamma$ QCD events in VBS region is given by Monte Carlo full simulated sample generated by SHERPA 1.3.1. The uncertainty is statistical only.	139
A.1	Definition of signal (A) and control regions (B, C, D) using electron isolation, missing transverse energy, transverse mass and total transverse momentum requirements. The track quality requirements are relaxed for non-isolated control region B and C to increase statistics in these regions. The electron calo strip and EM calorimeter track matching variables are inverted to suppress the $Z\gamma$ background in low M_T and low E_T^{miss} or low p_T^{tot} control region (C, D) in which this background is dominant	149
A.2	The number of observed events in data and the contribution from EW processes with real electron (N^{EW}) predicted by MC simulation in control region A, B, C and D. The MC estimations are normalized to the process cross section and luminosity.	149

A.3	Signal leakage parameters used to calculate the fake-electron background.	150
A.4	Results of the fake-electron background estimation with the ABCD method for several different choices of the control region definitions. The deviation is taken as an systematic uncertainty on the nominal value.	150
A.5	Breakdown of the size of the systematic uncertainties affecting the fake-electron background estimation for the inclusive and exclusive selection.	151
A.6	Control region definitions for jet faking photons. non-isolated region is defined by reversing photon isolation cut, i.e. $Iso > 6GeV$, non-tight region is defined the same way by requiring a non-tight photon passing the requirement in Chapter 5 in the event.	152
A.7	Control region definitions for electron faking photons. non-isolated region is defined by reversing electron isolation cut, i.e. $Iso/p_T > 0.1$, low-MET regions is defined to be : $MET < 20GeV, M_T < 20GeV$. .	152
A.8	The event counts in signal and control regions for different processes from data and Monte Carlo simulated samples. Monte Carlo closure tests and signal leakage parameters as well as the results from ABCD data driven method.	153
A.9	Input for the signal leakage correction derived from $W\gamma\gamma$ MC using the inclusive selection. The uncertainties shown are statistical only. .	156
A.10	Inputs for Monte Carlo for signal leakage correction derived from $W\gamma +$ jets MC using the inclusive selection. The uncertainties shown are statistical only.	156
A.11	Number of events in the control regions used for the calculation of the signal-leakage corrections.	157
A.12	Results of the 2D fit method using the inclusive selection. For each category the result of the fit and the event yield is given. The uncertainties are statistical only. Details on how the statistical uncertainties are obtained can be found in Section A.3.5.	158

A.13 Results of the 2D fit method using the exclusive selection. For each category the result of the fit and the event yield is given. The uncertainties are statistical only. Details on how the statistical uncertainties are obtained can be found in Section A.3.5. The results for the electron channel is extrapolated from the N_{jet} distribution as described in Section A.3.7.	158
A.14 Systematic uncertainties for the electron channel using the inclusive selection.	166
A.15 The result of the fake-photon background estimation using the exclusive selection in the electron channel. For each background category the estimated number of events and its statistical and systematic uncertainty is given. The numbers are obtained by using the zero-jet bin of the N_{jet} distribution obtained from data (see text).	167
B.1 Correction factor for the inclusive and the exclusive selection along with their statistical and relative systematic uncertainty in the muon channel.	169
B.2 Correction factor for the inclusive and the exclusive selection along with their statistical and relative systematic uncertainty in the electron channel.	169
B.3 Expected 95% CL limits on f_{M2} and f_{M3} using different signal regions defined by lower diphoton invariant mass ($M_{\gamma\gamma}$) cuts. The numbers in parentheses are the lower and upper limits. The limits converge to minimum values starting from 300 GeV.	175
B.4 Correction factor $A \times C$ for the inclusive and the exclusive electron selection for different points in the (aQGC) phase space.	175
B.5 Correction factor $A \times C$ for the inclusive and the exclusive muon selection for different points in the (aQGC) phase space.	176
D.1 The number of events after each selection step for the electron channel is shown. This is performed on a data set collected from period B, corresponding to an integrated luminosity of 5.3 fb^{-1} . A filtered sample is used. It is a subset of the whole dataset which has 116070903 events in total.	180

List of Figures

2.1	The Standard Model	4
2.2	Gauge boson couplings in the SM EWK sector. (a) WWA ,(b) WWZ ,(c) $WWWW$, (d) $WWZZ$, (e) $WWAA$,(f) $WWZA$	10
2.3	Illustrations of the topologies of the final states used to test gauge boson couplings : (a) $W\gamma$ final state to test the $WW\gamma$ vertex, (b) vector boson fusion W production to test $WW(Z\gamma)$ vertex. (c) $W\gamma\gamma$ final state to test $WW\gamma\gamma$ final state, (d) Vector boson scattering $Z\gamma$ final state to test $WWZ\gamma$ final state.	11
2.4	A heavy boson X contributes to TGC at one loop level as shown on the right and QGC at tree level on the left.	14
2.5	Argand circle is shown on the left. In the right plot, ν is the electroweak scale defined as $(\sqrt{2}G_F)^{-1/2} = 246$ GeV. It shows the saturation of WW vector boson scattering amplitude \mathcal{A}_K due to K-matrix unitarization.	15
2.6	Main contributions to the $W\gamma\gamma$ final state. In general, the final state photons can come from: the final state radiation, the initial state radiation, the fragmentation of an initial state quark or gluon, a TGC vertex or a QGC vertex. [1]	17
2.7	K factor as a function of the invariant mass of the di-photon system. Vetoed calculation veto events with an additional hadronic jet with $Pt > 50$ GeV [2]	18
2.8	QGC $WWZ\gamma$ and $WW\gamma\gamma$ contributes to $W\gamma$ produced in vector boson scattering.	19

2.9 Sherpa collision simulation. Sketch of a proton proton collision at high energy. In the upper hemi-sphere of the figure partons from the initial protons (large green ellipses) radiate gluons and finally interact in the hard interaction (red blob). The products of the hard interaction produce a parton shower (in red) which then hadronizes (the green blobs are hadrons) which then decay into the final state particles, all shown as small green blobs. The lower hemisphere of the figure depicts the underlying event, starting from some gluons radiated off the protons, which also produce a parton shower (purple). The beam remnants (blue blob) are considered part of the underlying event. Photon radiation occurs at all stages in the event generation (indicated as yellow lines)	22
3.1 The LHC Accelerator Complex	29
3.2 The peak instantaneous luminosity delivered to ATLAS per day versus time during the p-p runs of 2010, 2011 and 2012.	30
3.3 Integrated luminosity in 2011 and 2012	30
3.4 The ATLAS detector	32
3.5 The inner detector of the ATLAS detector	35
3.6 The Calorimeter system of the ATLAS detector	36
3.7 The Electromagnetic calorimeter in the ATLAS detector	37
3.8 Muon systems in the ATLAS detector	38
3.9 Trigger systems in the ATLAS detector	40
3.10 Electron reconstruction efficiency as a functions of η and E_T . Open circles are results from Monte Carlo simulations, Solid markers are estimated from data using a "Tag and Probe" method described in appendix.	42
3.11 The fraction of high threshold TRT hits	43
3.12 Electron identification efficiency as a functions of E_T for the LikeLyHood(LH) method is shown. Open circles are results from Monte Carlo simulated electrons, Solid markers are measurements from data using a "Tag and Probe" method described in appendix.	44
3.13 Photon identification efficiency as a functions of E_T for converted (top) and unconverted (bottom) photons. Results are measured from $Z \rightarrow ll\gamma$ events using a "Tag and Probe" method described in appendix.	45

3.14 Plan for LHC evolution in the next 10 years. LS stands for 'Long Shutdown'	46
4.1 A cross section view of the straws to show signal detection in the TRT.	50
4.2 Turn-on of Transition Radiation from Muons measured in the ATLAS Barrel TRT (Oct'2008). Most of the particles produced at the LHC lie in an energy range of 500 MeV to 100 GeV. With the equation of $E = m\gamma$, pions have gamma factors in the range of [10,10 ³] while a 500 MeV electron has a gamma factor of 10 ³	52
4.3 Left: X-Y Slice of the TRT Barrel. Phi modules with gas flow coming in from Side A is shown as black blocks. Right:A diagram of the gas flow in End-cap A.	53
4.4 HT_{ratio} as a function of hit z position in the TRT barrel detector for Period E 2012 data. On the left is input A and on the right is input C. Layer 2 is shown as an example here.	56
4.5 The relative change ($\Delta HT_{ratio} / (2 \times \text{ave } HT_{ratio})$) for Period E 2012 Data for Layer 2	56
4.6 HT_{ratio} as a function of hit r for Period E 2012 Data end-cap A (left) end-cap C (right).	58
4.7 $\Delta HT_{ratio} / (2 \times \text{average } HT_{ratio})$ for Period E 2012 Data in end-cap A. The left plot is for type-A wheels and the right plot is for type-B wheels.	58
4.8 Ozone accumulation effect for the Barrel. The increase in the slope value indicates a decrease in the HT_{ratio} along the gas flow direction due to the gas gain drop caused by ozone accumulation. The accumulation stabilizes later in the run.	60
4.9 Fitted slopes as a function of μ for Period E 2012 Data for the barrel	61
4.10 Ozone accumulation for runs with different instantaneous luminosity for period B 2012. Dashed (Solid) lines are for runs with low (high) instantaneous luminosity.	62
4.11 Aging monitoring study on data taken in 2012, plotted as a function of integrated luminosity. The top plot is for the barrel and the bottom left (right) is for wheel-type A (B).	63
4.12 Aging monitoring study for data from the beginning of each run of 2012. The left (right) plot is for the barrel (end-cap).	63
4.13 Baseline layout of new ATLAS inner tracker (active areas) for HL-LHC.	66

4.14	Shortened version of full stave, "stavelet". The stavelet width is 12 cm.	66
4.15	A silicon strip sensor.	67
4.16	Test system for a single module at CERN.	69
4.17	Strobe delay versus efficiency for two adjacent chips.	70
4.18	Threshold scan. The threshold scan as a function of the channel number and the threshold scan for a single channel are shown.	71
4.19	Three point gain test.	73
4.20	ENC result for one hybrid from the 3 point gain tests.	74
4.21	Response curve measurement result for one chip.	75
4.22	Noise injection to the cooling pipe test.	76
4.23	Test system for a stavelet.	76
4.24	Diagram of the CO ₂ cooling system.	77
4.25	CO ₂ cooling system.	77
4.26	The thermodynamic cycle of the CO ₂ cooling system.	78
4.27	Test results for CO ₂ cooling system, two sensors were used in the test, one located at the end where the cooling pipe enters the box (outside), the other one located at the other end (inside) where the cooling pipe goes out of the box. T stands for temperature and H stands for Humidity.	79
5.1	Invariant mass of electron and leading photon (top left), electron and sub-leading photon (top right), electron and two photons (bottom left), and total vector sum of transverse momentum of electron and two photons (bottom right). Events shaded in the box are rejected.	91
5.2	Optimization of the total vector sum of the transverse momentum of electron and two photons. The chosen lower cut is at 30 GeV. The right plot shows the percentage of events which survived the p_T^{tot} cut.	92

5.3	An event display of selected $W(e\nu)\gamma\gamma$ candidate. Photons are yellow, electrons are green and their electromagnetic showers are in red in the plot. Missing transverse energy is shown as red line. The left plot is a x - y plane cross section view, the upright plot is a log plot in η - ϕ space with the p_T shown in z coordinate. The lower right is a plot of the cross section view across the center of the detector, parallel to the beam line (η - z plane).	93
5.4	The E_T^{iso} distribution for the leading (left) and subleading (right) photon from simulated $W\gamma\gamma$ events using the inclusive selection are shown as black dots. The fitted photon isolation PDFs $F_{\gamma,1}(E_T^{\text{iso}1})$ and $F_{\gamma,2}(E_T^{\text{iso}2})$ are shown as solid lines.	96
5.5	The jet E_T^{iso} distribution for the leading (left) and subleading (right) photon candidate from the data using the inclusive selection are shown as black dots. The fitted PDFs $F_{j,1}$ and $F_{j,2}$ are shown as solid lines.	97
5.6	The two-dimensional E_T^{iso} distribution for the jj -PDF determined using the inclusive event selection. Left: $(E_T^{\text{iso}1}, E_T^{\text{iso}2})$ distribution in the $\tilde{\mathbf{T}}\tilde{\mathbf{T}}$ sample. Right: Corresponding smoothed PDF F_{jj}	98
5.7	Projection of the two-dimensional isolation distributions onto the transverse isolation energy of the leading (left) and subleading (right) photon candidates. The black line shows the result of the final fit and the colored lines show the different components.	99
5.8	A sketch presentation of the signal region (A) and three control regions (B, C and D) used the ABCD method. Region A contains events with an isolated electron and high E_T^{miss} , region B has the requirement on electron isolation reversed, region C has the requirement on variables related to E_T^{miss} reversed, while region D has both requirements reversed.	101
5.9	Leading photon E_T (left), Eta(middle), Isolation(right) distributions in the electron channel obtained with the inclusive selection. The $W\gamma j + Wj\gamma + Wjj$ -label denotes the fake photon background component and the fake lepton component is labelled “ $\gamma\gamma + \text{jet}$ ”. The $t\bar{t}$, $W(\rightarrow \tau\nu)\gamma\gamma$ and diboson (WW, WZ)contributions are combined and labelled as “Other”. The hashed areas show the total uncertainty on the background estimate.	106
5.10	Subleading photon E_T (left), η (middle), Isolation(right) distributions in the electron channel obtained with the inclusive selection.	106

5.11	Leading electron p_T (left), η (right) distributions in the electron channel obtained by using the inclusive selection.	107
5.12	ΔR between leading and subleading p_T photons(left) and diphoton invariant mass distribution(right) in the electron channel.	107
5.13	Missing transverse energy (left) and W transverse mass distribution(right) in the electron channel obtained by using the inclusive selection.	108
5.14	Number of jets distribution for the electron channel obtained by using the inclusive selection.	108
6.1	Cross-section and parabolic fit as a function of the coupling for the three operators F_{M2} , F_{M3} and F_{T0} . The parameters and goodness of the fit are given in the graphs.	126
6.2	Comparison of the 95 % exclusion limits on f_{M2} , f_{M3} and f_{T0} obtained from different measurements.	127
7.1	Vector boson scattering producing $W\gamma$ events.	131
7.2	Optimization of the VBS region. Significance is defined as S/\sqrt{B} , where S is the number of signal events predicted by the Monte Carlo simulated samples, B is the sum of the backgrounds taken from Monte Carlo simulation or data driven methods. It is calculated for different M_{jj} and dY_{jj} sets of cuts.	134
7.3	Pt balance distributions of $W(e\nu)\gamma$ VBS, $W(e\nu)\gamma$ QCD events after requiring $M_{jj} > 600$ GeV, $dY_{jj} > 2$. A selection cut for VBS events is applied at pt balance < 0.1	135
7.4	Distribution of number of jets for selected inclusive $W(e\nu)\gamma$ candidates. 'DD' stands for data driven.	138
7.5	Selected kinematic distributions of VBS $W\gamma$ events with $M_{jj} > 600$ GeV, $dY_{jj} > 2$ and pt balance < 0.1 imposed. Backgrounds with misidentified photons and leptons are estimated from data driven techniques and are labeled as 'DD' in the legend. Other backgrounds are taken from simulated samples. Electron p_T (first row, left), missing transverse energy (first row, right), transverse mass of the W boson (second row, left), photon p_T (second row, right) and M_{jj} (bottom) distributions are shown.	141

A.1	Projection of the two-dimensional isolation distributions on the transverse isolation energy of the leading (left) and subleading (right) photon candidate for the muon channel (top) and the electron channel (bottom). The black dots represent the data selected using the inclusive selection. The black line shows the result of the fit and the colored lines show the different components.	159
A.2	Projection of the two-dimensional isolation distributions on the transverse isolation energy of the leading (left) and subleading (right) photon candidate for the muon channel. The black dots represent the data selected using the exclusive selection. The black line shows the result of the fit and the colored lines show the different components. The results for the electron channel is extrapolated from the N_{jet} distribution as described in Section A.3.7..	160
A.3	Pull distributions for the four event yields in the signal region from 10000 pseudo-experiments. In addition the mean, width and goodness-of-fit of a gaussian fitted to these distributions is shown.	162
A.4	Pull distributions from pseudo-experiments used to evaluate the systematic uncertainty due to limited control region statistics. The results are shown for the muon (a–d) and electron (e–h) channel using the inclusive selection.	164
C.1	The relative change ($\Delta HT_{ratio} / (2 \times \text{ave } HT_{ratio})$) for Period E 2012 Data for long straws(up), short straws $z < 0$ (down left) and $z > 0$ (down right) in layer 1.	178
C.2	The relative change ($\Delta HT_{ratio} / (2 \times \text{ave } HT_{ratio})$) for Period E 2012 Data for layer 2 and 3 in Barrel.	178
C.3	$\Delta HT_{ratio} / (2 \times \text{average } HT_{ratio})$ for Period E 2012 Data in end-cap A. The left plot is for type-A wheels and the right plot is for type-B wheels.179	179

Acknowledgements

This thesis would not have been possible without the support of my friends, family, and colleagues. I would first like to thank my Ph.D. advisor, Professor Al Goshaw, for the guidance he has given me over the last five years at Duke, for always being patient and supportive. The members of my committee, comprised of Prof. Bass, Edwards, Kotwal and Walter, have given me invaluable feedbacks to my preliminary exam, my thesis and research work. I thank them for the time and efforts they spent to help directing my graduate studies towards a Ph.D.

I would also like to thank members of the Duke ATLAS group. Prof.Arce, Prof.Kruse and Prof.Kotwal have given me invaluable feedbacks to my research work during group meetings and private conversations. Our postdoctoral researchers, Andrea Bocci, Enrique Kajomovitz, Shu Li provided me with stimulating conversations which helped completing and improving the work documented in this thesis. Working within ATLAS would have been a far less productive and enjoyable experience without the people I have met along the way. Zhijun Liang has given me indispensable feedback and guidance as I have continued my studies. I would like to thank colleagues who I worked with on various projects in the ATLAS collaboration. Thanks to my Duke and CERN friends. Life without their companionship would be difficult to imagine.

Finally, I would like to devote this thesis to my parents. None of these would not have been achieved without their love, and being supportive, always, of my life

choices.

1

Introduction

The Standard Model (SM) of particle physics describes observed experimental phenomena up to the highest particle interaction energies with a few exceptions. Results from collider experiments have validated the SM for collisions with center of mass energies up to 8 TeV. However, the theory is not able to explain gravity or observations of dark matter. The core of the SM is the gauge structure determined by the underlying $SU(3)_C \times SU(2)_L \times U(1)_Y$ symmetry. The $SU(2)_L \times U(1)_Y$ electroweak (EWK) sector predicts self-couplings between the gauge bosons (W, Z and γ). Signatures with multiple electroweak gauge bosons at hadron colliders are essential in testing the $SU(2)_L \times U(1)_Y$ gauge structure. Precise SM predictions of these signatures can be calculated and compared to experimental findings. Physics beyond the SM (BSM) can change the production rate of multi-bosons processes and be used to probe the scale of new physics, providing constraints on anomalous couplings forbidden in the SM.

In the SM, a boson self-coupling interaction point can have associated three or four gauge bosons, referred to as triple or quartic couplings respectively. Triple gauge boson couplings have been measured extensively and found to be consistent with

the SM predictions by experiments at the Fermilab Tevatron and the CERN Large Hadron Collider (LHC). However, quartic couplings have never been probed previously because the contributions from these couplings are of very low rate. The dataset collected by the ATLAS detector at the LHC during 2012 provides unique opportunities to observe these processes for the first time. W bosons produced in association with two additional photons, $W\gamma\gamma$, and $W\gamma$ produced in vector boson scattering are the most promising first observations as they are produced at relatively high rates compared to other quartic coupling processes. This thesis presents a first measurement of $pp \rightarrow W\gamma\gamma + X$ production and $W\gamma$ produced by vector boson scattering using a dataset collected by the ATLAS detector at the LHC.

The contents of this thesis are presented as follows. A brief overview of the current theory framework and a physical motivation for measuring $W\gamma\gamma$ and vector boson scattering $W\gamma$ production are given in Chapter 2. In Chapter 3, the LHC experiment and ATLAS detector are described. Chapter 4 presents my work on the monitoring program for the Transition Radiation Tracker (TRT) of the ATLAS inner tracker and my contributions to constructing testing facilities for the R&D work to replace the inner tracker during future upgrades. The $pp \rightarrow W\gamma\gamma + X$ data analysis is described in Chapter 5, leaving the interpretation of the measured results to be discussed in Chapter 6. Preliminary results are presented in Chapter 7 of a measurement of the $pp \rightarrow W(e\nu)\gamma + 2$ jets, with $W\gamma$ produced by vector boson scattering ($WZ/\gamma \rightarrow W\gamma$) via quartic gauge boson couplings.

2

Theory and Motivation

The Standard Model (SM) has been a huge success in the field of particle physics during the past 50 years. In this chapter I will start with an introduction to the history and the mathematical formalism of the SM in Section 2.1, then move onto a detailed description of the electroweak sector and gauge boson couplings in Section 2.2. I will then discuss in Section 2.3 how one can test gauge boson couplings against the SM predictions at a collider experiment and also utilize any deviations from the SM as a model independent way of probing physics beyond the SM (BSM). Since this thesis presents a first measurement of $W\gamma\gamma$ production and $W\gamma$ vector boson scattering, the theory motivation for these measurements will be reviewed in Section 2.4. Finally the methods used to simulate experimental signatures at hadron colliders from theory predictions will be briefly described.

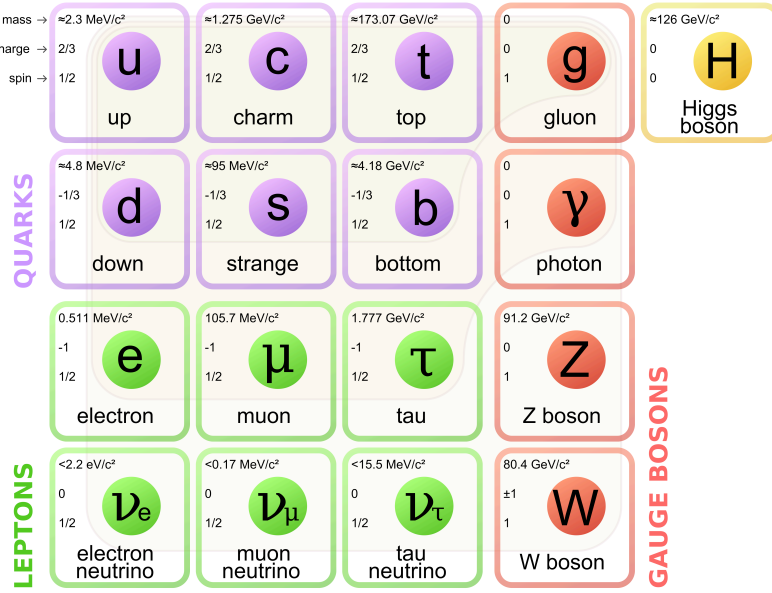


FIGURE 2.1: The Standard Model

2.1 Introduction to the Standard Model

The Standard Model is a particle physics theory that was developed throughout the latter half of the 20th century. It is a unified description of all the interactions of the known fundamental particles (except gravity). The structure of the SM is shown in Figure. 2.1 [3]. It contains three generations of quarks (purple), three generations of leptons (green), four gauge bosons (red) and the recently discovered Higgs boson. The fundamental particles in the figure are mathematically represented by states of quantized fields. The SM is a quantum field theory which obeys the $SU(3)_C \times SU(2)_L \times U(1)_Y$ gauge symmetry. Electromagnetism mediated by photons is a gauge theory under $U(1)$ transformations. In this case the gauge transformations are local complex phase transformations of the fields of charged particles, and gauge invariance necessitates the introduction of a massless vector (spin-1) particle (the photon), whose exchange mediates the electromagnetic interactions.

Guided by the gauge theory of electrodynamics, attempts were made to construct

a gauge theory of weak interactions based on $SU(2)$ symmetry. In the mid-1960s the hypothesized charged intermediate vector boson (W^\pm) was complemented with a neutral partner to achieve the required symmetry. To apply such a gauge theory to weak interactions, one arranges quarks, such as a u-quark and a d-quark and leptons, such as an electron and a neutrino, into weak isospin doublets. The transformation of the two states in a weak isospin doublet into each other under weak interactions is mediated by the W^\pm boson . The difficulty in the case of weak interactions was that they were known to be short range, mediated by very massive vector bosons, whereas a gauge-invariant theory require the gauge bosons to be massless. The Higgs boson, a scalar (spin-0) particle, and the Higgs mechanism were proposed to solve this problem [4]. The theory starts with a gauge-invariant Lagrangian, but the ground state of the theory is not invariant under the gauge transformations. The breaking of the invariance leads to a gauge-invariant and renormalizable theory with massive vector bosons. The recently discovered boson at the LHC announced on July, 4th, 2012, together with more recent experimental tests of its features, provide strong evidence for the Higgs boson and Higgs mechanism [5] [6].

The $SU(3)$ group of the Quantum Chromo Dynamics (QCD) sector introduces another degree of freedom referred to as color with the interactions mediated by eight bi-colored gauge bosons called gluons. The theory of the strong interaction acquired its modern form in 1970's, when experiments confirmed that the hadrons were composed of fractionally charged quarks [7]. One important feature of QCD is that due to color confinement, which means the color force mediated by the gluons increases when quarks are pulled apart, thus predicting no individual quark can be observed. The QCD sector is not of direct interests in terms of the physics topics covered in this thesis, albeit essential in understanding the phenomenology in hadron collider experiments which will be described in detail later in this chapter. Recent discoveries of the top quark (1995) [8] [9], tau neutrino (2000) [10] and the Higgs boson (2012)

have given further credence to the Standard Model, and complete the set of particles shown in Figure 2.1.

Despite its huge success in explaining and predicting most of the current experimental findings, the SM is an incomplete theory for various reasons. The first one being the failure to unify gravity, one of the four fundamental forces, into the theoretical framework. It also does not have candidates for fundamental particles that form dark matter as now observed in astrophysics experiment. From a theoretical point of view, the SM also suffers from issues such as the strong CP problem¹, and the fact that it requires many input parameters. Therefore one expect new physics to emerge above a certain energy scale where the SM breaks down, revealing a more fundamental understanding of elementary particles. Searches for new physics rely both on direct searches for particles predicted by specific extensions to the SM and precision measurements of processes predicted by the SM.

2.2 Electroweak sector and Gauge boson couplings

Although the electromagnetic forces and weak forces appear very different at low energy scales, they can be unified into electroweak forces described by $SU(2)_L \times U(1)_Y$ symmetry².

The dynamics of the SM, i.e., the motion defining interactions between excitations of the fields, can be described by a Lagrangian. In order to illustrate the gauge theory structure and the dynamics in the Electroweak (EWK) sector, the Lagrangian and the interactions is constructed as shown below from Chapter 15 in [11]:

¹ The strong CP problem asks why quantum chromodynamics (QCD) does not seem to break the CP-symmetry.

² L indicates that the $SU(2)$ operates on the left-handed projection of the weak isospin doublet. Y is the hyper charge of the $U(1)$ symmetry, defined as $2(Q - T_{3L})$, where Q is the electric charge (e.g +2/3 for u quark) and T_{3L} project the third component of the left-handed weak doublet (e.g +1/2 for u quark.)

$$\mathcal{L}_{EWK} = -\frac{1}{4}\mathbf{W}_{\mu\nu} \cdot \mathbf{W}^{\mu\nu} - \frac{1}{4}B_{\mu\nu}B^{\mu\nu} \quad \left\{ \begin{array}{l} \text{W}^\pm, Z, \gamma \text{ kinetic} \\ \text{energies and} \\ \text{self-interactions} \end{array} \right. \quad (1)$$

$$+\bar{L}\gamma^\mu \left(i\partial_\mu - g\frac{1}{2}\boldsymbol{\tau} \cdot \mathbf{W}_\mu - g'\frac{Y}{2}B_\mu \right) L \\ +\bar{R}\gamma^\mu \left(i\partial_\mu - g'\frac{Y}{2}B_\mu \right) R \quad \left\{ \begin{array}{l} \text{lepton and quark} \\ \text{kinetic energies} \\ \text{and their} \\ \text{interactions with} \\ \text{W}^\pm, Z, \gamma \end{array} \right. \quad (2)$$

$$+ \left| \left(i\partial_\mu - g\frac{1}{2}\boldsymbol{\tau} \cdot \mathbf{W}_\mu - g'\frac{Y}{2}B_\mu \right) \phi \right|^2 - V(\phi) \quad \left\{ \begin{array}{l} \text{W}^\pm, Z, \gamma, \text{ and Higgs} \\ \text{masses and} \\ \text{couplings} \end{array} \right. \quad (3)$$

$$-(G_1\bar{L}\phi R + G_2\bar{L}\phi_c R + \text{hermitian conjugate}). \quad \left\{ \begin{array}{l} \text{lepton and quark} \\ \text{masses and} \\ \text{coupling to Higgs} \end{array} \right. \quad (4)$$

Where each symbol is defined as following:

- g' and g are the coupling strength constants for the $U(1)_Y$, $SU(2)_L$ group respectively³. $\boldsymbol{\tau}$ are $1/2 \times \boldsymbol{\sigma}$, where $\boldsymbol{\sigma}$ are Pauli matrices.
- \mathbf{W}_μ is the three-component $SU(2)_L$ gauge field.
- $\mathbf{W}_{\mu\nu}$ is defined as $\partial_\mu \mathbf{W}_\nu - \partial_\nu \mathbf{W}_\mu - g \mathbf{W}_\mu \times \mathbf{W}_\nu$
- B_μ is the boson field corresponding to the $U(1)_Y$ symmetry, $\mathbf{B}_{\mu\nu} = \partial_\mu \mathbf{B}_\nu - \partial_\nu \mathbf{B}_\mu$.
- L , \bar{L} , R , \bar{R} represent the left and right handed fermion isospin doublets and their hermitian conjugates.
- Y is the weak hyper charge of the $U(1)_Y$ group.

³ In a quantum field theory with a dimensionless coupling constant g , if g is much less than 1 then the theory is said to be weakly coupled. In this case it is well described by an expansion in powers of g , called perturbation theory. If the coupling constant is of order one or larger, the theory is said to be strongly coupled. $g = \sqrt{4\pi\alpha}M_Z/M_W$, $g' = (G_F/(hc)^3 \times 4\sqrt{2}M_W C^2)^{1/2}$, where α is fine structure constant and G_F is Fermi constant.

- ϕ is the Higgs field, ϕ_c is another higgs doublet constructed from ϕ which transforms identically to ϕ and is used to generate fermion masses. G_1 and G_2 describe the couplings of fermions to the Higgs boson.
- $V(\phi)$ is the effective potential of the Higgs field. $V(\phi) = -\mu^2\phi^2 + 1/2\lambda\phi^4$.

The non-abelian nature of the $SU(2)$ group , i.e. the feature that the term $\mathbf{W}_\mu \mathbf{W}_\nu - \mathbf{W}_\nu \mathbf{W}_\mu$ does not vanish, gives terms involving the self-coupling of three or four gauge boson vectors from $-\frac{1}{4}\mathbf{W}_{\mu\nu} \cdot \mathbf{W}^{\mu\nu}$. To give an more physical understanding, the relations between the vector boson fields and physical particles are given as follows (omitting the four vector index for simplicity):

- The massive neutral boson : $Z = \cos\theta_W W_3 - \sin\theta_W B$.
- The massless neutral boson (photon): $A = \cos\theta_W W_3 + \sin\theta_W B$.
- The massive charged W bosons: $W^\pm = \frac{1}{\sqrt{2}}(W_1 \mp iW_2)$.

Where θ_W is defined as the weak mixing angle, $\sin^2\theta_W = 0.231$ [3] in the \bar{MS} scheme. Using these relations, one can expand $-\frac{1}{4}\mathbf{W}_{\mu\nu} \cdot \mathbf{W}^{\mu\nu}$ with the physical particles W^\pm, Z, γ . The graphical presentation of the expansion can be illustrated with the corresponding Feynman diagrams for trilinear couplings and quartic couplings that are allowed by the SM as shown in Figure 2.2. The allowed Triple Gauge Couplings (TGC) are WWA and WWZ and Quartic Gauge Couplings (QGC) are $WWZA$, $WWAA$, $WWZZ$, and $WWWW$.

These electroweak couplings can be tested at a hadron collider experiment with distinct experimental signatures. The triple gauge boson coupling interactions can be tested by looking at two categories of topologies: final states with two gauge bosons (di-boson production) or vector boson fusion channel with a single W or Z boson produced in association with two forward/backward jets in the final state. Quartic

coupling vertices can be tested with tri-boson production and a vector boson scattering processes with two gauge bosons produced associated with two forward/backward jets. Diagrams for selected final states to illustrate these topologies are shown in Figure 2.3. Here the massless neutral boson A is noted as γ , which is conventionally used in the experimental community. Each diagram corresponds to a matrix element, the square of which can be converted into the probability of observing such an event in nature as measured by a cross section. Thus one can make connections between the theoretical prediction based on these diagrams and experimental measurements of cross sections in experiments. As shown in Figure 2.3 (c), gauge boson couplings can generate a signature of a W boson with two photons. Figure 2.3 (d) shows a signature of a W boson plus a photon generated along with two quarks. These two production processes can be measured experimentally and are documented in this thesis. Such final states can also be used to set constraints on physics beyond the SM, which will be discussed in detail in the following section.

2.3 Anomalous gauge boson coupling

2.3.1 Overview

Any gauge boson couplings that are forbidden by the SM are referred to as anomalous gauge boson couplings. Experimentally the contributions from these anomalous couplings enhance the production of di-bosons, tri-bosons and modify the vector boson fusion/scattering in the high energy region probed by experiments. Examining the deviation from the SM predictions in the high energy regime serves as a model independent way of searching for new physics. Unlike searches motivated by specific extensions of the SM, model independent searches do not have any preferences for the specific kinematic regions, but aim at providing a general direction to where new physics occurs. For example, a search for a Z' boson predicted by an additional

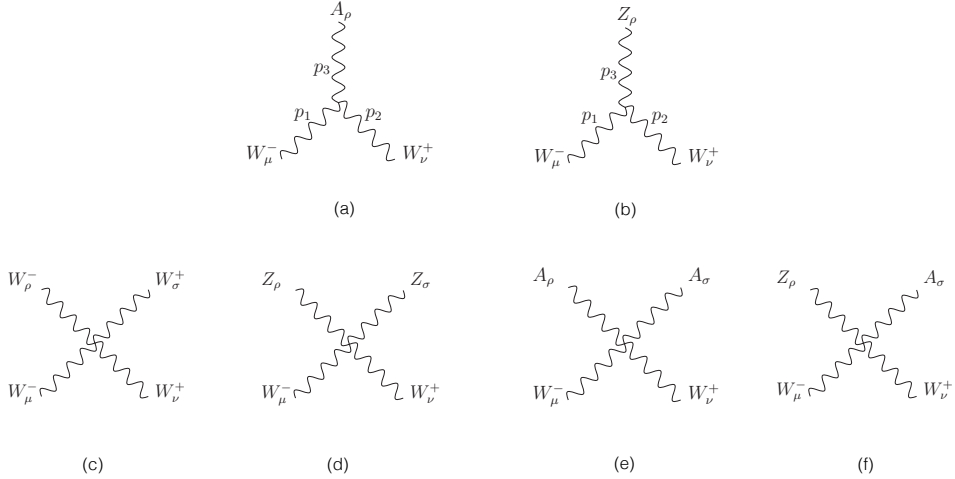


FIGURE 2.2: Gauge boson couplings in the SM EWK sector. (a) WWA , (b) WWZ , (c) WWW , (d) WWZ , (e) WWA , (f) WWZ

$U(1)$ symmetry group would be performed in regions which are optimized for Z' production but possibly blind to the production of other particles that are predicted by another BSM model. A model independent search has advantages of not biasing the phase space in the process, though may not be as sensitive as a search dedicated to a specific model.

2.3.2 Parametrization of anomalous couplings

Two conceptually different approaches were proposed in the late 1970s to parametrize anomalous gauge boson couplings. The first approach is referred as the anomalous electroweak gauge boson coupling framework and the other one is the effective field theory (EFT) framework.

- Parametrization using anomalous coupling framework

Taking trilinear gauge boson coupling for example, in the anomalous electroweak gauge boson coupling parametrization, the most general effective Lagrangian for

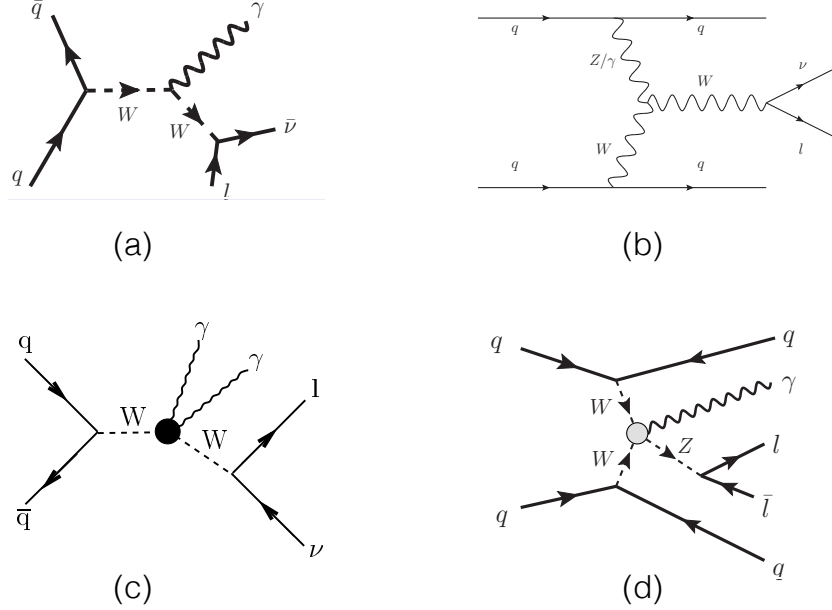


FIGURE 2.3: Illustrations of the topologies of the final states used to test gauge boson couplings : (a) $W\gamma$ final state to test the $WW\gamma$ vertex, (b) vector boson fusion W production to test $WW(Z\gamma)$ vertex. (c) $W\gamma\gamma$ final state to test $WW\gamma\gamma$ final state, (d) Vector boson scattering $Z\gamma$ final state to test $WWZ\gamma$ final state.

WWV , ($V=\gamma$ or Z), with lorentz invariance and CP conservation required can be written as [12]:

$$\mathcal{L}_{WWV}/g_{WWV} = ig_1^V (W_{\mu\nu}^\dagger W^{\mu\nu} V^\nu - W_\mu^\dagger V_\nu W^{\mu\nu}) + i\kappa_V W_\mu^\dagger W_\nu V^{\mu\nu} + i\frac{\lambda_V}{M_W^2} W_{\lambda\mu}^\dagger W_\lambda^\mu V_\nu V^{\nu\lambda} \quad (2.1)$$

where W^μ denotes the W^- field and $W_{\mu\nu} = \partial_\mu W_\nu - \partial_\nu W_\mu$. $V_{\mu\nu} = \partial_\mu V_\nu - \partial_\nu V_\mu$, where V_ν is the photon A_ν or Z_ν field. The coupling constants are chosen to be : $g_{WW\gamma} = -e$, $g_{WWZ} = -ecot(\theta_W)$. In the SM, $g_1^V = \kappa_V = 1$, and $\lambda_V = 0$. The last term illustrates an anomalous gauge boson coupling. Experimental constraints on

the allowed range of $\kappa_V - 1$ and λ_V are presented as anomalous gauge boson coupling limits. A detailed procedure of extracting this limit is described in the analysis results sections. It is important to point out that this parametrization of anomalous gauge boson coupling terms does not impose SM gauge invariance.

- Parametrization using Effective Field Theory EFT

The effective field theory approach considers the SM as the low energy limit of a more general BSM theory and new physics is introduced through operators that have dependence on a energy scale Λ . The resulting modified effective field theory extension of the standard model is [13]:

$$\mathcal{L} = \mathcal{L}_{SM} + \sum_i \frac{C_i}{\Lambda^2} \mathcal{O}_i + \sum_j \frac{C_j}{\Lambda^4} \mathcal{O}_j + \dots$$

where the \mathcal{O}_i are dimension-six operators and the \mathcal{O}_j are dimension-eight operators, and the dots indicate yet higher dimension operators. The coefficients c_i are dimensionless parameters indicating the strength that new physics couples to the SM particles. The SM is recovered in the limit of $\Lambda \rightarrow \infty$.

aTGCs can be introduced with dimension six operators in the following way: assuming C and P conservation, there are just three independent dimension-six operators that affect the electroweak triple vector boson self interactions [13]. They can be chosen to be:

$$\begin{aligned}\mathcal{O}_{WWW} &= Tr[W_{\mu\nu} \hat{W}^{\nu\rho} \hat{W}^{\mu\rho}] \\ \mathcal{O}_W &= (D_\mu \Phi)^\dagger \hat{W}^{\mu\nu} (D_\nu \Phi) \\ \mathcal{O}_B &= (D_\mu \Phi)^\dagger B^{\mu\nu} (D_\nu \Phi)\end{aligned}$$

where Φ is the Higgs doublet field. D_μ is the covariant derivative constructed with the electroweak gauge boson vector fields: $D_\mu = \partial_\mu + \frac{i}{2}g\boldsymbol{\tau}\mathbf{W}_\mu + \frac{i}{2}g'B_\mu$, $\hat{W}_{\mu\nu} = \boldsymbol{\tau}\mathbf{W}_{\mu\nu}$

with $\mathbf{W}^{\mu\nu}$ defined in Section 2.2. There are direct transformations to convert one set of anomalous coupling parameters to the EFT parametrization for the anomalous triple gauge boson coupling vertices. The coefficients of the dimension-six operators can be translated to the anomalous coupling parameters, for example:

$$\lambda_\gamma = \lambda_Z = \frac{3M_W^2 g^2}{2\Lambda^2} C_{WWW}.$$

where C_{WWW} is the coefficient in front of \mathcal{O}_{WWW} . A complete set of translations are documented in [13], while no such simple relations exist for the anomalous quartic coupling parameters.

The EFT approach respects $SU(2)_L \times U(1)_Y$ gauge symmetry [13], which is a fundamental difference from the anomalous coupling approach. The modifications of the SM due to heavier resonances (new physics) that are beyond the energy reach of current experiments will occur with additional loops induced by these particles while still respecting gauge invariance of the SM in the low energy regime. The limits obtained from the $W\gamma\gamma$ and VBS $W\gamma$ analysis presented in this thesis are quoted based on the more modern EFT approach.

- Anomalous Quartic Couplings

The triple gauge boson couplings were probed with experiments at the LEP accelerator, and tested with much higher precision with Tevatron and LHC data, setting very constraint limits on the aTGC parameters.

However, we just started directly studying the quartic couplings. It is important to notice that new physics due to anomalous triple couplings and quartic couplings could contribute to the deviations from the SM in very different ways. As illustrated in Figure 2.4, the exchange of heavy bosons can generate a tree level contribution to four gauge boson couplings while its effect in a triple gauge vertex would only appear at one loop level, and consequently be suppressed with respect to the quartic one [14]. It has also been argued that with the existence of a light Higgs boson, we

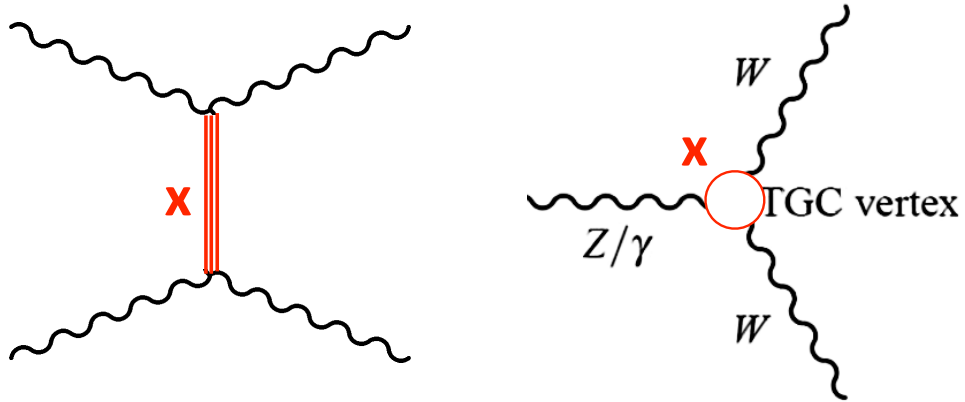


FIGURE 2.4: A heavy boson X contributes to TGC at one loop level as shown on the right and QGC at tree level on the left.

are lead to test the dimension eight effective operators through the final states of tri-boson production and vector boson scattering processes at the LHC [15].

2.3.3 Unitarization procedure

Unitarization is a natural constraint for a physics process because the number of observed events must be finite. The cross section for processes with non-zero anomalous coupling parameters diverges at high energies. A non-unitarized model can generate extra high energy events and produce more sensitive though non-physical limits on the anomalous coupling parameters. Thus a unitarization procedure is necessary. There are two commonly used procedures, the K matrix method and the form factor approach.

- K matrix method

The K matrix method is commonly used for the treatment of the pion scattering

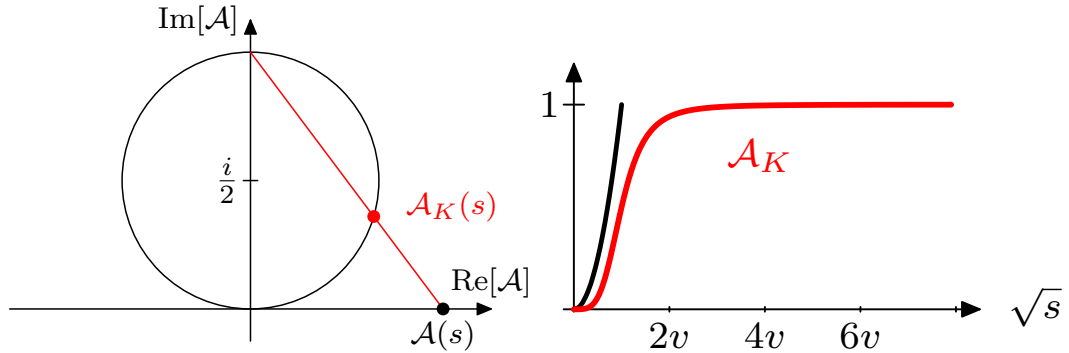


FIGURE 2.5: Argand circle is shown on the left. In the right plot, ν is the electroweak scale defined as $(\sqrt{2}G_F)^{-1/2} = 246$ GeV. It shows the saturation of WW vector boson scattering amplitude \mathcal{A}_K due to K-matrix unitarization.

which is a $2 \rightarrow 2$ process. The application to the gauge boson coupling case is discussed in detail in [16]. The main idea is summarized as following: for the processes of interest, the elastic scattering amplitude has to lie on the Argand circle $|\mathcal{A}(s) - \frac{i}{2}| = \frac{1}{2}$ shown in Figure 2.5 on the left.

For example, as shown in [16], for the process of WW vector boson scattering, by projecting an amplitude exceeding the unitarity constraint on the real axis back to the argand circle with the relation below:

$$\mathcal{A}_K(s) = \frac{\mathcal{A}(s)}{1-i\mathcal{A}(s)}$$

a finite scattering amplitude is achieved as shown in Figure 2.5 on the right.

- Form factor approach

The form factor approach introduces scale dependent functions $\mathcal{F}(s)$ to modify the coupling parameters $f : f(s) = \mathcal{F}(s) \times f$ [1].

$$\mathcal{F}(s) = \frac{1}{(1 + \frac{s}{\Lambda_{FF}^2})^n}$$

where Λ_{FF}^2 is a new energy scale and n is an integer. However n = 2 is favored in general since it provides the best attenuation for dim-8 operators and preserves unitarity at high energies including aQGC effects [17].

The K matrix method is a more natural choice for unitarization and does not introduce dependence on additional parameters. However the form factor approach is used in the $W\gamma\gamma$ ($2 \rightarrow 3$ process) presented in this thesis, due to the lack of the implementation of the K-matrix approach in the theoretical generators.

2.4 $W\gamma\gamma$ production and vector boson scattering $W\gamma$

- Experiment background review

Measurements of the production of W and Z bosons in association with high energy photons provide important tests of the SM. Total and differential cross-sections for the di-boson production processes W/Z plus one photon have been reported previously by the ATLAS and CMS collaborations, including the determination of limits on anomalous triple gauge boson couplings [18] [19].

$W\gamma\gamma$ production and $W\gamma$ vector boson scattering (VBS) have never been tested experimentally due to the low production rate. The cross section is a few fb ⁴ for $W\gamma\gamma$ and on the order of 10 fb for VBS $W\gamma$, with the W boson decaying leptonically, at a center of mass energy of 8 TeV in pp collisions [2]. The 20 fb^{-1} data collected by the ATLAS detector at the LHC (introduced in Chapter 3) at 8 TeV during 2012 provides opportunities to study these two processes and probe the existence of the SM quartic coupling. In addition, $W\gamma\gamma$ is a irreducible background for searches such as Higgs boson produced associated with a W boson with the Higgs boson decaying

⁴ A barn is defined as $10^{-28}m^2$ (100 fm², fm is one fermi) and is approximately the cross sectional area of a uranium nucleus. A femtobarn (fb) is 10^{-15} barn.

to two photons, and searches for supersymmetric particles in the final state of di-photon with large missing transverse energy [20].

- $W\gamma\gamma$ production and $W\gamma$ VBS in the SM.

The $W\gamma\gamma$ channel probes the $WW\gamma\gamma$ coupling. However the measured $W\gamma\gamma$ signal includes also contributions from other processes such as initial state radiation (ISR) and triple gauge boson coupling (TGC) as shown in Figure 2.6. Contributions and inferences between multiple diagrams make it a complex process to study. The

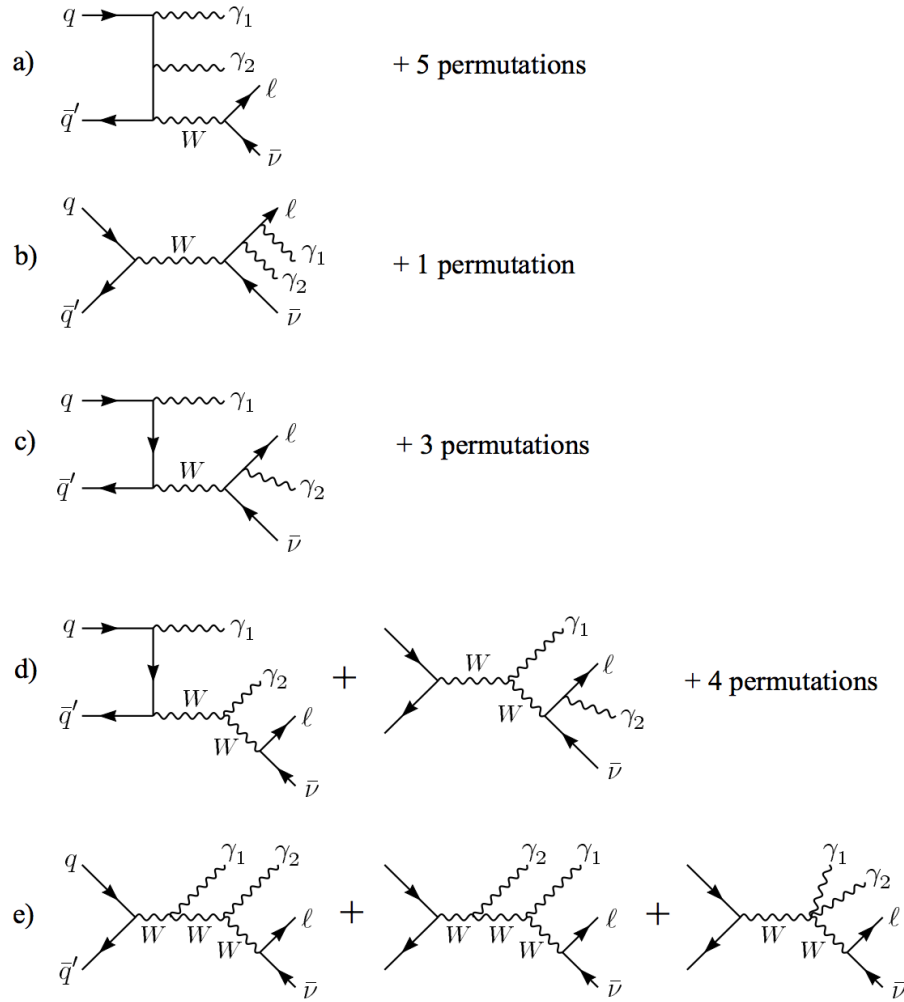


FIGURE 2.6: Main contributions to the $W\gamma\gamma$ final state. In general, the final state photons can come from: the final state radiation, the initial state radiation, the fragmentation of an initial state quark or gluon, a TGC vertex or a QGC vertex. [1]

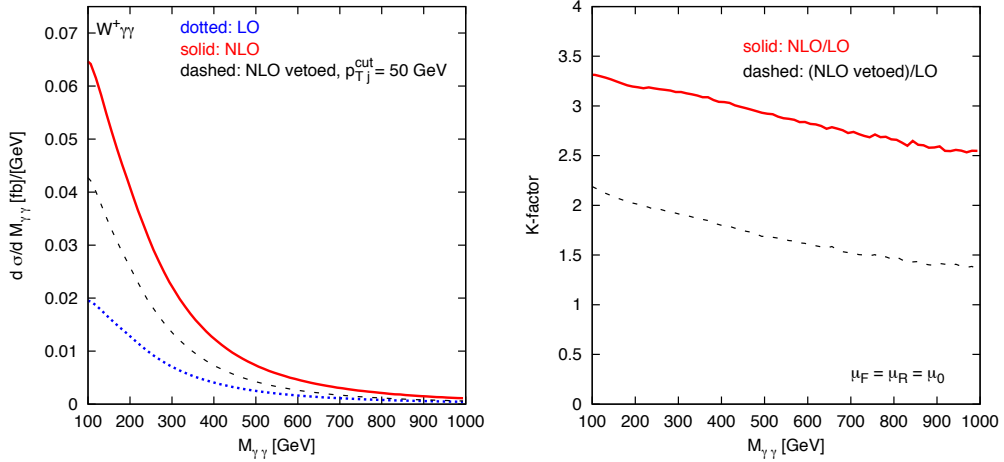


FIGURE 2.7: K factor as a function of the invariant mass of the di-photon system. Vetoed calculation veto events with an additional hadronic jet with $Pt > 50$ GeV [2]

$W\gamma\gamma$ final state has interesting behaviors that have been calculated theoretically, for example, the K factor, which is defined as σ_{NLO}/σ_{LO} ,⁵, has dependence on kinematic variables as shown in Figure 2.7. For an electroweak process, the k-factor of $W\gamma\gamma$ is also relatively large, the reason being that the destructive interference between ISR and TGC contributions at LO is suppressed at the NLO due to additional gluon radiation. A large k-factor indicates a bigger uncertainty on the theoretical calculation [2]. A better understanding of the production rate from experiments or theory calculations is important in understanding the background to BSM physics. A measurement of $W\gamma\gamma$ would provide better understanding of $W\gamma\gamma$ production and probes $WW\gamma\gamma$ coupling.

The quartic couplings that can be probed by the VBS $W\gamma$ are $WWZ\gamma$ and $WW\gamma\gamma$ as shown in Figure 2.8. The advantage of a VBS final state is that the scattered

⁵ σ_{LO} is the calculation of the cross section at leading-order, and σ_{NLO} is the calculation at next-to-leading order, the orders are for the strong coupling constant α_s

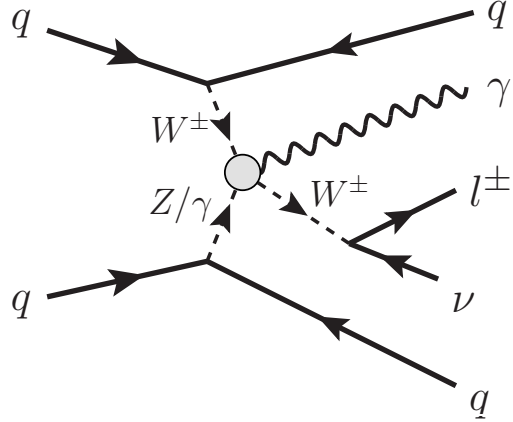


FIGURE 2.8: QGC $WWZ\gamma$ and $WW\gamma\gamma$ contributes to $W\gamma$ produced in vector boson scattering.

final-state quarks carry significant transverse momentum and are detected as very energetic forward/backward jets in the detector which can be used as a handle to suppress QCD backgrounds.

- aQGC contributions to $W\gamma\gamma$ production and $W\gamma$ VBS.

The aQGCs may be introduced with both dimension-6 or dimension-8 operators. For $WW\gamma\gamma$ the formalism used in the LEP studies were dimension-6 operators which generated purely aQGC vertices, with no anomalous triple gauge couplings (aTGCs).

These are written as:

$$\mathcal{L}_6^0 = -\frac{e^2 a_0^W}{8\Lambda^2} F_{\mu\nu} F^{\mu\nu} \vec{W}^\alpha \cdot \vec{W}_\alpha, \quad (2.2)$$

$$\mathcal{L}_6^c = -\frac{e^2 a_c^W}{16\Lambda^2} F_{\mu\alpha} F^{\mu\beta} \vec{W}^\alpha \cdot \vec{W}_\beta. \quad (2.3)$$

and limits have been derived for the parameters a_0^W and a_c^W [17]. However generally, operators of dimension 6 also modify three weak boson coupling and thus are typically better constrained by the measurement of di-boson final states. Therefore it has been proposed to study the aQGCs in a dimension-8 effective lagrangian formalism [17]. There are a total of 18 dimension-8 operators that do not generate aTGCs, of which 14 generate aQGCs of the form $WW\gamma\gamma$. The full list may be found in [17]. Three

operators in particular are considered here, referred to as $M2$, $M3$ and $T0$. The operators $M2$ and $M3$ have been chosen since they allow a comparison to previous measurements at LEP and TeVatron as described below [21]. In the unitary gauge the aQGCs Lagrangian terms (\mathcal{L}_{M2} corresponds to $M2$ for example) corresponding to these operators are:

$$\mathcal{L}_{M2} = -\frac{f_{M2}}{\Lambda^4} [c_w^2 F_{\mu\nu} F^{\mu\nu} + s_w^2 Z_{\mu\nu} Z^{\mu\nu} - 2s_w c_w F_{\mu\nu} Z^{\mu\nu}] [\frac{g^2 v^2}{4} W_\beta^+ W^{-\beta} + \frac{g^2 v^2}{8c_w^2} Z_\beta Z^\beta] \quad (2.4)$$

$$\mathcal{L}_{M3} = -\frac{f_{M3}}{\Lambda^4} [c_w^2 F_{\mu\nu} F^{\mu\beta} + s_w^2 Z_{\mu\nu} Z^{\mu\beta} - 2s_w c_w F_{\mu\beta} Z^{\mu\beta}] [\frac{g^2 v^2}{4} W_\beta^+ W^{-\mu} + \frac{g^2 v^2}{8c_w^2} Z_\beta Z^\mu] \quad (2.5)$$

$$\mathcal{L}_{T0} = -\frac{f_{T0}}{\Lambda^4} \text{Tr} [\hat{W}_{\mu\nu} \hat{W}^{\mu\nu}] \times \text{Tr} [\hat{W}_{\alpha\beta} \hat{W}^{\alpha\beta}] \quad (2.6)$$

where f_{M2} and f_{M3} are coupling parameters of dim-8 operators, $M2$ and $M3$. $W\gamma\gamma$ channel can supply information for the constraints on anomalous coupling parameters, f_{T0} , f_{M2} and f_{M3} [15]. f_{M2} and f_{M3} are relate to those of the dimension-6 formalism as

$$\frac{f_{M2}}{\Lambda^4} = -\frac{a_0^W}{\Lambda^2} \frac{s_w^2}{2v^2 c_w^2} \quad (2.7)$$

$$\frac{f_{M3}}{\Lambda^4} = -\frac{a_c^W}{\Lambda^2} \frac{s_w^2}{2v^2 c_w^2} \quad (2.8)$$

Thus the limits found on f_{M2} and f_{M3} may be directly compared to previous results from the LEP and other experiments.

- $W\gamma\gamma$ and VBS $W\gamma$ analyses in this thesis

A first-time measurement of the tri-boson production process of a W boson with two high energy photons is presented in Chapter 5 of this thesis. This analysis measures the production cross-section for $p + p \rightarrow \ell\nu\gamma\gamma + X$ ($\ell = e$ or μ) at $\sqrt{s} = 8$ TeV with a data set of integrated luminosity of 20.3 fb^{-1} collected by the ATLAS detector in 2012 and compares it to SM NLO predictions. Limits on anomalous gauge boson coupling parameters, f_{T0} , f_{M2} and f_{M3} , are also provided.

An analysis of vector boson scattering $W(e\nu)\gamma$ events selected from the dataset is presented in Chapter 7, with preliminary results of data analysis described.

2.5 Monte–Carlo Event Generation

In order to compare the theoretical predictions with experimental observations, the physics processes of interest as well as the detector response to the final state particles need to be simulated. In this section, I will discuss the event generation step, leaving discussions of detector response to the chapter of descriptions of the LHC and the ATLAS detector.

Event generators are used to model the complex physics processes occurring in collisions of high energy particle beams. A collision event in a hadron collider is shown in Figure 2.9. First, the interaction of a pair of partons originating from the incoming protons is simulated. This interaction of the two initial state partons is called the hard process. The parton components of the incoming protons are described by the parton density functions (PDFs) and the hard process is described by a matrix element corresponding to one or several Feynman diagrams. Calculations are normally categorized according to the power of α_s and α_{ewk} in the Feynman diagrams. Higher order QCD effects not accounted for in the matrix element are simulated later in the so called parton-shower process, in which gluon splitting and gluon radiation are taken into consideration. The fundamental difference between gluon radiation simulated in this process and one calculated in the matrix element at NLO is that spin correlations and interference effects are neglected. In the next step called hadronization, all colored objects are combined into colorless hadrons, which are allowed to decay. The colored remnants are allowed to interact, forming underlying events. Monte Carlo generators used to generate the signal processes and the cross sections of processes of interests are summarized here.

- Leading-Order event generators

AlpGen [22]

AlpGEN (A collection of codes for the generation of multi-parton processes in hadronic collisions) is a LO generator for SM processes with a emphasis on multijet final states. HERWIG+JIMMY [23] are then used for parton showers and hadronization for the

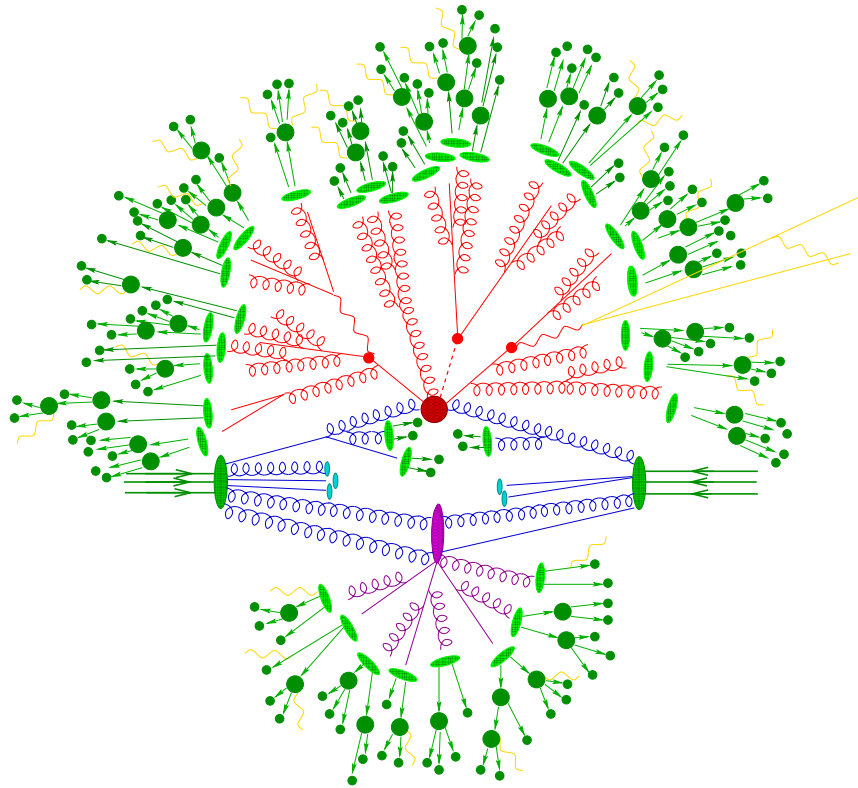


FIGURE 2.9: Sherpa collision simulation. Sketch of a proton proton collision at high energy. In the upper hemi-sphere of the figure partons from the initial protons (large green ellipses) radiate gluons and finally interact in the hard interaction (red blob). The products of the hard interaction produce a parton shower (in red) which then hadronizes (the green blobs are hadrons) which then decay into the final state particles, all shown as small green blobs. The lower hemisphere of the figure depicts the underlying event, starting from some gluons radiated off the protons, which also produce a parton shower (purple). The beam remnants (blue blob) are considered part of the underlying event. Photon radiation occurs at all stages in the event generation (indicated as yellow lines)

samples used in the studies in this thesis because these are not supported in AlpGen.

SHERPA [24]

SHERPA (Simulation for High Energy Reactions of PArticles) is a framework that uses AMEGIC++ (A Matrix Element Generator In C++) as the matrix element generator, by providing hard tree-level matrix elements and suitable integrators for $1 \rightarrow n$ particle decays and $2 \rightarrow n$ particle scatterings. Parton showering and hadronisation are also integrated as part of the SHERPA framework.

- Next-to-Leading-Order event generators

MCFM

MCFM (Monte Carlo for FeMtobarn processes) [25] is a parton-level event integrator which gives results for many processes. $W\gamma\gamma$ is calculated at NLO in MCFM.

VBFNLO

VBFNLO (Vector Boson Fusion at Next-to-Leading Order) [26] is a parton level Monte Carlo program for the simulation of vector boson fusion, double and triple vector boson production in hadronic collisions at NLO. Anomalous couplings in the EWK sector are also implemented for selected processes. Both the $W\gamma\gamma$ process and VBS $W\gamma$ process are included in VBFNLO. Cross sections with anomalous couplings are also calculated with VBFNLO and used for extracting aQGC limits.

2.6 Summary

The formalism of the SM was introduced in this Chapter, with an emphasis on the electroweak sector. The gauge boson couplings in the EWK sector and anomalous couplings were discussed in detail to motivate the measurement of the $pp \rightarrow W\gamma\gamma + X$ and vector boson scattering $W\gamma$ processes at the LHC. These measurements are also

used as probes of BSM physics. The phenomenology at a hadron collider was described at the end to bridge the theoretical calculations and experimental observables.

3

The LHC and the ATLAS experiment

This Chapter will describe the hadron collider (LHC) and particle detector (ATLAS) used to collide protons beams and collect data that are studied in this thesis. Upgrade plans for the ATLAS detector to operate in future high-luminosity LHC (HL-LHC) running conditions will also be discussed.

3.1 Introduction to the LHC

The LHC is a super-conducting accelerator installed in a 27 km circular tunnel that is buried 100 meters underground. It is located at the European Organization for Nuclear Research (CERN). The LHC spans the border between France and Switzerland, near the city of Geneva. A diagram of the LHC is shown in Figure 3.1. Beams of protons traveling in opposite directions in separate beam pipes around the accelerator ring are guided and accelerated to the final center of mass energy. The protons collide at interaction points along the ring at the locations of the four LHC experiments: ALICE, ATLAS, CMS, and LHCb. The two general purpose detectors, ATLAS and CMS, are designed to record as much information as possible about the proton–proton collisions with the aim of looking for any sign of new physics. ATLAS and CMS are the largest experiments at the LHC. LHCb is a single sided forward spectrometer specifically designed to investigate the physics of beauty quarks and hadrons. ALICE is used to investigate collisions of heavy ions. Its strength is the ability to reconstruct a large number of tracks in each collision. The aim is to study exotic states of matter at very high densities, such as a quark–gluon plasma. Two smaller experiments, TOTEM and LHCf, are placed at some distance from the interaction points to investigate particles produced at very small angles in the collisions. This region is experimentally inaccessible to the other detectors. TOTEM focuses on the measurement of the total elastic and diffractive cross sections of proton–proton interactions. LHCf uses the high energy protons to simulate the reaction chains induced by cosmic rays in the atmosphere.

The acceleration of the protons is accomplished in several steps. Protons, obtained from hydrogen atoms, are injected into a linear accelerator called Linac2 which accelerates the protons to a kinetic energy of 50 MeV. The protons are then injected into the Proton Synchrotron Booster (PS Booster), which accelerates them to 1.4 GeV.

After the PS Booster, the protons are sent to the Proton Synchrotron (PS) where they are accelerated to 25 GeV. They are then sent to the Super Proton Synchrotron (SPS) where they are accelerated to 450 GeV. In the final step the protons are accelerated to the full LHC energy. Under normal operating conditions, the colliding beams will circulate for many hours before the beams are dumped and the process repeated.

Another important characteristic of the LHC operation is the luminosity. The performance is typically described by the instantaneous luminosity and the integrated luminosity. The luminosity of a particle collider determines the rate of particle collisions it produces. Assuming a process $pp \rightarrow X$, the luminosity $\mathcal{L}(t)$ is the process-independent proportionality factor between the rate $R_{pp \rightarrow X}(t)$ and its production cross-section $\sigma_{pp \rightarrow X}$:

$$R_{pp \rightarrow X}(t) = L(t) \times \sigma_{pp \rightarrow X} \quad (3.1)$$

The instantaneous luminosity depends on the structure of the incoming beams and the collision rate as shown in Equation 3.2, where $n_{1(2)}$ are the number of particles per bunch in beam 1(2), $\sigma_{1(2)x(y)}$ are the transverse gaussian profiles for the two colliding beams. The beams are generally well-described by gaussian density profiles by the time the beam reaches high energy. f_r is the revolution frequency of the bunches. This equation shows that in order to achieve high luminosity, one needs tightly focused beams with highly populated proton bunches colliding at high frequency.

$$L = \frac{n_1 n_2 f_r}{2\pi \sqrt{\sigma_{1x}^2 + \sigma_{2x}^2} \sqrt{\sigma_{1y}^2 + \sigma_{2y}^2}} \quad (3.2)$$

The integral over time is called integrated luminosity, commonly denoted with $\mathcal{L} = \int L(t) dt$, and is measured in units of inverse barns. The integrated luminosity describes the total number of collisions recorded over a period of time. The number of expected

events produced in a dataset of luminosity \mathcal{L} can be calculated as:

$$N_{total}(pp \rightarrow X) = \mathcal{L} \times \sigma_{pp \rightarrow X} \quad (3.3)$$

The LHC is designed to produce collisions with a center of mass energy of 14 TeV. During the initial turn-on in 2008, one of the links between super-conducting magnets failed, leading to an explosion that damaged several other magnets. Problematic connections were found and repaired in several other magnet inter connections and additional quench protection was added. Until further repairs it was decided to run the LHC at a reduced energy. In 2010 and 2011, the LHC was operated at 3.5 TeV per beam, producing $\sqrt{s} = 7$ TeV collisions. In 2012, the energy was increased to 4 TeV per beam, producing $\sqrt{s} = 8$ TeV collisions. All collisions were recorded with a proton bunch spacing of 50 ns. Figure 3.2 shows the instantaneous luminosity of the 2010, 2011, and 2012 data sets. Figure 3.3 shows the integrated luminosity of the 2011, and 2012 data sets. The data sets collected in 2012 are the basis of the analysis work presented in this thesis. The large integrated luminosity of 20.3 fb^{-1} allows for the study of rare processes such as triboson production and vector boson scattering. The LHC has been shut down in 2013-2014 for repairs, after which it is expected to be operated at 6.5-7 TeV per beam with a bunch spacing of 25 ns.

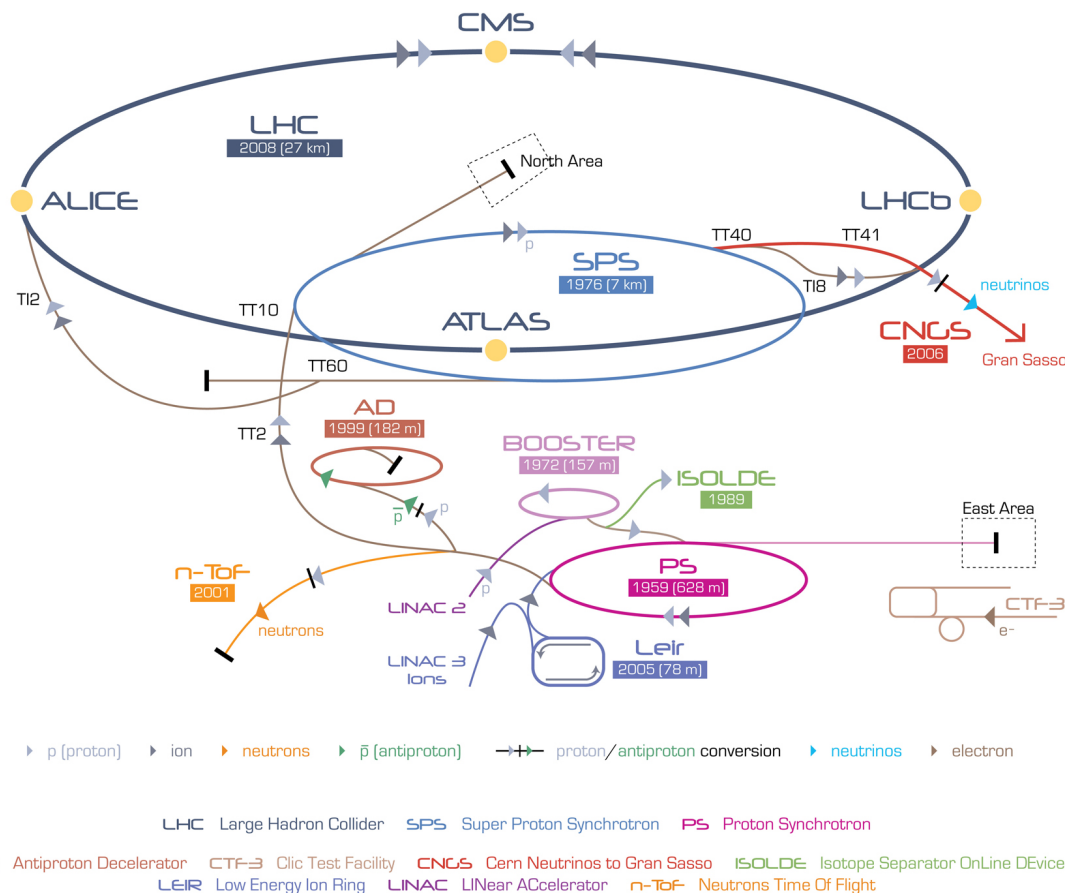


FIGURE 3.1: The LHC Accelerator Complex

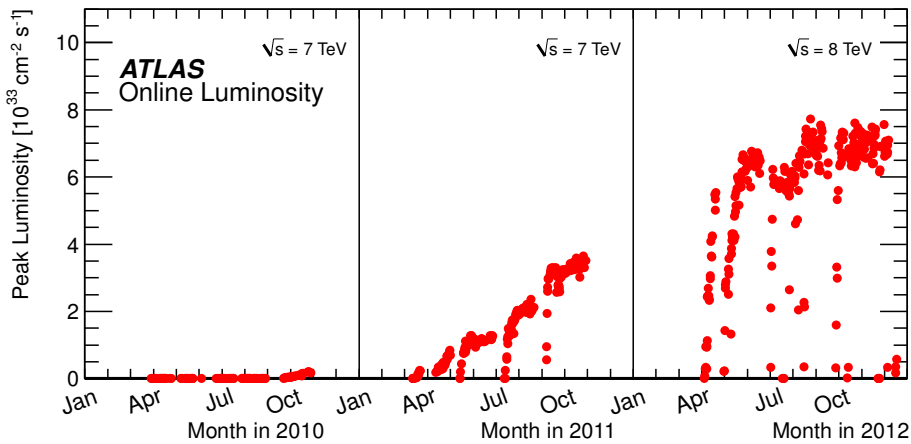


FIGURE 3.2: The peak instantaneous luminosity delivered to ATLAS per day versus time during the p-p runs of 2010, 2011 and 2012.

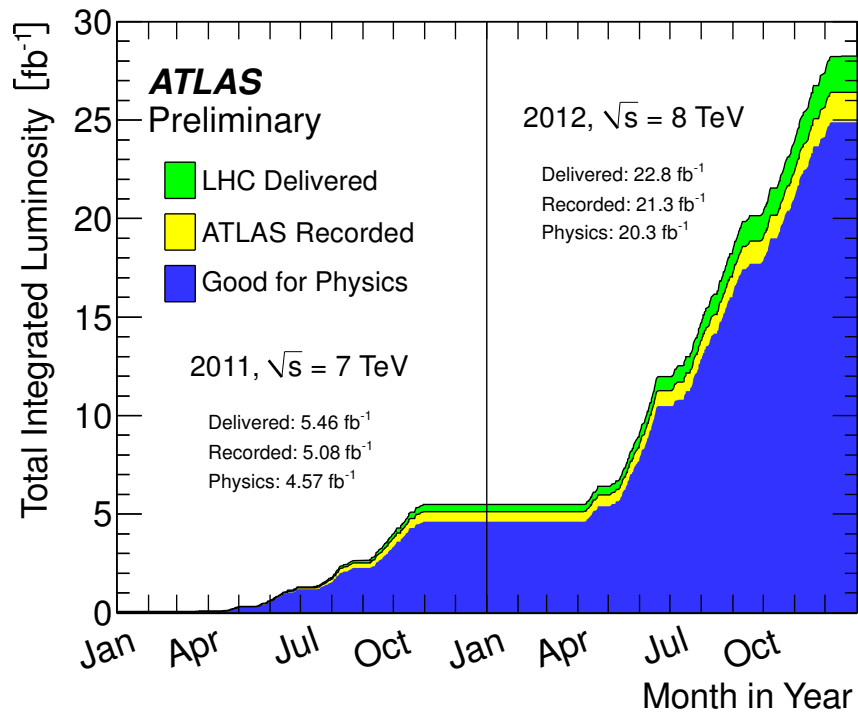


FIGURE 3.3: Integrated luminosity in 2011 and 2012

3.2 Introduction to the ATLAS detector

ATLAS is a general purpose detector, designed to cover a phase space of almost 4π steradians in solid angle around the interaction point (IP) [27]. An overview is shown in Figure 3.4, where the main sub-detector systems are shown: the inner detector, the electromagnetic calorimeters, the hadronic calorimeters, and the muon spectrometer. The nominal interaction point is defined as the origin of the coordinate system, while the beam direction defines the z -axis and the x - y plane is transverse to the beam direction. The positive x -axis is defined as pointing from the interaction point to the centre of the LHC ring and the positive y -axis is defined as pointing upwards. The azimuthal angle ϕ is measured around the beam axis in the x - y plane, and the polar angle θ is the angle from the beam axis. The pseudo-rapidity is defined as $\eta = -\ln \tan(\theta/2)$ (in the case of massive objects such as W/Z boson or jets, the rapidity $y = 1/2\ln[(E + p_z)/(E - p_z)]$ is used). The transverse momentum p_T , the transverse energy E_T , and the missing transverse energy E_t^{miss} are defined in the x - y plane. Each sub-detector will be discussed in the following subsections. The inner detector and calorimeter systems will be described at a detailed level. The muon system will be presented for completeness but the analyses documented in this thesis do not use muons.

3.2.1 Inner detector

The inner detector (ID) is designed to measure the trajectories of charged particles with great precision and to determine the position of the collision vertex and any secondary vertices. Secondary vertices occur when relatively long-lived particles like tau leptons and b-hadrons decay. The reliable reconstruction of secondary vertices is essential for the tagging of jets originating from a b-quark.

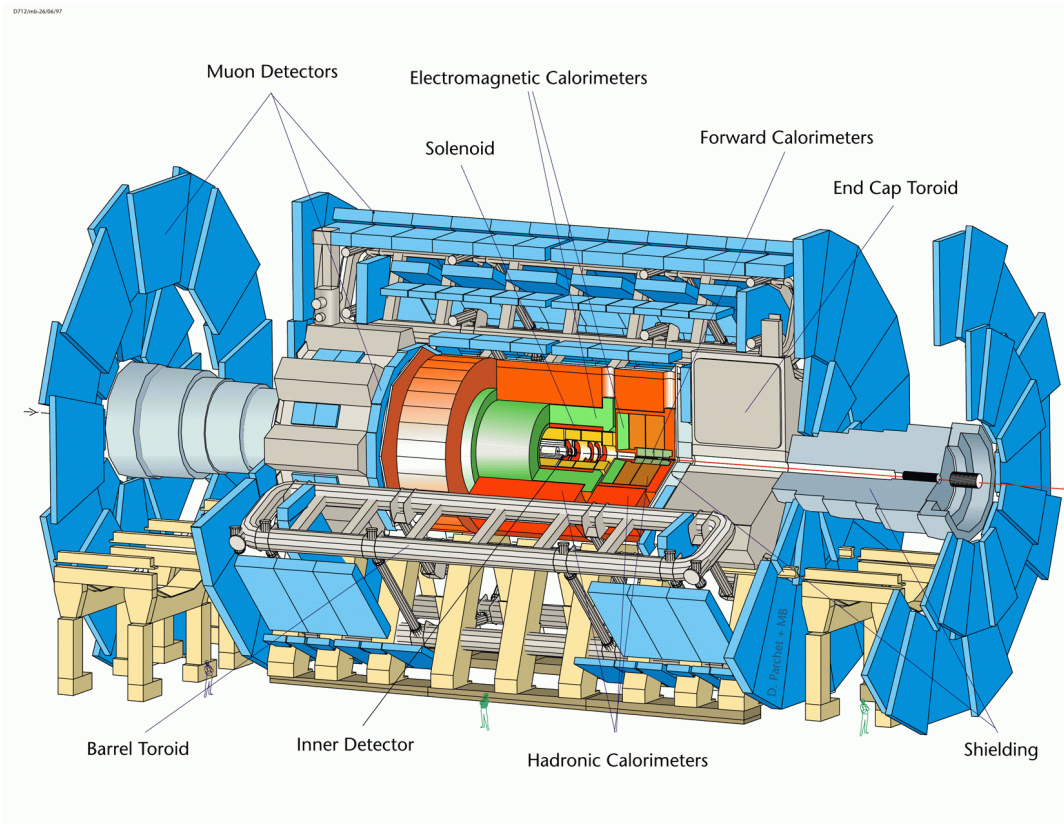


FIGURE 3.4: The ATLAS detector

The ID is composed of three sub-detectors immersed in a solenoidal magnetic field of 2 T parallel to the beam axis. A schematic drawing of the ID is presented in Figure 3.5. The sub-detectors are arranged as cylindrical layers in the central region (barrels), and disk or wheel like structures in the forward and backward regions (end-caps). Moving from the center to outside of the barrel detector, there are three layers of silicon pixel sensors (PIX), four layers of silicon strip detectors (SCT) and a straw tube tracker (TRT). The PIX and SCT are based on silicon semiconductor technology while the TRT is a gaseous detector. In total the ID extends 6.2 m in length, 2.1 m in diameter and covers a pseudo-rapidity range of $|\eta| < 2.5$. After alignment of the ID components, a transverse impact parameter resolution of $22 \mu\text{m}$ and a relative transverse momentum resolution $\sigma_{p_T}/p_T = 4.83 \times 10^{-4} \text{GeV}^{-1} \times p_T$

have been achieved for high momentum tracks.

- The Pixel detector.

The Pixel Detector (PIX) provides a very high granularity, high precision set of measurements as close to the interaction point as possible. The system provides three point measurements that determine precise impact parameters allowing the ID to identify short-lived particles. Pixels are grouped in 1744 modules with 46,000 pixels each, where every pixel is a readout channel. Each module is divided into 16 readout chips which are directly connected to the sensor substrate via bump-bonds to every pixel. The pixel dimensions are $50 \mu\text{m} \times 400 \mu\text{m}$ and provide a single hit resolution of $10 \mu\text{m}$ in the transverse plane and $115 \mu\text{m}$ in z for the barrel and in radius for the end-caps.

- The Silicon Strip Detector.

The Silicon Strip Detector (SCT) is designed to provide eight precision measurements per track in the intermediate radial range, contributing to the measurement of momentum, impact parameter and vertex position. The SCT is divided into four barrel layers and nine end-cap disks on each side with a total of 4088 modules. Each module consists of four sensors, two being daisy chained and glued back to back to provide a stereo angle of 40 mrad. Typical point measurement precision is presented in Table 3.1.

- The Transition Radiation Detector.

The Transition Radiation Tracker (TRT) is based on the use of straw tube detectors, which can operate at high rates due to their small diameter and the isolation of the sensor wires located in individual gas volumes. Electron identification capability is added by employing Xenon gas to detect transition radiation photons created in a radiator between the straws. The TRT consists of two main sections, the barrel detector and the end-caps. The barrel part covers the central pseudo-rapidity region ($|\eta| < 1.0$). The TRT end-caps cover the forward and backward pseudo-rapidity

Table 3.1: The main parameters of the inner detector. $r \times \Delta\phi$ is the transverse plane.

Detector	Section	η coverage	Resolution(μm)	Layers
Pixel	B-layer	± 2.5	$r \times \Delta\phi = 12, z = 110$	1
	Barrel	± 1.7	$r \times \Delta\phi = 12, z = 110$	2
	End-cap	1.7-2.5	$r \times \Delta\phi = 12, r = 110$	3
SCT	Barrel	± 1.4	$r \times \Delta\phi = 16, z = 580$	4
	End-cap	1-2.5	$r \times \Delta\phi = 16, r = 580$	9
TRT	Barrel	± 0.7	$r \times \Delta\phi = 170$	3
	End-cap	0.7-2.0	$r \times \Delta\phi = 170$	14

regions ($1.0 < |\eta| < 2.0$). The TRT is approximately 144 cm long and is composed of 298,144 straws of diameter 4 mm. Each straw is filled with a gas mixture, with the straw wall held at a high voltage of 1530 V and a gold-plated tungsten wire at the center with diameter 31 μm . The TRT will be described in detail in Chapter 4.

3.2.2 Calorimeters

The calorimeter system measures the energy of hadrons, electrons and photons. It provides coverage up to $|\eta| = 4.9$. An overview of the calorimeter system is shown in Figure 3.6. Hadrons, electrons and photons deposit their energy during showering in the calorimeter system without reaching the muon system.

The ATLAS calorimeters are a type known as sampling calorimeters. Only a fraction of the energy produced by the particle is measured by active detector sensors. The energy of the full shower can be inferred from the observed energy. The energies of electrons and photons are measured by the liquid-argon (LAr) electromagnetic (EM) barrel and end-cap calorimeters. The EM calorimeter is a lead-LAr detector with a specially designed geometry that provides uniform coverage and fast readout. The EM calorimeter is segmented into four radial sections with different granularities. Figure 3.7 shows a cut-away view of the different layers in the EM barrel calorimeter.

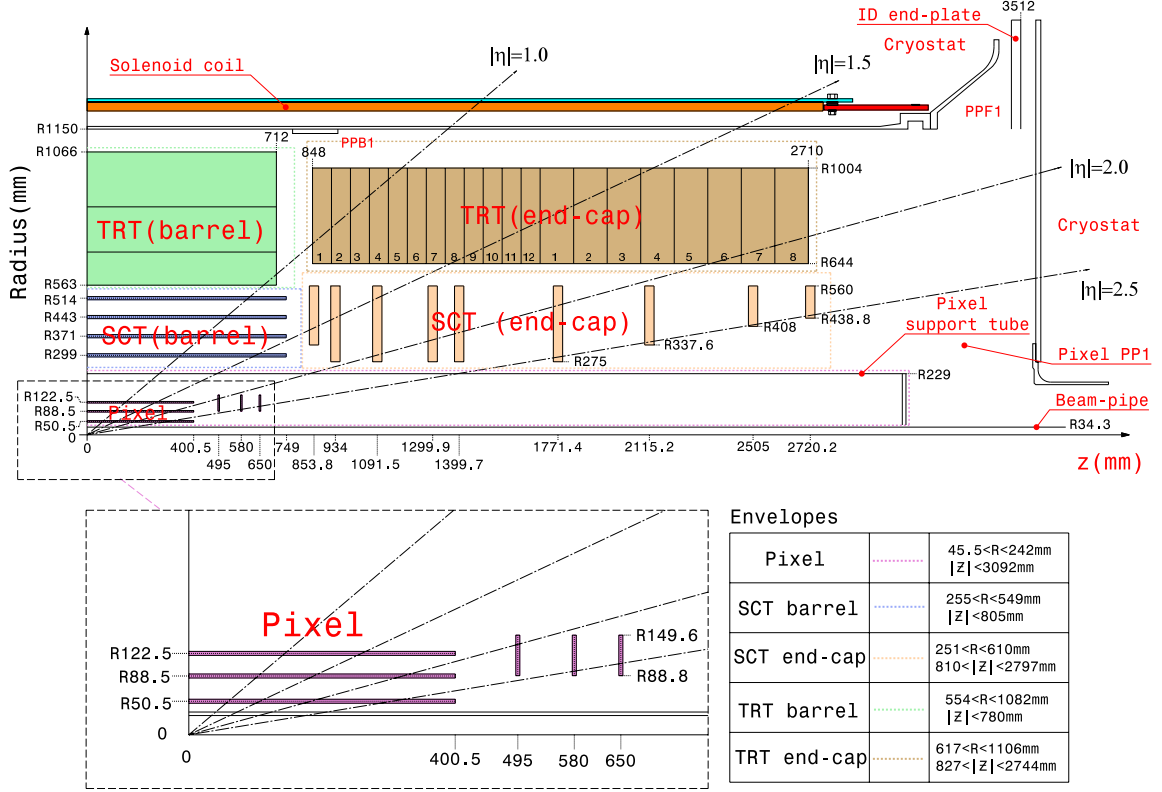


FIGURE 3.5: The inner detector of the ATLAS detector

The first sampling has a depth of 4.3 radiation lengths. The calorimeter readout is, as seen in Figure 3.7, in thin η strips, where each strip has the size $(\Delta\eta \times \Delta\varphi) = (0.0031 \times 0.098)$. This provides an excellent resolution in the η coordinate that helps distinguish between showers initiated by electrons or photons and showers initiated by neutral pions decaying into two photons. The majority of the energy is deposited in the second sampling layer. It has a depth of 16 radiation lengths. Electromagnetic showers (which will be referred to as clusters) with energy below 50 GeV are fully contained in this layer. For the position measurement of the cluster, the two coordinates are equally important, resulting in square cells of size $(\Delta\eta \times \Delta\varphi) = (0.0245 \times 0.0245)$. The third sampling layer is coarser and adds additional depth to the calorimeter to capture the highest energy electrons and photons. The clusters are wide at this point and the cell size can be doubled in the η direction without loss

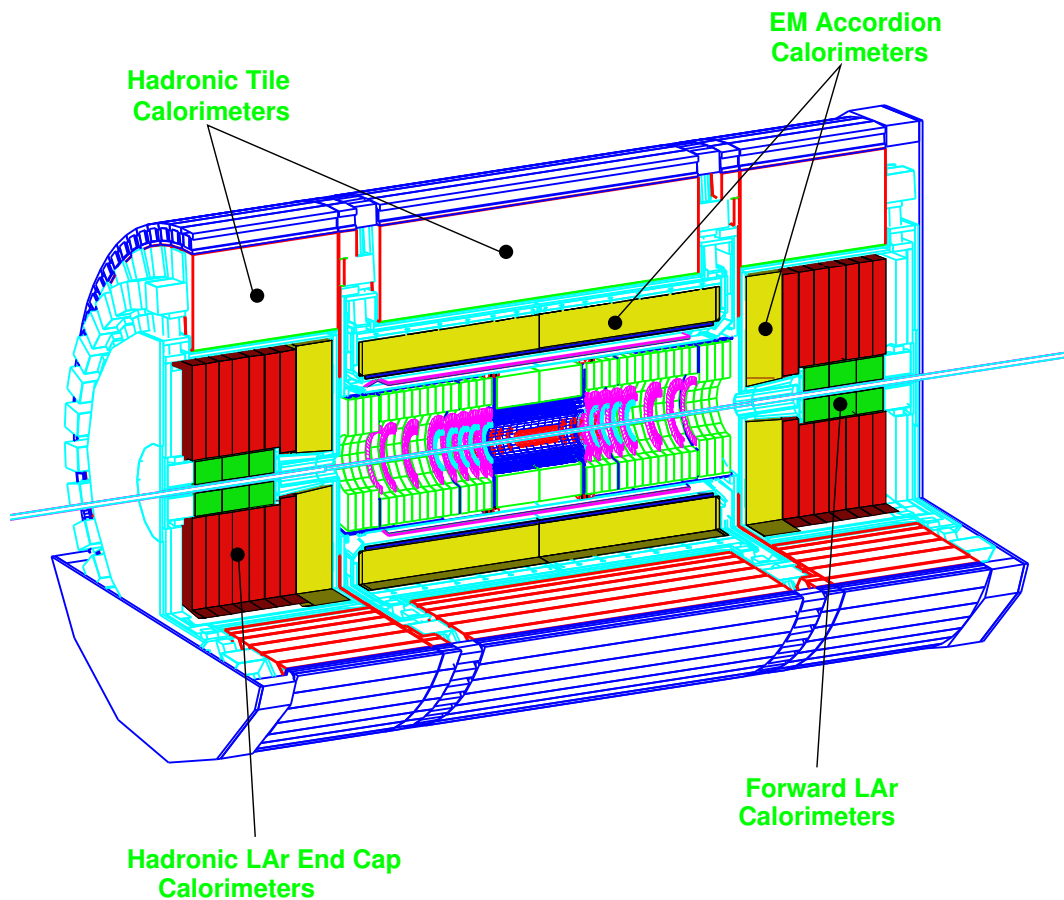


FIGURE 3.6: The Calorimeter system of the ATLAS detector

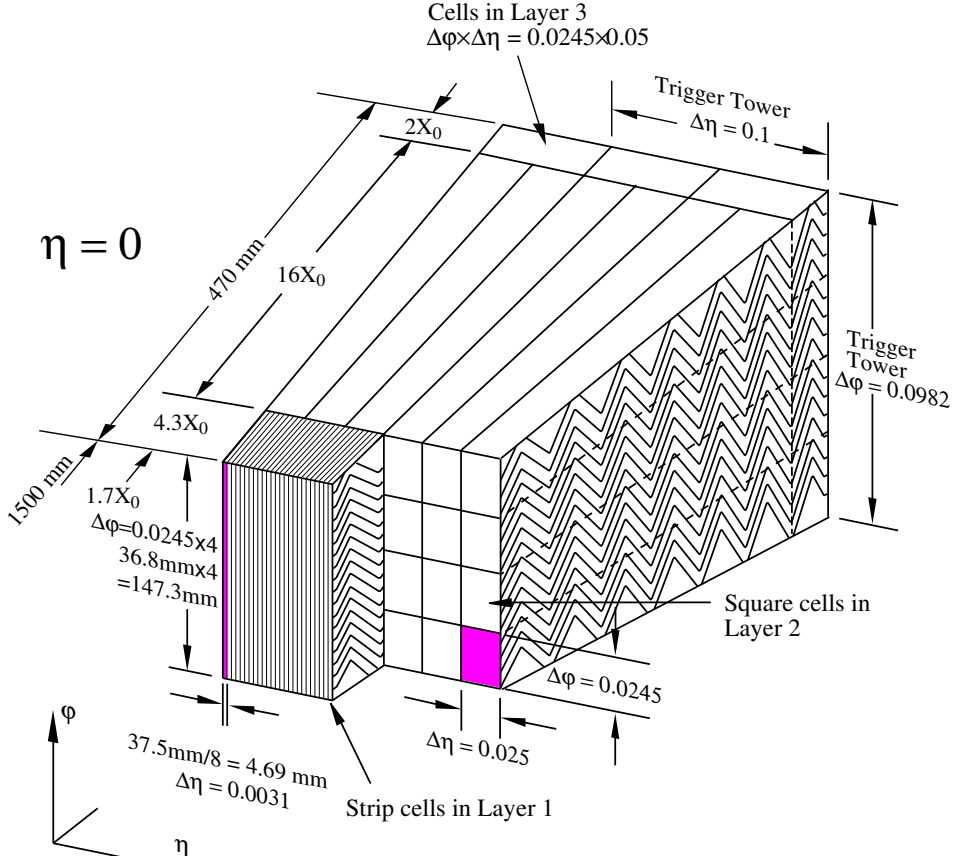


FIGURE 3.7: The Electromagnetic calorimeter in the ATLAS detector

of resolution. The EM calorimeters cover the pseudo-rapidity range $|\eta| < 3.2$.

The Tile calorimeters and the LAr Hadronic end-cap calorimeter are designed to measure the energy of hadrons. A range of $|\eta| < 1.7$ is covered by the Tile calorimeter that is separated into a barrel and two extended barrel cylinders. In the end-caps, $1.5 < |\eta| < 3.2$, a copper and liquid argon detector with parallel plates, similar to the electro-magnetic calorimeter, is employed due to its better radiation tolerance. The LAr forward calorimeters provide both electromagnetic and hadronic energy measurements and extend the pseudo-rapidity coverage to $|\eta| = 4.9$. The energy resolutions of the EM and the Hadronic calorimeters are:

$$\frac{\sigma}{E} = \frac{10\%}{\sqrt{E(GeV)}} \oplus 0.7\%(EM), \frac{\sigma}{E} = \frac{50\%}{\sqrt{E(GeV)}} \oplus 3\%(Hadronic) \quad (3.4)$$

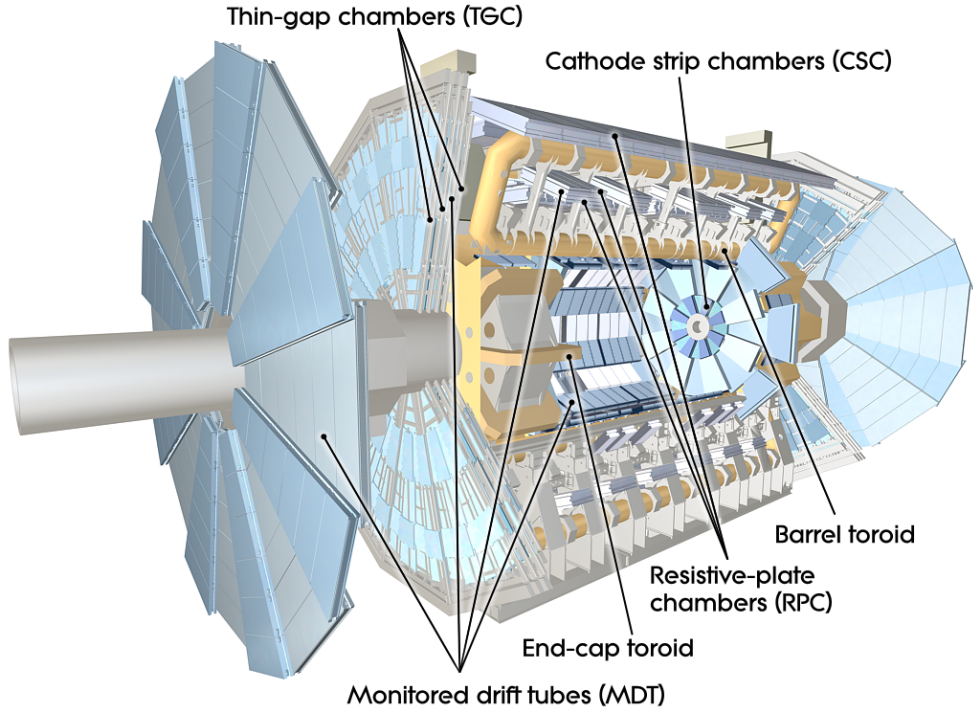


FIGURE 3.8: Muon systems in the ATLAS detector

3.2.3 Muon system

The calorimeter is surrounded by the muon spectrometer (MS) which measures the trajectory of muons as they traverse the detector. The layout of the MS is shown in Figure 3.8. Over the range of $|\eta| < 1.4$, magnetic bending is provided by a central barrel toroid. For $1.6 < |\eta| < 2.7$, muon tracks are bent by two smaller end-cap magnets inserted into both ends of the barrel toroid. In the region $1.4 < |\eta| < 1.6$, the bending is provided by a combination of the barrel and end-cap fields.

In the barrel region, the positions of the muons are measured in chambers arranged in three cylindrical layers around the beam axis. In the transition and end-cap regions, the chambers are arranged in three planes perpendicular to the beam. Over

most of the η range, the muon positions are measured by Monitored Drift Tubes. In the range $2 < |\eta| < 2.7$, Cathode Strip Chambers are used. The muon detector provides information used in the trigger system. The muon trigger chambers cover the pseudorapidity range of $|\eta| < 2.4$. Resistive Plate Chambers are used in the barrel and Thin Gap Chambers in the end-cap regions. The trigger chambers provide precise timing and well-defined p_T thresholds. The uncertainty on the transverse momentum measurement is less than 10% for a muon with $p_T < 1000$ GeV.

3.2.4 Triggering system

ATLAS has three levels of triggering to keep the data taking at an affordable rate and still capture interesting physics signatures. It is designed to record events at approximately 200 Hz from the LHC's 40 MHz proton-proton bunch crossing rate. The system has three levels as shown in Figure 3.9. The first level (L1) is a hardware-based system using a subset of the information recorded by the calorimeter and the muon detectors. It requires about 2 micro-seconds to reach its decision, including the propagation delays on cables between the detector and the underground counting room where the trigger logic is housed. All of the information from the detector must be stored in pipeline memories until the L1 decision is available. The level 2 trigger is a software-based system which refines the selection of candidate objects compared to L1, using full-granularity information from all detectors, including the inner tracker. In this way, the rate can be reduced to 1kHz. The Event filter (EF) level trigger is software-based. It uses offline physics and event reconstruction algorithms accessing the full event data and is expected to have a latency of a few seconds. A trigger requiring three EF level electromagnetic clusters is used in the $W\gamma\gamma$ analyses and a trigger requiring a single lepton in the vector boson scattering $W\gamma$ analysis. More details about these triggers are provided in Chapter 5 and 6.

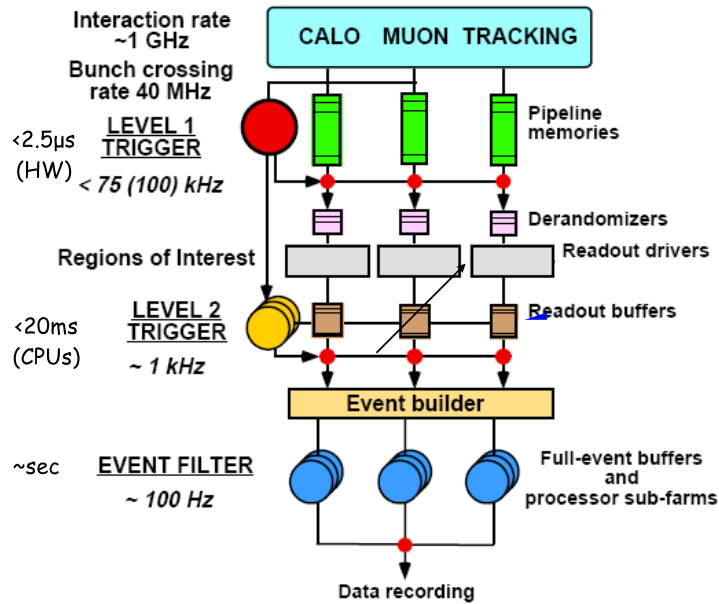


FIGURE 3.9: Trigger systems in the ATLAS detector

3.3 Particle detection with the ATLAS detector

Particle detection is a general term describing the process of using the recorded electronic signals to reconstruct and identify specific particles produced in the proton-proton collisions. Charged particles leave hits passing through the ID, and their momenta can be reconstructed from these hits with pattern recognition algorithms. Electrons, photons and jets deposit most of their energy in the calorimetry system where energy information is recorded in calorimeter cells. Various clustering algorithms are used to reconstruct electromagnetic showers left by electrons or photons and hadronic showers produced by hadrons. The reconstructed tracks and clusters are then matched to identify particles such as electrons, photons and jets. The recorded variables describing reconstructed clusters are used for further classification of the type of reconstructed particle.

Tracks recorded by the inner detector and muon system are used to identify muons.

Neutrinos escape the detector without being detected and only the information in the transverse plane can be reconstructed using four momentum conservation, since the kinematics along the z -axis is unknown for the incoming partons. tau leptons and b-quark jets leave a secondary decay vertex that is displaced from the primary interaction point. This information is used to reconstruct and identify tau leptons and b-quark jets.

3.3.1 Reconstruction and identification of electrons and photons

Since electrons and photons are of primary importance for the analyses discussed in this thesis, their detection will be described in more detail.

The reconstruction of electrons and photons starts with the information recorded by the calorimeter cells. A "sliding- window" algorithm is used to reconstruct clusters from the energy deposited in the cell. This algorithm is based on summing cells within a fixed-size rectangular window with the position of the window adjusted so that its contained energy is a local maximum. The clusters are matched to the reconstructed tracks, and the particles are then categorized as follows.

- Electrons are reconstructed if there is a suitable match with a track of $p_T > 0.5$ GeV.
- Photons are reconstructed if there is no reconstructed track matched to the cluster (unconverted photon candidates) or if there is a reconstructed conversion vertex matched to the cluster (converted photon $\rightarrow e^+e^-$ candidates)

Converted photon candidates are efficiently reconstructed only if the conversion radius is below 800 mm. High efficiency in this range can only be achieved if one considers, in addition to double-track conversions, the so-called single-track conversions, i.e. those for which only one track is reconstructed and no hits are found in the

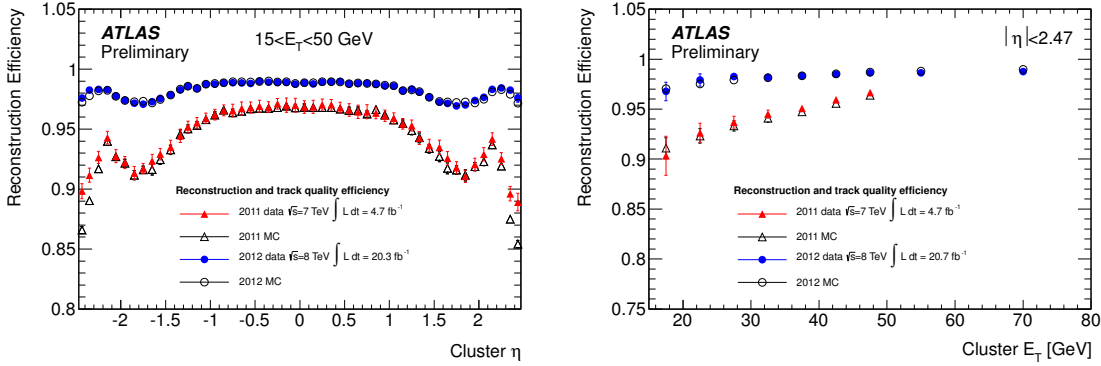


FIGURE 3.10: Electron reconstruction efficiency as a functions of η and E_T . Open circles are results from Monte Carlo simulations, Solid markers are estimated from data using a "Tag and Probe" method described in appendix.

first layer of the pixel detector. A large fraction of single-track conversion candidates correspond to a track reconstructed only in the TRT detector. The reconstruction efficiency for electrons as a function of the transverse energy E_T and pesudorapidity η can be found in Figure 3.10. The efficiency is greater than 95 % for electrons over the kinematic range used for analysis presented in this thesis.

The reconstructed particle candidates are then subjected to identification procedures designed to ensure that true objects are selected with a high and uniform efficiency, while suppressing background. For electrons, the backgrounds are from photon conversions and QCD jets, while for photons, misidentified signatures from QCD jets need to be suppressed.

The identification algorithm uses variables with discriminating power between desired particle candidates and background events. As mentioned before, an electron passing through the TRT will produce additional transition radiation photons, resulting in a stronger signal (referred as high threshold hits). The fraction of the high threshold hits associated with a track initiated by electron candidates has a well-separated distribution from the background events which are mostly hadrons as shown in Figure 3.11. Electrons can then be selected by requiring the fraction of

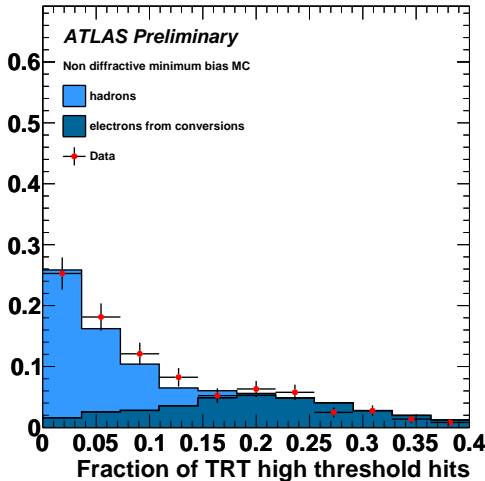


FIGURE 3.11: The fraction of high threshold TRT hits

high threshold hits on the track to be larger than 0.15. The baseline electron and photon identification algorithms in ATLAS rely on variables which deliver good separation between isolated electrons/photons and fake signatures from QCD jets. These variables include information from the calorimeter and, in the case of electrons, combined calorimeter/tracker information. Several selection criteria with different signal efficiencies are available for different purposes in analyses. Looser selections apply fewer requirements on the variables, resulting in higher efficiency for the desired particle candidates while suffering from larger background from fake signatures. Choices of variables used to define each operating point can be found in [28]. Starting from 2014, an electron identification algorithm based on a likelihood method has been developed by the ATLAS collaboration. These cuts are studied and chosen for the best selection efficiency of the signal process and rejection power of background events coming from other processes with false signatures. The identification efficiencies for electrons and photons are shown in Figures 3.12 and 3.13.

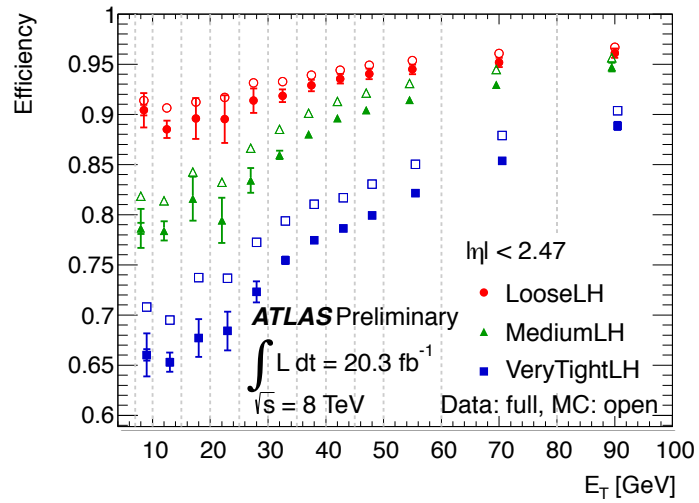


FIGURE 3.12: Electron identification efficiency as a functions of E_T for the LikeLyHood(LH) method is shown. Open circles are results from Monte Carlo simulated electrons, Solid markers are measurements from data using a "Tag and Probe" method described in appendix.

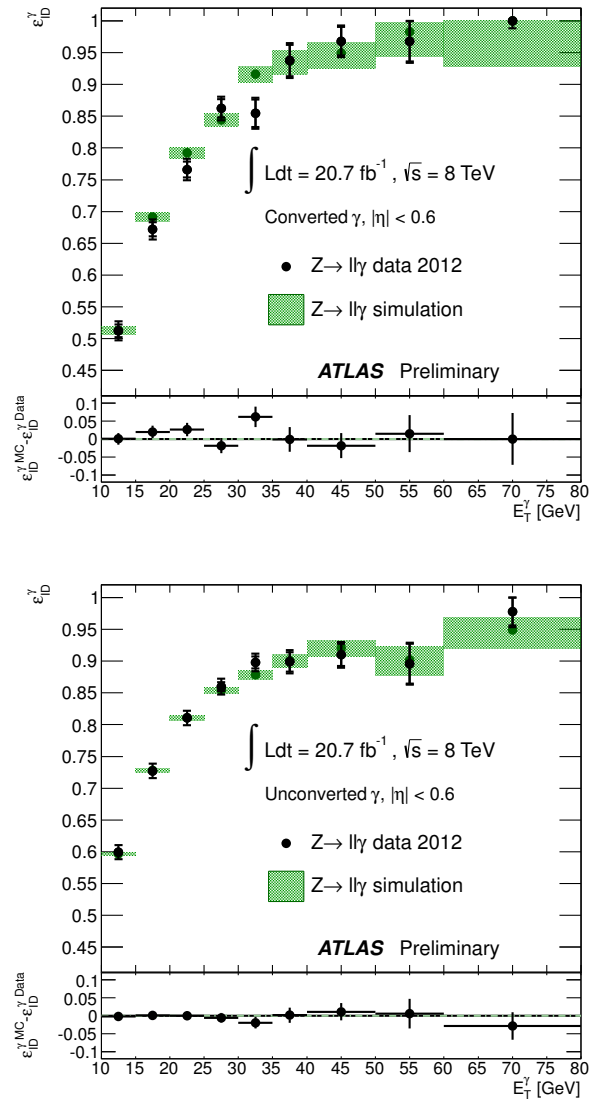


FIGURE 3.13: Photon identification efficiency as a functions of E_T for converted (top) and unconverted (bottom) photons. Results are measured from $Z \rightarrow ll\gamma$ events using a "Tag and Probe" method described in appendix.

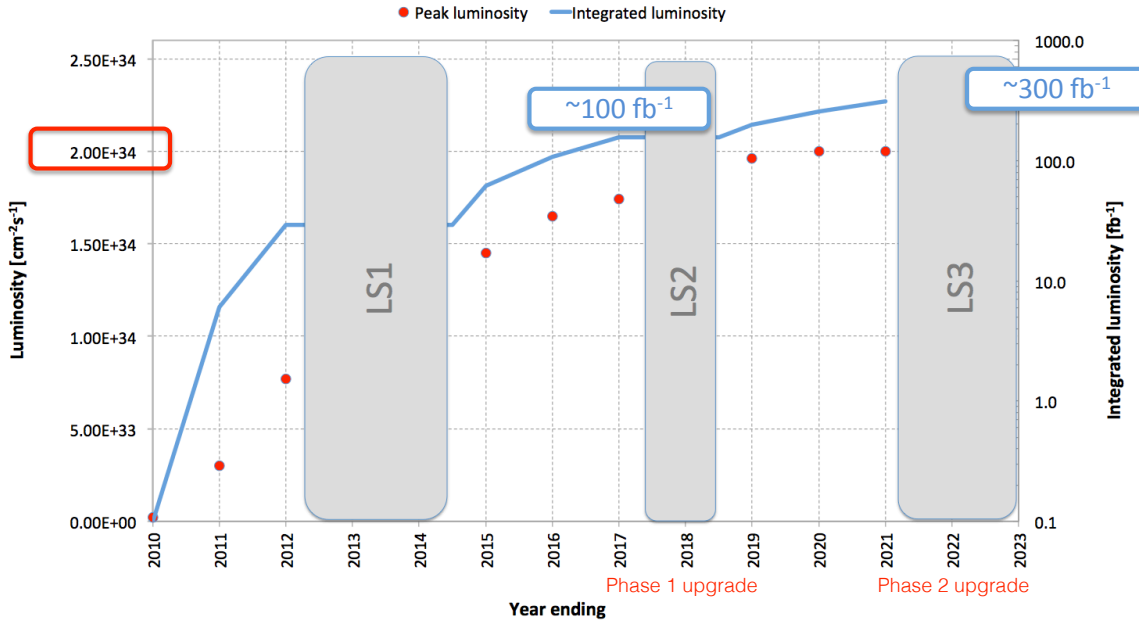


FIGURE 3.14: Plan for LHC evolution in the next 10 years. LS stands for 'Long Shutdown'

3.4 Status and future plans for the LHC and ATLAS detector

At the time of writing this thesis, the LHC is shut down for repairs. A new pixel layer is being installed in the ATLAS ID. Run 2 is expected to start in the Spring of 2015 with 6.5 TeV per beam and a proton bunch spacing of 25 ns. The goal is to collect 100 fb^{-1} data by the next scheduled shutdown in 2018. The expected peak luminosity and integrated luminosity the LHC is designed to achieve in the next 10 years are shown in Figure 3.14.

In order to meet the challenges and take advantage of the high peak luminosity conditions and large integrated luminosity of the future LHC, there are plans to upgrade the ATLAS detector to preserve and improve the current detection capabilities. The upgrades plans are referred to as Phase 1 and Phase 2 as shown in Figure 3.14. The phase 1 upgrade focuses on enhancements to the ATLAS trigger system to cope

with luminosities beyond the LHC nominal design value, while retaining the same physics performance [29]. For example, the new trigger system will allow ATLAS to maintain low p_T trigger thresholds for isolated leptons by increasing the granularity of the calorimeters involved in the Level-1 trigger.

After 2024, the High luminosity LHC(HL-LHC) will provide unprecedented pp luminosities, resulting in an additional integrated luminosity of about $2500\text{ }fb^{-1}$ over ten years. This will present a unique opportunity to extend searches for new physics, and to significantly improve the study of the Higgs boson. To preserve the current detection capabilities of the ATLAS detector in the HL-LHC running conditions, the current inner tracker needs to be fully replaced [30]. In addition, the readout of the calorimeter and muon systems will be upgraded. A new trigger architecture will be implemented exploiting the upgrades of the detector to maintain and improve the performance. Research and development (R&D) work on the inner tracker replacement to prepare for the Phase 2 upgrade will be reported in Chapter 4.

4

The ATLAS Inner Tracker Monitoring and Upgrade

The Transition Radiation Tracker (TRT) is constructed from gas-filled straw tubes that act as drift chambers for particle tracking and are also used to detect transition radiation for particle identification. The TRT improves curvature measurements of charged particle tracks and is useful for electron identification. As electrons are essential to analyses in this thesis, studies of the TRT performance are presented in detail in this Chapter. Aging of a straw tube detector under LHC operating conditions is a concern for its long-term operation. A study of the phenomena of wire aging and how it is monitored is presented. The Chapter ends with a description of plans to replace the current inner detector with an all-silicon tracker. As described in Chapter 3, this will be needed for operation of the ATLAS detector in the high luminosity conditions expected in HL-LHC running.

4.1 Description of the transition radiation tracker

The particle detection principle used by the TRT will be described in this section. The detector layout, gas flow and gas mixture will also be presented since these are essential in understanding the monitoring procedure of straw tube aging. The aging study and monitoring results will be summarized at the end of this Section.

4.1.1 *Detection of charged particles with the TRT*

The basic detector unit of the TRT is a 4 mm diameter straw tube which is filled with a gas mixture of 70% Xe + 27% CO₂ +3% O₂. As shown in Figure 4.1, when a charged particle passes through a straw, it ionizes the gas, freeing electrons which are subjected to strong acceleration by an electric field and subsequently collide with other atoms, producing more free electrons. This process repeats and creates an avalanche effect resulting in an amplified signal. The electrons drift towards the center wire and produce a signal. The space between the straws is filled with polypropylene fibers. When a charged particle passes through a boundary with a different index of refraction, in this case between the gas and the fibre, it produces tradition radiation (TR) as shown in Figure 4.1. The TR carries enough energy to liberate electrons from the gas, resulting in a stronger signal.

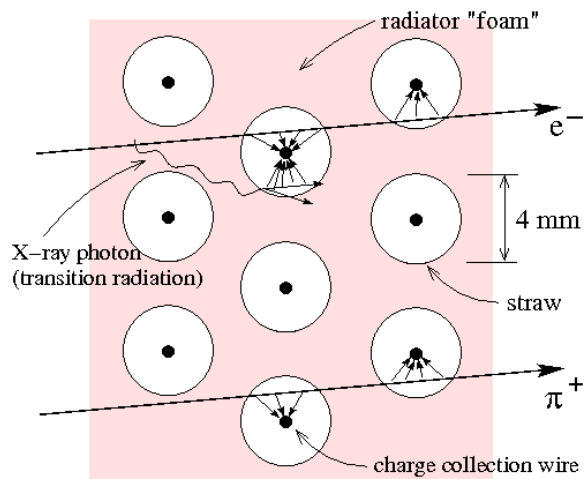


FIGURE 4.1: A cross section view of the straws to show signal detection in the TRT.

Collected signals are amplified and digitalized in the readout electronics located at the end of the straw. Thresholds are set on the signal shape to convert the analog signal to a digital signal, recorded as a hit used in the track reconstruction. There are two thresholds defined for a signal, a Low Threshold (LT) which is set at around 300 eV and a High Threshold (HT) at 6-7 KeV. This is the energy associated with the amount of ionization deposited in the straw as described by the Bethe-Bloch formula.¹

The probability of transition radiation increases with the relativistic gamma factor ($\gamma = E/mc^2$). For a given energy, this allows a discrimination between a lighter particle (which has a high gamma factor) and a heavier particle (which has a low gamma factor). The dependence of the transition radiation effect on the gamma factor is shown in Figure 4.2.

4.1.2 Detector layout and gas mixture

The TRT consists of two main sections, the barrel and the end-caps. The barrel covers the central pseudo-rapidity region $|\eta| < 1.0$ and the end-caps cover the forward and backward pseudo-rapidity regions $1.0 < |\eta| < 2.0$. The TRT is approximately 1440 cm long and is composed of 298,144 straws of diameter 4 mm. The gas flow will be described for the barrel and the end-caps since this is relevant for the aging studies discussed later.

There are 52,544 straws in the barrel detector. The straw layout was chosen such that a charged particle track with $p_T > 0.5$ GeV and pseudo-rapidity $|\eta| < 2.0$ would

¹ Bethe-Bloch formula describing energy loss per unit length :

$$-\frac{dE}{dx} = \frac{4\pi}{m_e c^2} \frac{nz^2}{\beta^2} \left(\frac{e^2}{4\pi\epsilon_0} \right)^2 \left[\ln\left(\frac{2m_e c^2 \beta^2}{I(1-\beta^2)}\right) - \beta^2 \right]. \quad (4.1)$$

Where v is the speed, z is the charge, E is the energy of the charged particle, x is the coordinate of the direction that the charged particle is traveling in, n is the electron number density, I is the mean excitation potential, c is the speed of light, ϵ_0 is the vacuum permittivity, $\beta = v/c$, e is the electron charge, and m_e is the mass of the electron.

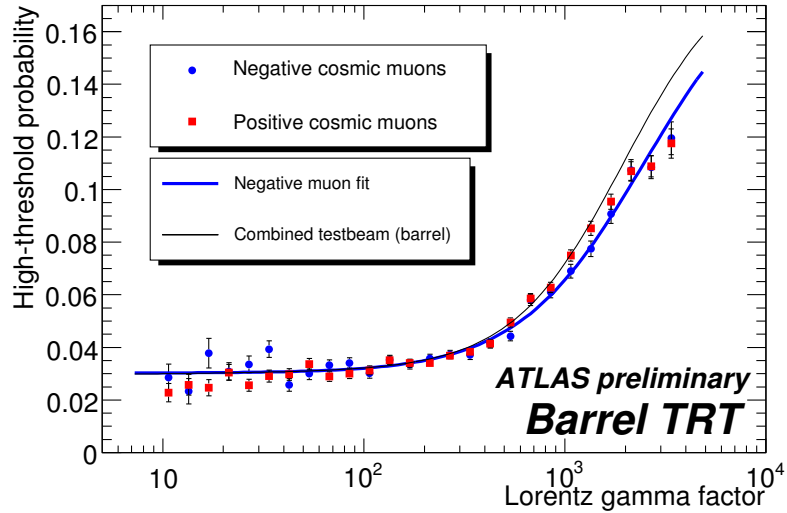


FIGURE 4.2: Turn-on of Transition Radiation from Muons measured in the ATLAS Barrel TRT (Oct'2008). Most of the particles produced at the LHC lie in an energy range of 500 MeV to 100 GeV. With the equation of $E = m\gamma$, pions have gamma factors in the range of $[10, 10^3]$ while a 500 MeV electron has a gamma factor of 10^3 .

cross approximately 35 straws. The gas enters the straws from two ends: Input A is at +720.5 mm and Input C is at -720.5 mm. The gas flows parallel to the beam line, in opposite directions for the two inputs. There are three radial layers in the barrel, each layer is segmented in phi sectors which are the basic unit for gas flow. In each layer, 16 of the phi modules have gas from Input A and the other 16 modules have gas from Input C. The azimuthal distributions of the phi modules for Input A are shown in Figure 4.3.

The end-caps are situated at opposite sides of the beam crossing point ($z=0$), composed of End-cap A(+z) and End-cap C(-z). Each end-cap has a length of 2.2 m and a diameter of 1.9 m, and is composed of 122,880 straws. The straws in the end-caps are oriented radially and are perpendicular to the beam axis, forming a plane of straws. There are a total of 160 straw layers in each end-cap. Eight (Four) straw layers form a bigger unit referred to as an eight (four) plane wheel. There

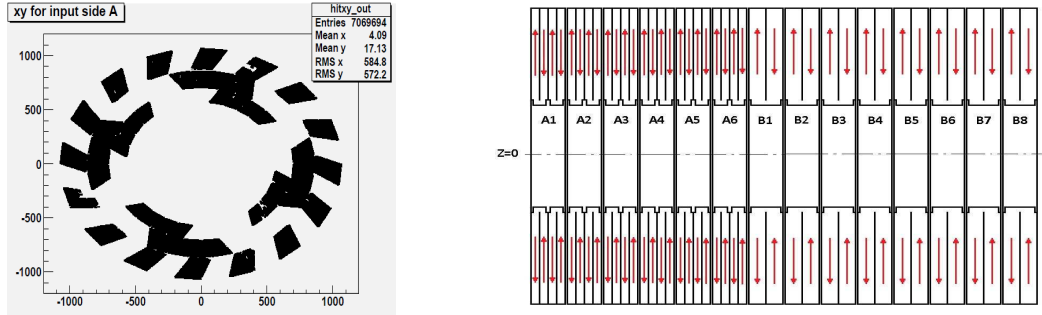


FIGURE 4.3: Left: X-Y Slice of the TRT Barrel. Phi modules with gas flow coming in from Side A is shown as black blocks. Right: A diagram of the gas flow in End-cap A.

are two types of wheels, type-A and type-B, with different separation between straw layers in the wheel. Adjacent straw layers in type-A (B) wheels are separated by 4 (11) mm in the z -direction. Each eight plane wheel is made up of two back-to-back four plane wheels. The gas flow in End-cap A is shown in Figure 4.3. As can be seen from Figure 4.3, the gas enters the outermost (in z -axis) four plane wheels from the outer radius of the end-cap and travels towards the inner radius, then enters the next four plane wheel from the inner radius and exits from the outer radius.

TR absorption ability, electron drift velocity, stability and aging factors were carefully considered when the gas mixture of 70% Xe, 27% CO₂ and 3% O₂ was chosen. Xenon makes up the base of the gas which is chosen for its excellent ability to absorb x-ray TR. The CO₂ gas helps to quench and stabilizes the gas by absorbing ultraviolet photons which prevents a secondary avalanche that could cause damage. O₂ increases the protection against hydrocarbon deposits on the wires. One of the issues with the introduction of O₂ gas is the production of ozone when the straws are irradiated. Gas studies verified that for concentrations of O₂ under 3.5%, ozone would not significantly affect TRT performance [31].

4.2 Monitoring the performance of the TRT

4.2.1 Aging and other performance issues

The TRT is subject to large doses of radiation during operation with the high luminosity achieved at the LHC. Understanding the effects of aging is important for reliable data-taking in the long term. Silicon and hydrocarbon composites due to contamination of materials in the gas delivery system can be carried in by gas flow. They can polymerize and create deposits on the wire, causing a drop in gas gain which leads to a gradual signal loss [32]. Impurities that form larger molecular chains can insulate the wire and eventually change the geometry and electric field conditions in an irreversible manner [33].

Irradiation tests were performed by heavily irradiating TRT straws for up to 30 hours [33, 34]. The mixture of 70% Xe + 27% CO₂ + 3% O₂ was validated for usage under high luminosity and aging conditions in these studies. However, this does not guarantee eliminating damages during machine running time. Thus a cleaning procedure was proposed. This is done by introducing a mixture containing CF₄ for “cleaning” runs to remove the silicon deposits on the wire [31]. It is important to monitor the wire aging during TRT operation to assist in decisions about whether to run clean procedures or apply offline calibrations to correct for modest aging effects.

4.2.2 Methods for monitoring the TRT

Aging reduces the signal size, affecting both the Low threshold (LT) and High threshold (HT) efficiencies. The fraction of HT (High Threshold) hits out of total number of hits, referred to as HT_{ratio} , is expected to be sensitive to this change since a much larger pulse is required to trigger the high threshold. In order to monitor any deterioration in the straws, we measure the HT_{ratio} in the direction of gas flow, as aging has been shown to be dependent on gas flow direction. We also study other factors

that can affect the aging monitoring parameters, such as ozone production from the oxygen in the gas mixture and constantly changing LHC running conditions.

Parameters of interests

HT_{ratio} as a function of the z coordinate, grouped by gas flow direction, is plotted in Figure 4.4 for a typical layer with Period E 2012 data ². The hit position in z is extrapolated from tracks reconstructed using combined information from the Pixel Detector and the SCT. As shown in Figure 4.4, there is evidence for a small decrease in HT_{ratio} vs gas flow direction, being higher at the gas entry side. The HT_{ratio} also rises at high values of $|z|$ as shown in Figure 4.4. This effect is geometrical due to increases in track path length through the straw at large z .

Since aging has dependences on gas flow directions, the degradation effect as a function of z is the opposite for Input A and Input C segments. To quantify this effect and remove the geometrical effect, the difference of $HT_{ratio}(\text{Input A}) - HT_{ratio}(\text{Input C})$ as a function of hit z -coordinate is taken and normalized by twice the average of HT_{ratio} value. Data points are then fitted to a slope of ΔHT_{ratio} vs z . Results for the second layer in the barrel are shown in Figure 4.5.

The fitted positive slope indicates a decrease in HT_{ratio} along the direction of gas flow for the long straws. The drop in HT_{ratio} along the length of the straw is nearly 6%. An increasing slope value over a long period of time (the order of years) would indicate an accumulation of silicon deposits on the wire. Monitoring plots in other layers of the barrel are similar to what is shown for Layer 2. More details can be found in the appendix.

Similar studies are performed as a function of the r coordinate in the end-caps because the straws are perpendicular to the beam and extend radially outward. Straw

² Period E refers to one run period of data taken from 2012 . It contains sufficient statistics for documented studies. Monitoring plots shown until Section 4.2.3 are produced with this dataset.

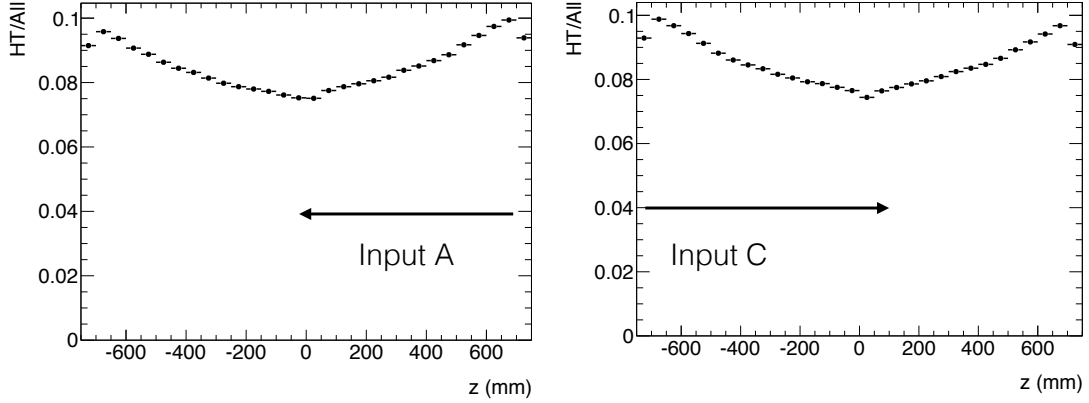


FIGURE 4.4: HT_{ratio} as a function of hit z position in the TRT barrel detector for Period E 2012 data. On the left is input A and on the right is input C. Layer 2 is shown as an example here.

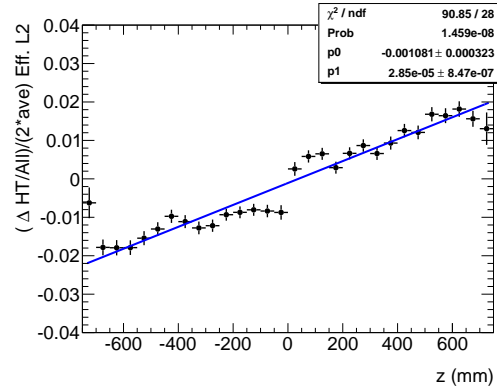


FIGURE 4.5: The relative change ($\Delta HT_{ratio} / (2 \times \text{ave } HT_{ratio})$) for Period E 2012 Data for Layer 2

layers with gas coming into the detector from the outer radius (center of the wheel) are defined as gasIN (gasOUT). Studies are performed separately for end-cap A A-type and B-type wheels and end-cap C A-type and B-type wheels. The distributions

of HT_{ratio} as a function of the radius is shown in Figure 4.6. The difference of the HT_{ratio} for the gasIN group and gasOUT group, normalized by twice the average value for the full segment of the detector, is plotted as a function of the radius. This ΔHT_{ratio} vs r for end-cap A is shown in Figure 4.7.

A positive slope indicating a decrease in HT_{ratio} along the direction of gas flow is seen in the end-cap A-type wheels. The end-cap B-type wheels have a negative slope after a dip at large r . This is inconsistent with the effect in the barrel and end-cap A-type wheels and is due to gas flow directions being installed reversed from the design in the B-Type wheels. The slope reverses at a radius of 900 mm, this could be due to a dip in temperature from the coolant system. A study of the temperature in the end-cap wheels using the temperature probes would be useful to confirm this. A fitted slope value for a range of 650 mm to 925 mm in radius is used for the monitoring studies for the time being due to lack of information of the temperature in the end-cap wheels during running time. ³.

The fitted slope values of ΔHT_{ratio} as a function of z/r are used to monitor the wire aging effect, and are referred as aging parameters in the rest of this Chapter.

³ Another difference between barrel and end-caps is that the gas input is always higher than the gas output (slope does not cross the axis). This is most likely due to the fact that the gasIN wheels are at a smaller $|z|$ than the gasOUT wheels, which indicates that there is a possible dependence on $|z|$ in the end-caps that needs to be studied in the future.

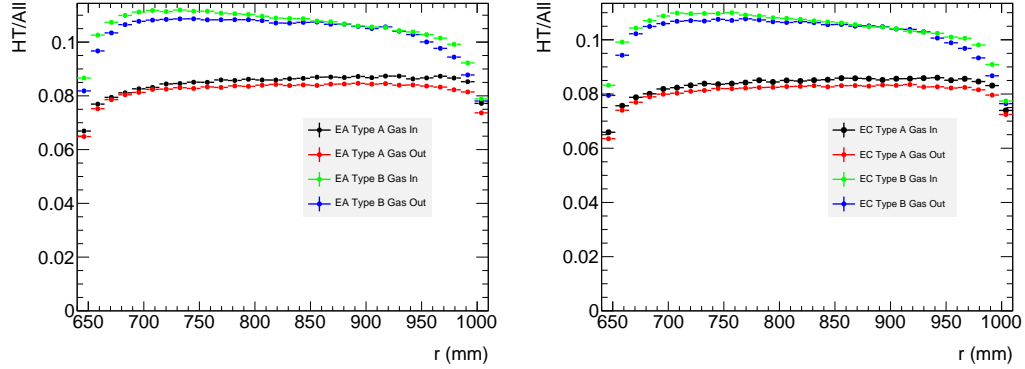


FIGURE 4.6: HT_{ratio} as a function of hit r for Period E 2012 Data end-cap A (left) end-cap C (right).

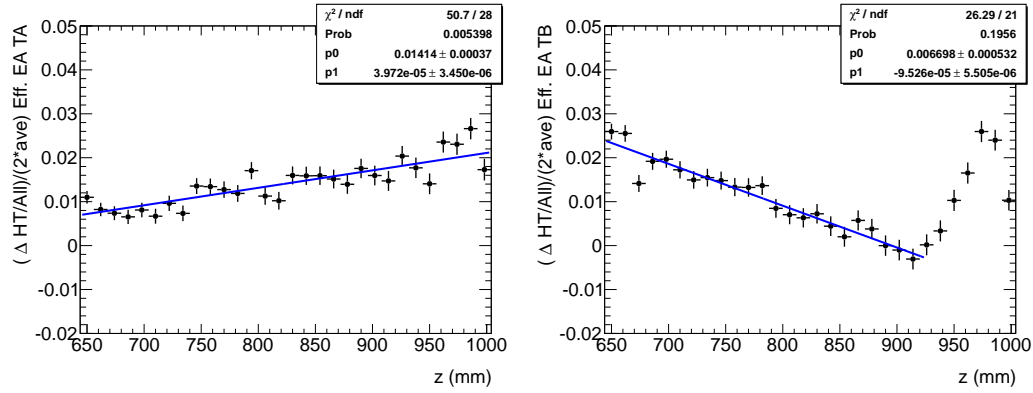


FIGURE 4.7: $\Delta HT_{ratio} / (2 \times \text{average } HT_{ratio})$ for Period E 2012 Data in end-cap A. The left plot is for type-A wheels and the right plot is for type-B wheels.

Ozone accumulation

Ozone accumulation in the gas could also cause a decrease in HT_{ratio} in the TRT straws. When a track ionizes the gas, oxygen molecules in the gas can absorb the free electrons and form ozone molecules which are drawn closer to the wire due to the voltage difference. This would result in a decrease in the gas gain leading to a drop in the HT_{ratio} . Since ozone molecules can be carried down the straw in the direction of the gas flow, this would cause an effect similar to wire aging.

The difference between ozone accumulation and wire aging is that ozone accumulation gets reset between runs. Therefore a scan over the integrated luminosity within a run is performed and the fitted slope values are calculated for each luminosity slice to study the ozone accumulation curve. We expect to see little to no effect in the first luminosity bin, then an increase in the slope is expected to be seen due to ozone accumulation. Eventually ozone accumulation reaches saturation and we should see a drop in the slope. Scans over many runs are combined to get decent statistics. Results are shown in Figure 4.8. The slope value increases in the beginning of runs, saturates and stabilizes, indicating a visible ozone accumulation.

Aging parameter dependence on run conditions

In a hadron collider experiment, the detector performance has a strong dependence on the machine running conditions. The run conditions at the LHC are often changing. It is thus important to check if the aging parameter chosen has a dependence on the running conditions and understand the dependence if any, in order to isolate aging effects.

The dependence of the aging parameter on the colliding beams pile up conditions is examined. Pile up is measured by the average number of proton-proton interactions per bunching crossing $\langle\mu\rangle$. Aging parameters are calculated for data slices with different requirements on the pile up conditions (with a $\langle\mu\rangle$ range of [0,10],

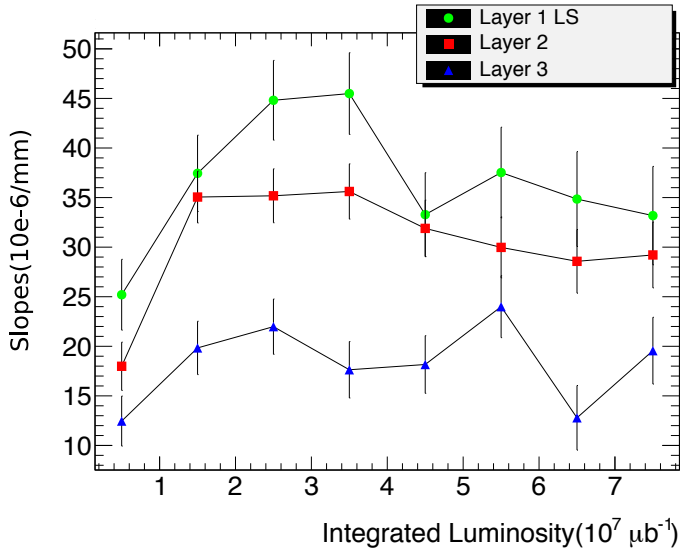


FIGURE 4.8: Ozone accumulation effect for the Barrel. The increase in the slope value indicates a decrease in the HT_{ratio} along the gas flow direction due to the gas gain drop caused by ozone accumulation. The accumulation stabilizes later in the run.

[14,16],[19,21],[24,26], [29,31]). The results are shown in Figure 4.9. No obvious dependence on $\langle \mu \rangle$ is observed.

To further understand the relation between instantaneous luminosity and fitted slopes, data from period B⁴ was divided into low instantaneous luminosity runs and high instantaneous luminosity runs. As shown in Table 4.2.2, runs with higher instantaneous luminosity have somewhat higher central values for the fitted slopes but are within the statistical uncertainties. More statistics in future LHC runs will help understanding this dependence better. This observation is suspected to be correlated with the ozone accumulation. A comparison of the ozone turn-on curve between runs with high instantaneous luminosity and runs with low instantaneous

⁴ Another period of data from 2012. There was a run condition change in this period, resulting two categories of data with different instantaneous luminosity features.

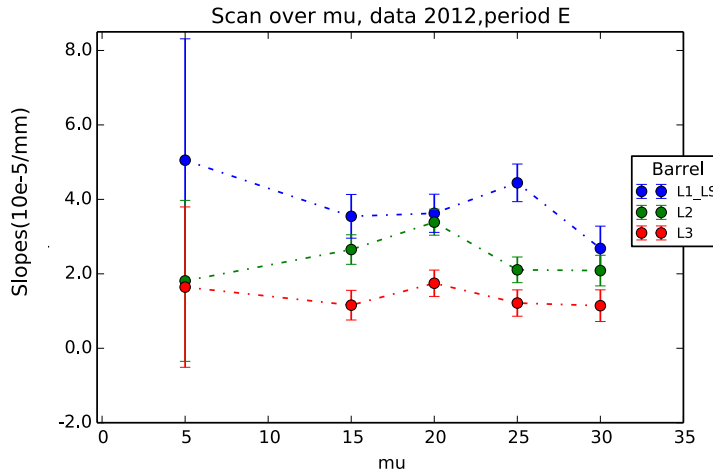


FIGURE 4.9: Fitted slopes as a function of μ for Period E 2012 Data for the barrel

luminosity is also shown in Figure 4.10. No obvious dependence of the ozone turn-on curve on instantaneous luminosity is observed.

Table 4.1: The aging parameters (10^{-5}) for runs with low instantaneous luminosity and runs with high instantaneous luminosity from Period B.

	Layer 1 LS	Layer 2	Layer 3
High	3.40 ± 0.11	2.07 ± 0.07	1.27 ± 0.07
Low	3.29 ± 0.10	2.01 ± 0.07	1.22 ± 0.07

4.2.3 Summary of wire aging studies

The aging studies described above were performed for all data taken in 2012⁵. Results are plotted as a function of integrated luminosity in Figure. 4.11. The jump from period A to period B is likely due to the instantaneously luminosity change as it is easy to argue that a straw aging effect would not happen within a short period of time,

⁵ Data taking is separated into periods of A to J in 2012, studies were performed per period due to considerations of decent statistics and stable run conditions.

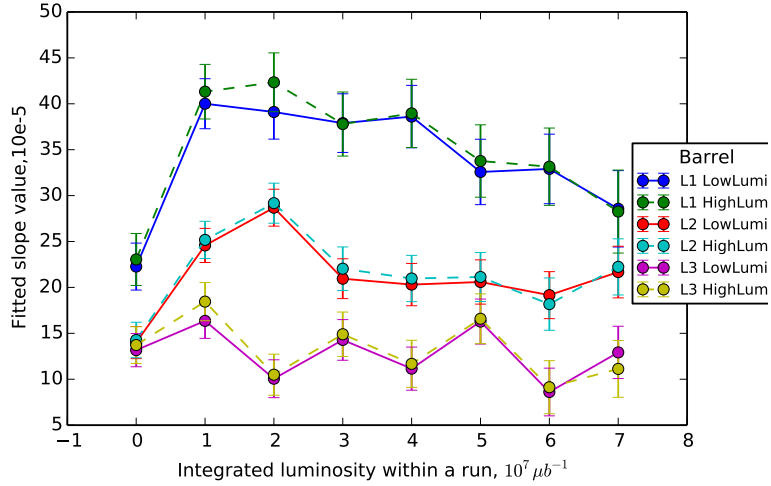


FIGURE 4.10: Ozone accumulation for runs with different instantaneous luminosity for period B 2012. Dashed (Solid) lines are for runs with low (high) instantaneous luminosity.

as it is expected to be a long-term effect. Although an increasing trend is observed for all sectors of the detector, it is possible that the effect is partially due to an accumulation of ozone instead of an aging effect. The turn-on curve observed in the scan over slices of integrated luminosity within a run indicates the presence of ozone. The extent of the effect due to ozone is unknown and difficult to quantify. Therefore another approach was adopted in order to isolate ozone accumulation effect. The trend for the fitted slope value for the first $10^7 \mu b^{-1}$ (corresponding to the first 30 mins of each run) before a large amount of ozone is accumulated is plotted. As shown in Figure 4.12, no obvious rising trends of the aging parameter were observed. Data from the next run of the LHC with higher statistics could help to distinguish between ozone and aging, and their dependence on instantaneous luminosity condition.

4.2.4 Monitoring the TRT in future LHC runs

Wire aging is one of the main concerns for the TRT operation over time. A method using the difference of the fraction of HT hits over all hits between detector segments

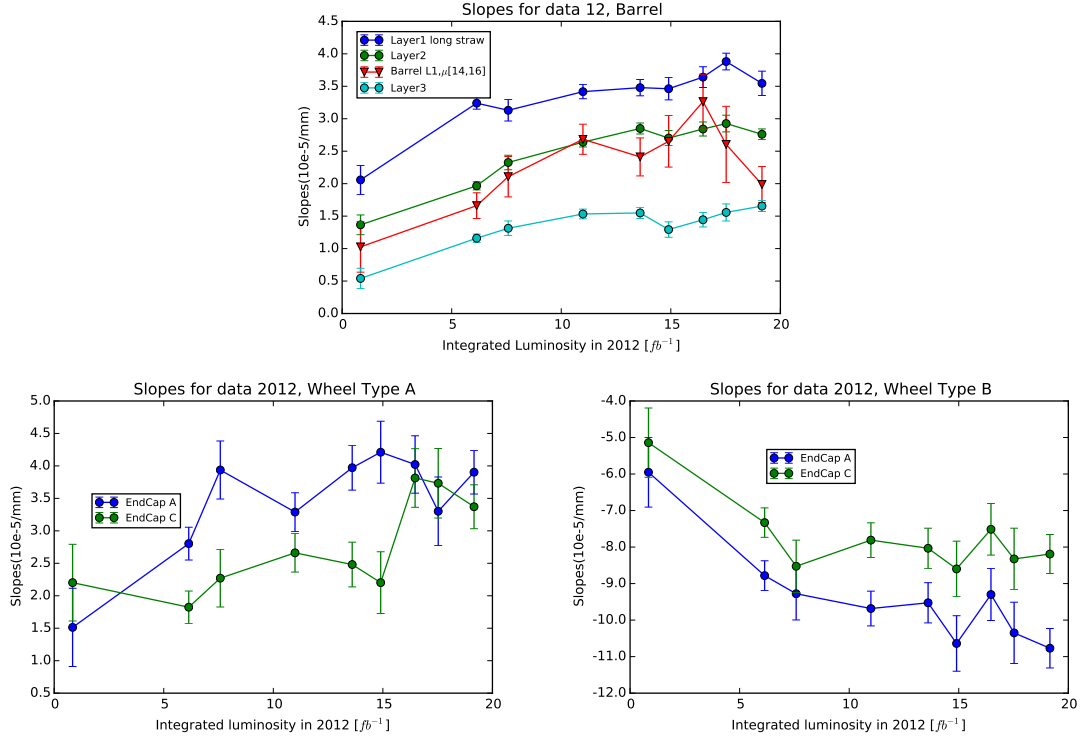


FIGURE 4.11: Aging monitoring study on data taken in 2012, plotted as a function of integrated luminosity. The top plot is for the barrel and the bottom left (right) is for wheel-type A (B).

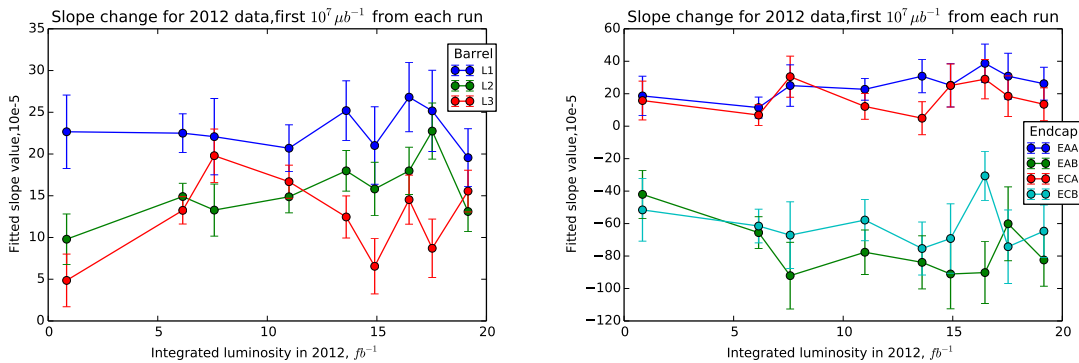


FIGURE 4.12: Aging monitoring study for data from the beginning of each run of 2012. The left (right) plot is for the barrel (end-cap).

with two different gas input directions was created in order to monitor a degradation of the signal detection efficiency from TRT straws. The fitted slope to the normalized

difference (normalized to the average HT_{ratio} value for the detector segment) distribution is proposed as the parameter to quantify the aging effect. Its dependence on the ozone accumulation, and run conditions such as average interaction number per bunch crossing and instantaneous luminosity were studied. Future studies of the ozone accumulation dependence on the run conditions will help better separating wire aging from ozone effect.

The program for monitoring aging effects that has been developed will be integrated into part of the TRT monitoring procedure. The aging monitoring will be regularly performed and further developed in the next run of the LHC. Since the TRT detector will be used until a scheduled upgrade of the ATLAS detector around 2020, such a monitoring program is essential over the next 10 years of TRT running.

4.3 Plans for the replacing the ATLAS Inner Detector in Phase 2 upgrade

One of the most important projects in the Phase 2 upgrade described in Chapter 3 is the replacement of the inner tracker. The current one will not be suitable for long term operation with increased luminosity and the accumulated radiation damage. The whole ID needs to be replaced with a new all-silicon tracker to maintain tracking performance in the high occupancy environment and to cope with the increased radiation. New technologies are used to ensure that the system can survive this harsh radiation environment and to optimize the material distribution. A new readout scheme that allows the implementation of a track trigger, contributing to the improvements in the ATLAS triggering capabilities, will also be exploited. The contributions I made to the testing facilities located at CERN will be presented in this Section.

4.3.1 ATLAS Inner Tracker for HL-LHC

The baseline layout of the new ATLAS inner tracker for HL-LHC is shown in Figure 4.13. The silicon strip detector consists of a central barrel region between ± 1.3 m and two end-caps that extend the length of the strip detector to ± 3 m. They cover a rapidity range of ± 2.5 . The barrel consists of five long cylinders that surround the beam-line and a short barrel that covers the loss of acceptance between the end-cap and barrel. The layers are populated with 472 full length staves (236 on each side of $Z = 0$). Each stave has 26 modules (13 on each face). The strips on the inner three cylinders are 24 mm long (short-strips) and those on the outer two cylinders and stubs are 48 mm long (long-strips).

A stave is the basic mechanical element of the barrel. It consists of a central core that provides mechanical rigidity and support for the modules, and contains the electrical, optical and cooling services. The readout interface to the stave is the End-Of-Stave (EOS) card. Small versions of short strip staves with 4 strip modules instead of 13 ("stavelets") have already been developed for tests. A layout of a stavelet is shown in Figure 4.14. The basic electrical unit of a stave is called a module. Application specific front-end chips ("ABC130") are mounted on kapton circuits to make a hybrid. One or two hybrids are glued to the surface of a silicon detector to form a module as shown in Figure 4.14.

4.3.2 Particle detection with silicon strips

In order to understand the important features of a silicon strip detector, I will give a brief introduction to the design of the silicon strip sensor and the principles of using silicon as a particle detection medium. An illustration of a strip sensor can be found in Figure 4.15. The bulk material of the SCT sensors is n-type semiconductor. The diode is formed by implanting a thin layer of extra-highly doped p-type semiconduc-

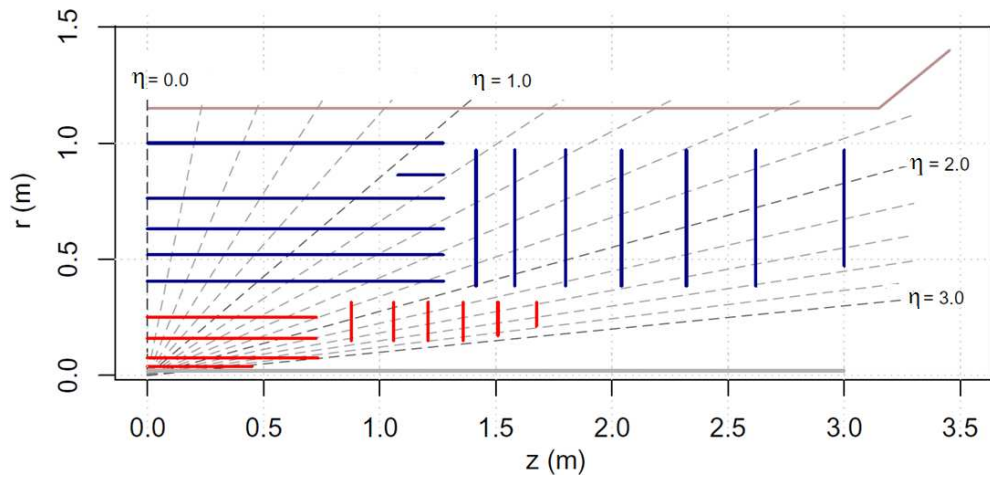


FIGURE 4.13: Baseline layout of new ATLAS inner tracker (active areas) for HL-LHC.

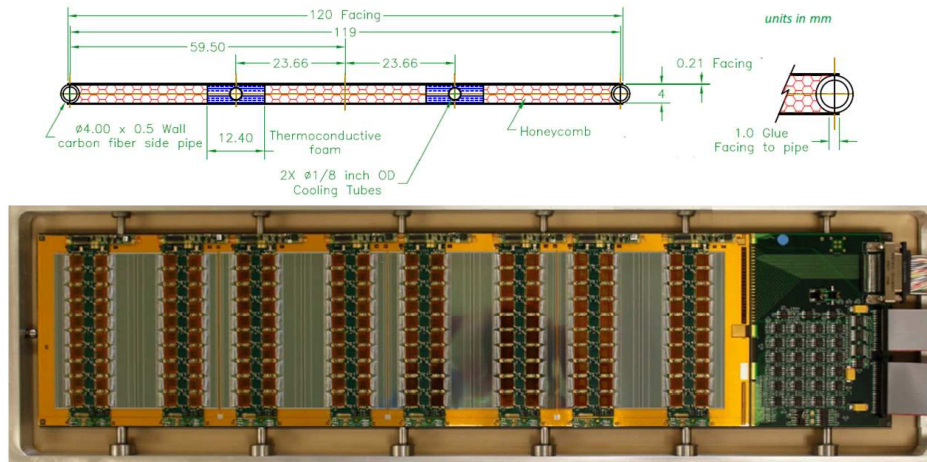


FIGURE 4.14: Shortened version of full stave, "stavelet". The stavelet width is 12 cm.

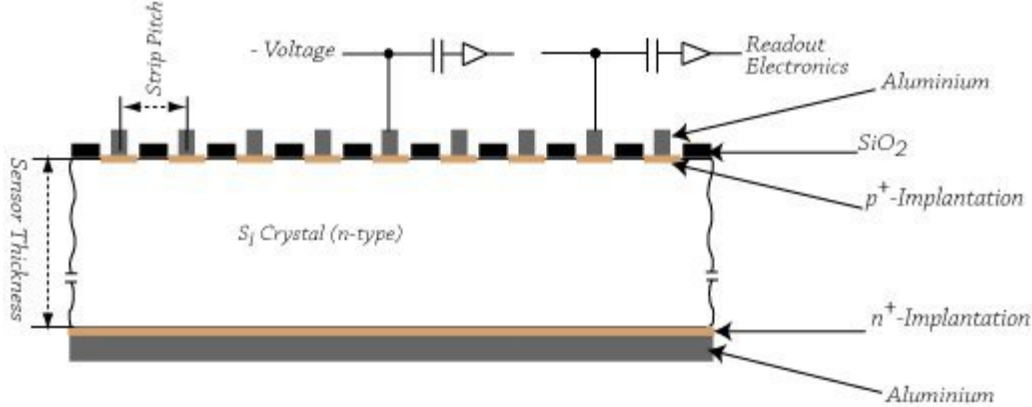


FIGURE 4.15: A silicon strip sensor.

tor⁶. A p-n junction forms when a p-type and a n-type semiconductor material are brought together. When a p-n junction is formed, there are uncompensated negative ions, therefore a depletion region (i.e., depletion of mobile carriers) is formed at the junction. This region, in turn, creates an electric field. At thermal equilibrium, the drift current due to the electric field is exactly balanced by the diffusion current due to concentration gradients of the mobile carriers on the two sides of the junction. When a positive voltage is applied to the p-side with respect to the n-side, a large current will flow through the junction. However, when a negative voltage is applied, virtually no current flows, referred as reverse bias current, until the breakdown voltage threshold. This behavior is the most important characteristic of p-n junctions. A charged particle traversing the silicon ionizes it, creating conduction electrons and holes, which drift to the electrodes inducing a current. This current is detected and since it is associated with a strip, the position where the particle traversed the sensor is determined.

⁶ Silicon has four valence electrons. Doping introduces impurities into a pure semiconductor for the purpose of modulating its electrical properties. By doping pure silicon with Group V elements such as phosphorus, extra valence electrons are added that become unbonded from individual atoms and allow the compound to be an electrically conductive n-type semiconductor. Doping with Group III elements, which are missing the fourth valence electron, creates "broken bonds" (holes) in the silicon lattice that are free to move. The result is an electrically conductive p-type semiconductor.

The performance of silicon strip detectors can be described by its signal-to-noise ratio (SNR). It is important to test and understand the performance in a high fluence radiation environment. Noise can be generated from external sources (grounding design for example) or from the detector design (reverse bias current etc). Noise levels can be measured with a three point gain test that will be described later. Since the energy deposited in the detector translates directly into charge, it is convenient to express the electronic noise as an Equivalent Noise Charge (ENC). It is defined to be the number of electrons one would have to collect from a silicon sensor in order to create a signal equivalent to the noise of this sensor. ENC is commonly expressed in fC or units of the electronic charge $e = 1.602 \times 10^{19} C$.

4.3.3 Tests of silicon strip tracker components

A single module test system, stavelet test system and a CO_2 cooling system were constructed and operated at CERN. The test systems are used to test and configure the readout electronics and the data acquisition (DAQ) system. They can also help in comparing the performances of different stave prototypes (different powering schemes for example) to help with the stave design. Such test systems will also be essential in the irradiation tests of the assembled full staves to examine their radiation hardness as a unit. The layout and some test results for each system will be described.

A single module is the basic unit of a strip detector. Tests in understanding its performance are essential. Test results from the single module test stand system will be presented.

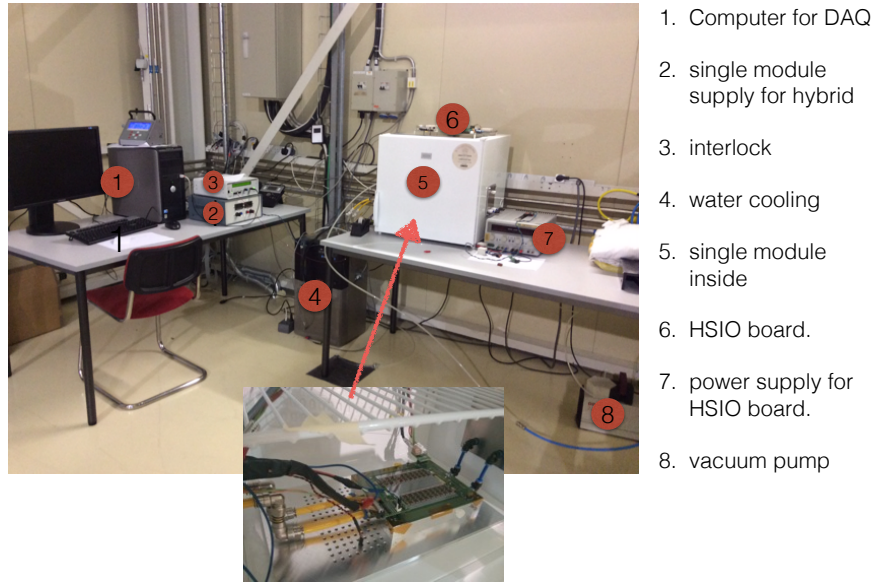


FIGURE 4.16: Test system for a single module at CERN.

Single module test system.

The single module test system located at CERN is shown in Figure 4.16. Each component is labeled in the Figure. The following tests were performed in order to test the noise level:

- **StrobeDelay**

The calibration strobe sets the timing (delay) of the calibration pulse injected into the module with respect to the time of the command that actually triggers the pulse. This ensures that the discriminators, always firing at the clock frequency, will be synchronous with the calibration signal. An optimal setting of the strobe delay for each chip is important for the accuracy of the threshold calibration. If the delay in injecting the test charge is too short, then the discriminator will fire too late and won't record a hit. If it is too long, the discriminator fires too early and will not capture the injected charge. The delay of the strobe can be tuned for individual chips within a range of 50 ns. The difference in the strobe delays between two adjacent

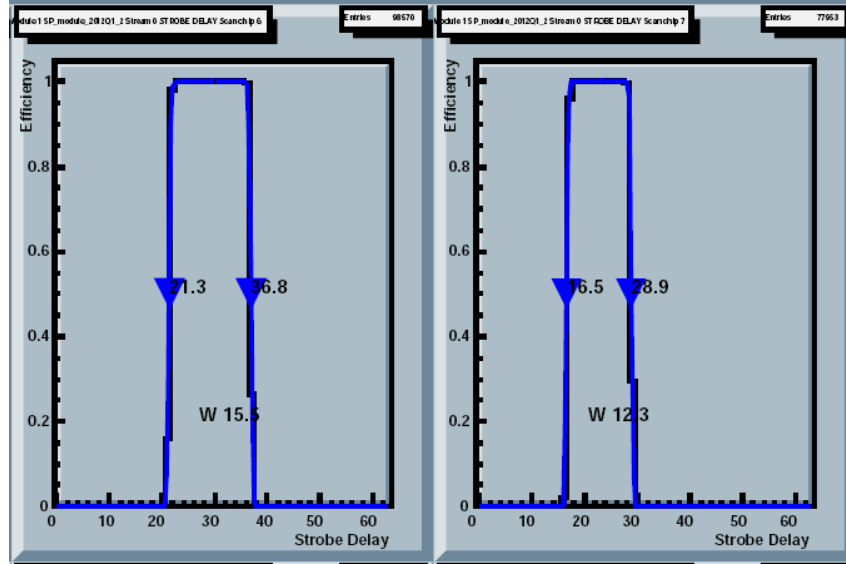


FIGURE 4.17: Strobe delay versus efficiency for two adjacent chips.

chips is shown in Figure 4.17.

- ThresholdScan

The output of a channel for a given input of charge is measured as the threshold is varied. The channel's response to an injected charge is to record a "1" (hit) or a "0" (no hit). The occupancy, defined as the ratio of the number of hits detected over the total number of hits injected, of each channel is measured over a given range of thresholds settings with a large sampling for each threshold setting. The occupancy is then plotted as a function of the varied threshold as shown in Fig 4.18. At low thresholds all the events return a hit (occupancy at 100%) since the input signal at the discriminator is likely to be above threshold. As the threshold is increased, the occupancy of the channels is reduced. When the threshold raises above the level of the input signal, the occupancy continues to fall until it reaches zero. Ideally this S-curve would have a shape of a step function immediately falling to 0 (no hit) as soon as the threshold is raised above the input signal level. In reality this shape is

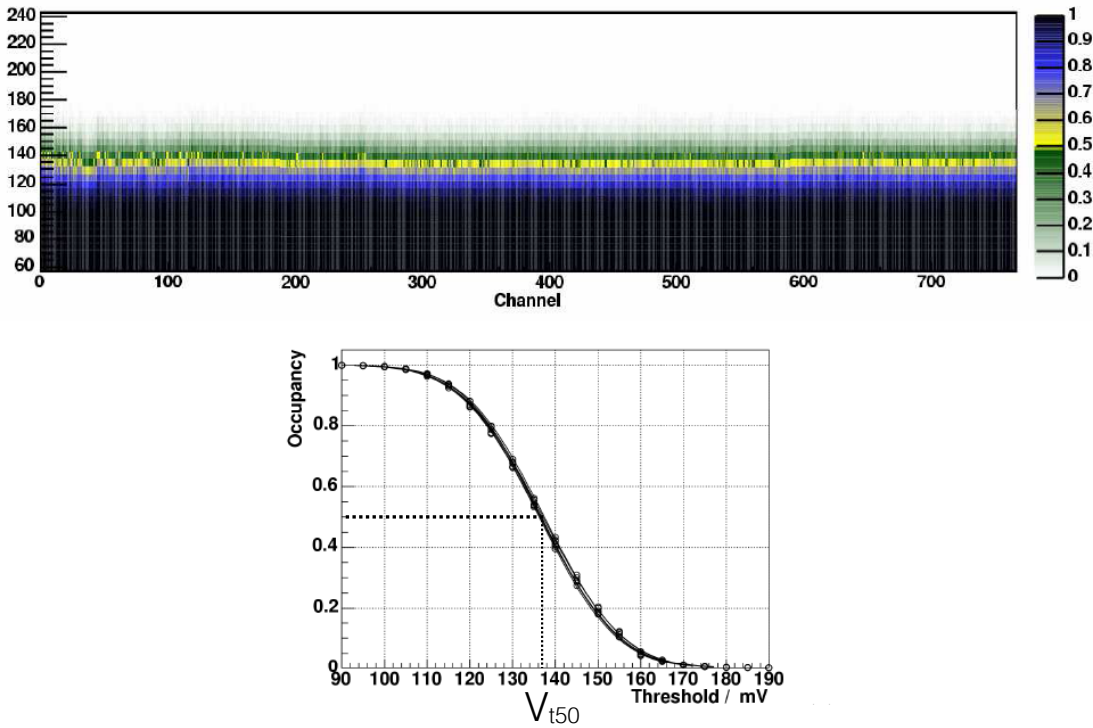


FIGURE 4.18: Threshold scan. The threshold scan as a function of the channel number and the threshold scan for a single channel are shown.

smeared due to the noise in the system. A V_{t50} point is defined to be the threshold voltage with an occupancy of 50 % as shown in Figure 4.18

- ThreePointGain

These tests are made with a threshold scan each with 3 different levels of injected charge. There are two options for this test: 3PointGain@1fC and 3PointGain@2fC, which refer to injected charges 0.5fC, 1fC, 1.5fC and 1.5fC, 2fC, 2.5fC. The result of the V_{t50} points versus injected charges is shown in Figure 4.19. The purpose of this test is to study the performance of the modules with respect to a set of parameters:

- V_{t50} as shown in Figure 4.18.

- The output noise, defined to be the variance σ of the distribution of the threshold V_{t50} (mV) for a particular injected charge (fC).
- The gain (G), measured in mV/fC, is calculated from a linear fit to V_{t50} versus injected charge as shown in Figure 4.19.
- The Equivalent Noise Charge (ENC), measured in units of e, is the result of dividing the output noise by the gain and converting the input noise in fC to electrons ($1\text{fC} = 6250 \text{ e}$, $\text{ENC} = \sigma/G \times 6250 \text{ e}$).

The results of the three point gain test are calculated for individual channels, allowing extraction of the ENC per chip, per hybrid or for the whole module as shown in Figure 4.20.

- Response curve

The response curve is an extension of the three point gain test to 10 scan points, where the injected charge is set to 0.5, 0.75, 1.0, 1.25, 1.5, 2, 3, 4, 6 and 8fC. This test is used to get a more precise measurement of the gain. A quadratic fit to a response curve can be seen in Figure 4.21. It shows the non-linearity of the pre-amplifier in the chips when the input signal increases.

Stavelet test system.

The stavelet test system is shown in Figure 4.23. At the time of writing this thesis, there is no dedicated design for the grounding of the cooling pipe, and the noise level that could be introduced through ground loops. Therefore a test was made using external noise generated by a function generator injected into the system through the cooling pipe. The three point gain test results were compared with and without external noise introduced. Some tests results for a module closer to the end of the stavelet (where external noise is injected into the system) are shown in Figure 4.22. The noise level is observed to increase with injected external noise. Therefore a

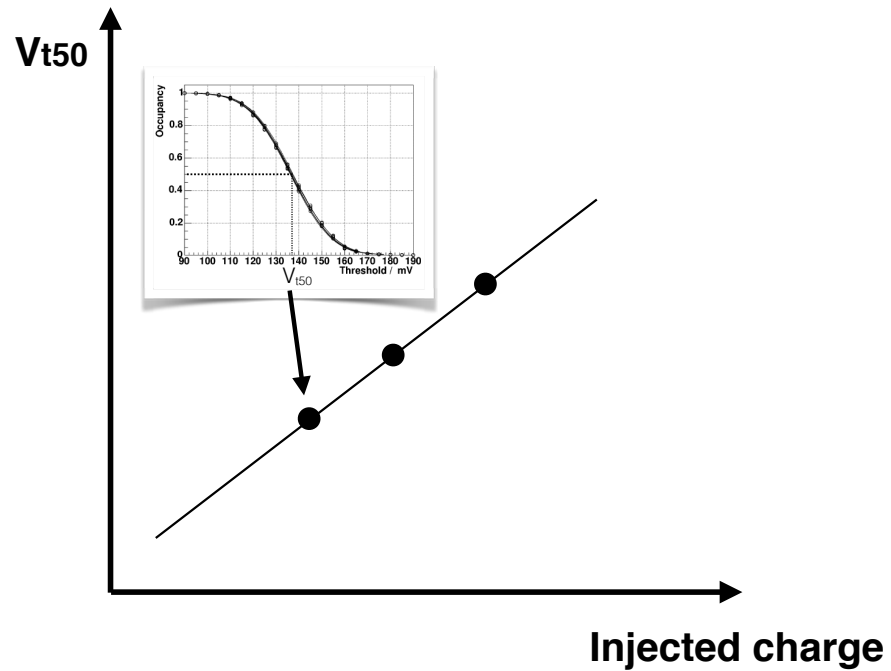


FIGURE 4.19: Three point gain test.

dedicated grounding design of the cooling pipe is needed.

CO₂ cooling system.

A cooling system using CO_2 liquid was constructed for tests of staves with more robust cooling power and safety concerns. The basic principle of cooling is that CO_2 liquid at room temperature enters the cooling pipe and evaporates into gas, absorbing heat during the phase transitions.

The thermodynamic cycle of the system is given in the pressure-enthalpy diagram in Figure 4.26, with the numbers matched to different parts in the system shown in the Figure 4.25. The continuous green line is the system cycle. The dashed line

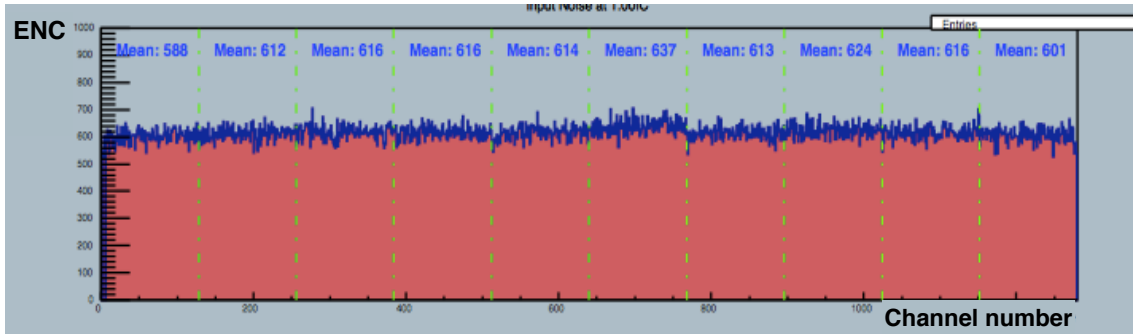


FIGURE 4.20: ENC result for one hybrid from the 3 point gain tests.

is the cycle for a system with a compressor for compressing CO_2 gas to liquid. The overheated vapor is heated to room temperature and expanded to atmospheric pressure and then vented. The cooling ability of this system is shown in Figure 4.27. The humidity, temperature and dew point for two sensors located at two ends of the container are shown as a function of time. The system was found to run stable at $10^\circ C$ for about 3 hours with one bottle of CO_2 liquid.

The CO_2 cooling system will supply sufficient cooling for a full sized stave. The readout electronics and data acquisition system have been configured with the single module and stavelet test facilities. Performances of different designs can be tested and compared using these systems. These testing facilities will also be essential in examining the radiation hardness of the proposed detector design.

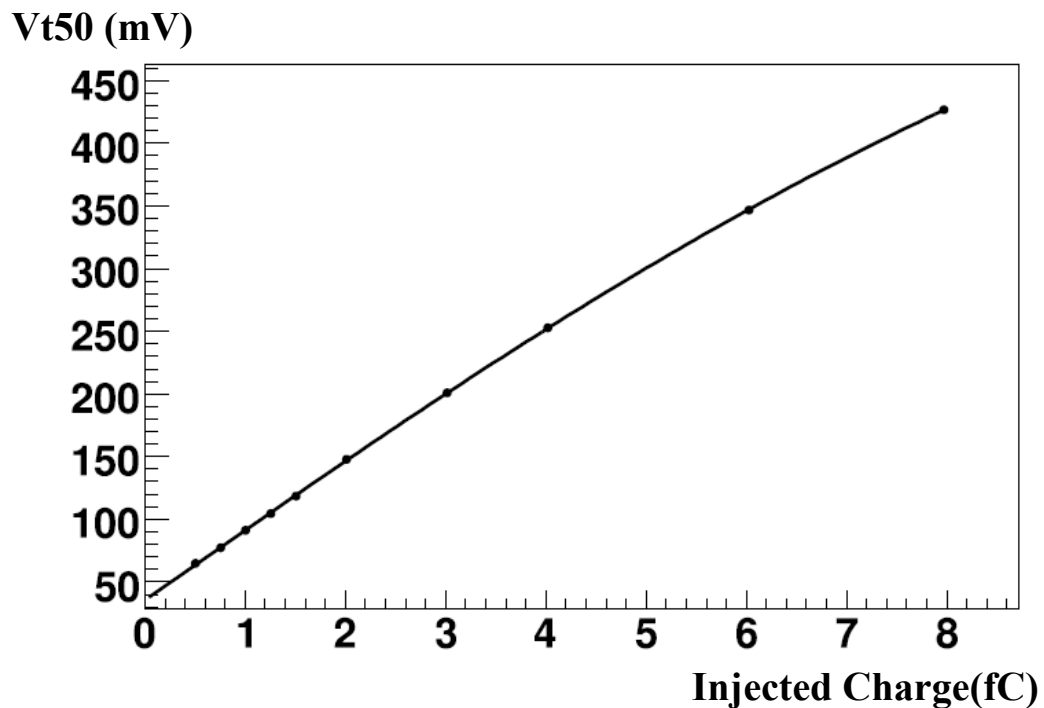


FIGURE 4.21: Response curve measurement result for one chip.

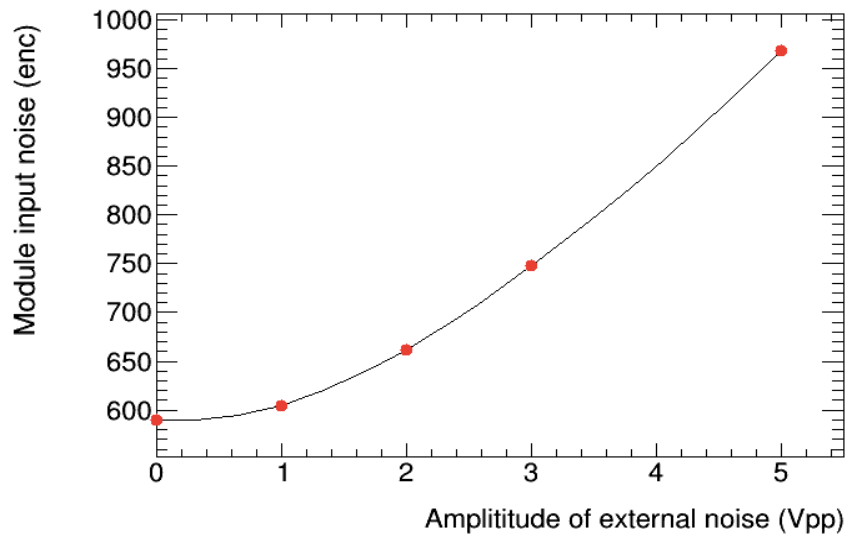


FIGURE 4.22: Noise injection to the cooling pipe test.

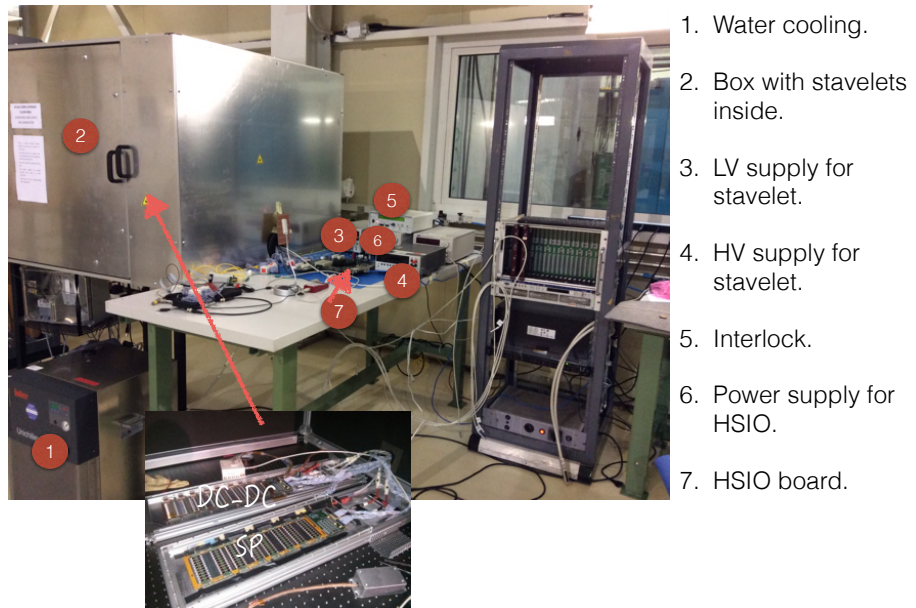
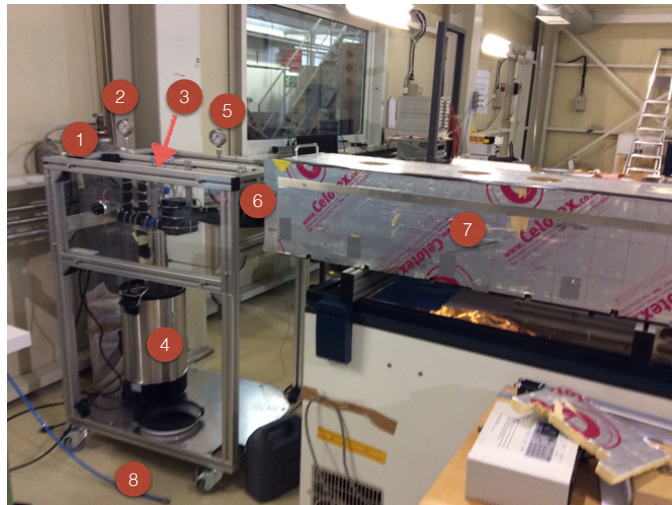


FIGURE 4.23: Test system for a stavelet.



1. CO₂ bottle
2. Input pressure meter.
3. Back pressure valve.
4. Water boiler.
5. Output pressure meter.
6. Throttle valve
7. Box: dummy stavelet inside.
8. Dry air.

FIGURE 4.24: Diagram of the CO₂ cooling system.

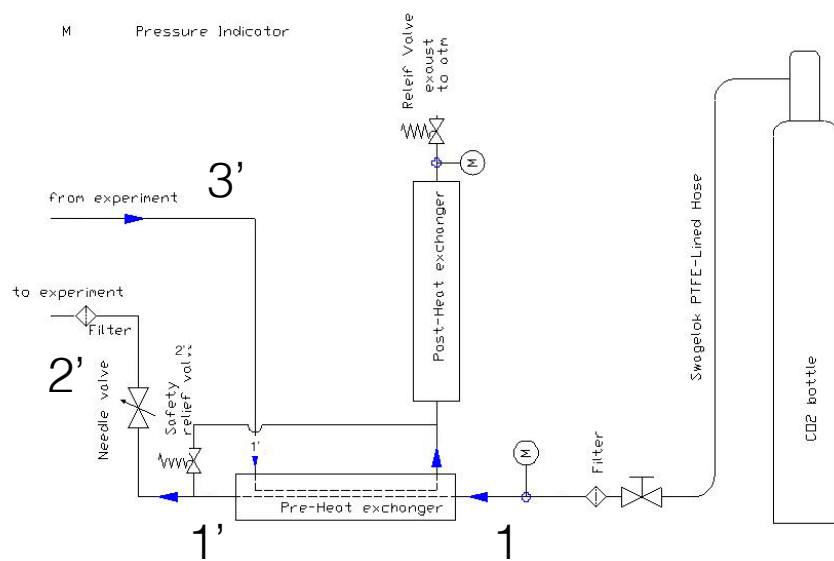


FIGURE 4.25: CO₂ cooling system.

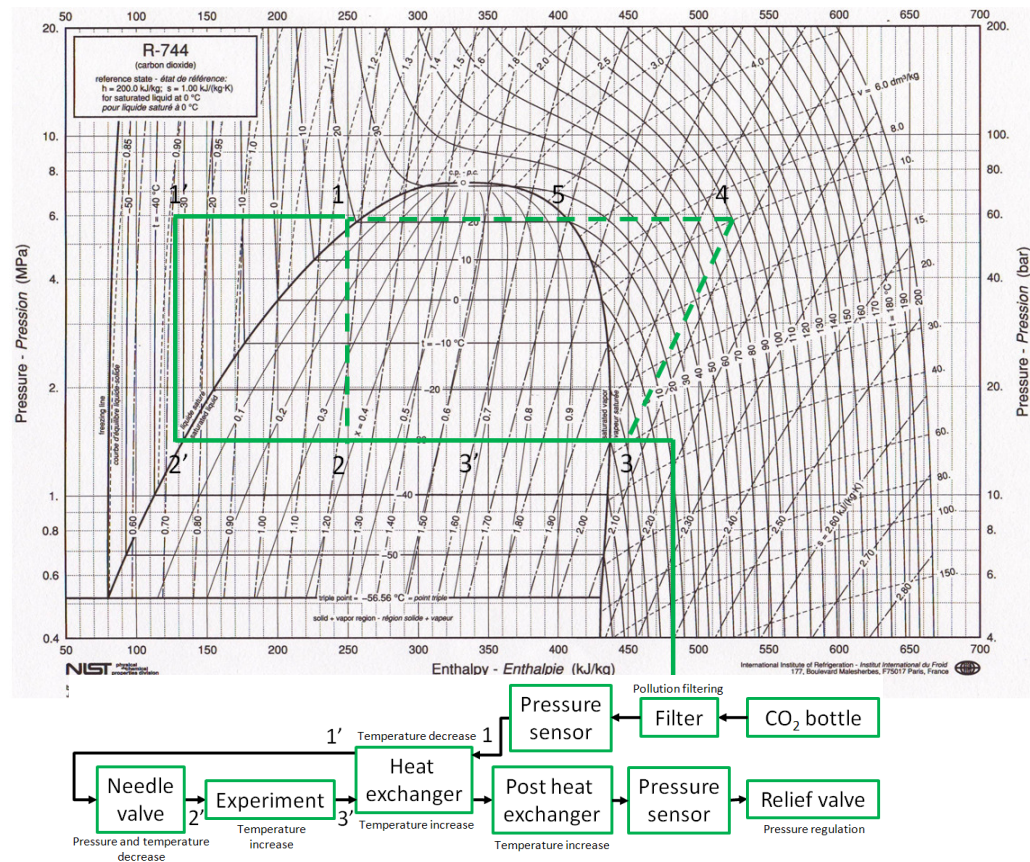


FIGURE 4.26: The thermodynamic cycle of the CO₂ cooling system.

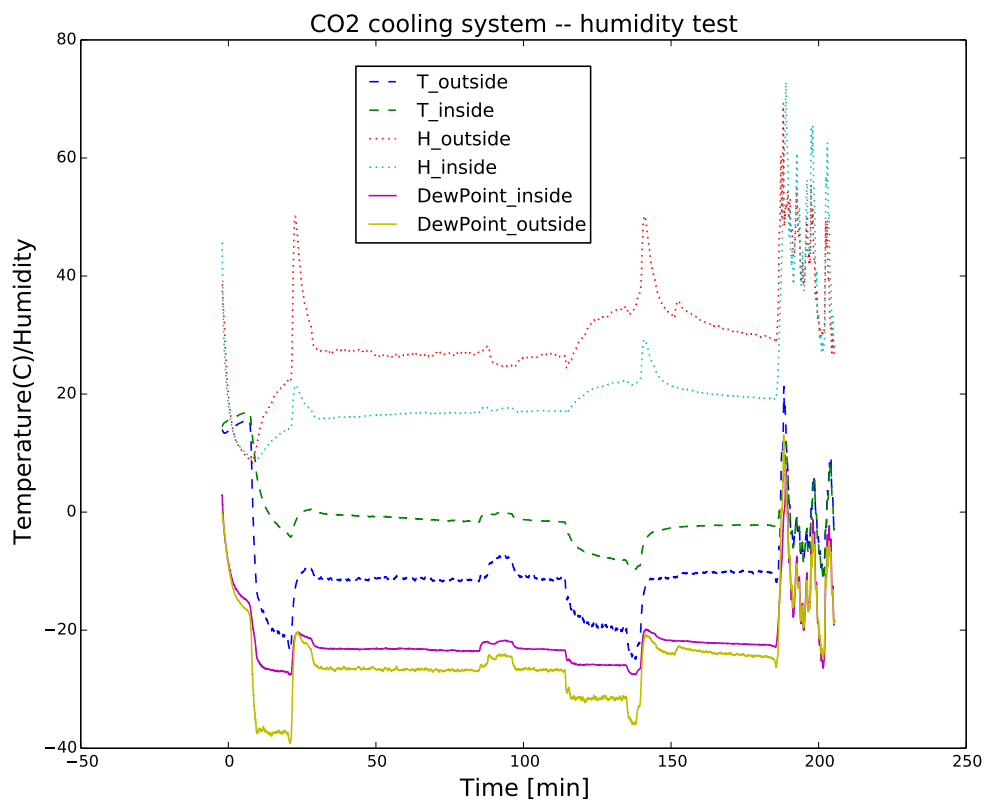


FIGURE 4.27: Test results for CO₂ cooling system, two sensors were used in the test, one located at the end where the cooling pipe enters the box (outside), the other one located at the other end (inside) where the cooling pipe goes out of the box. T stands for temperature and H stands for Humidity.

4.4 Summary

A procedure designed to monitor the TRT performance during the next 10 years of operation has been described in this Chapter. Studies of the data taken in 2012 show no sign of wire aging. The TRT is scheduled to be replaced with a silicon strip tracker in the phase 2 upgrade of the ATLAS detector. My contributions to the testing facilities used for designing the new tracker have been presented.

5

Measurement of $pp \rightarrow W\gamma\gamma + X$ Production

A measurement of $pp \rightarrow W\gamma\gamma + X$ production will be presented in this Chapter. The analysis is performed on a dataset from proton-proton collisions collected by the ATLAS detector in 2012, corresponding to an integrated luminosity of 20.3 fb^{-1} . In Section 5.1, the data and Monte-Carlo (MC) simulated samples used in this analysis will be introduced. In Sections 5.2 and 5.3, the event selection and data driven background estimates are described, leading to the $W\gamma\gamma$ signal extraction.

5.1 Data and Simulated samples

This analysis is based on a data sample of proton-proton collisions collected at $\sqrt{s} = 8$ TeV during 2012. As electron and photons are present in the final state, the dataset triggered by electromagnetic objects is used.

As introduced in Chapter 2, for the Standard Model simulation of the signal, the leading order generators **ALPGEN** [22] and **SHERPA 1.3.1** [24] are used. The **ALPGEN** samples are generated with up to five additional jets while **SHERPA** generates up to three. All generated events are then passed through full detector simulation.

5.2 Event Selection

To select $W\gamma\gamma$ events with the W boson decaying into an isolated electron and a neutrino, an event is required to have a high p_T electron, large missing transverse energy and two isolated high p_T photons. Additional selections are carefully chosen to ensure good data quality and optimize the significance of the final state of interest.

They will be introduced in three categories based on their purposes:

- Event quality requirements : These are criteria common to most analyses performed by the ATLAS collaboration.
- Triggering and object definitions : Selection of events and definitions of objects (particles) are chosen to ensure high signal efficiency and quality.
- Additional kinematic cuts: These are studied and optimized to improve background suppression.

5.2.1 *Event quality requirements*

Data is selected from the LHC pp collisions for which the ATLAS detector sub systems were operating normally. LHC run conditions, detector performance and

other operational issues were recorded in the Good Runs List (GRL) in intervals of luminosity blocks. Luminosity blocks (LB) are defined as time intervals with most parameters entering integrated luminosity calculation, instantaneous luminosity for example, being constant. One LB contains roughly 2 minutes of data taking, but this can vary due to run conditions and other operational issues. All events accepted are required to pass the GRL requirement. No selection is applied to simulated events at this stage.

The average number of interactions per bunch crossing, μ , is measured for each LB. The simulated distribution of μ is reweighed to reproduce the one in data. Events are also required to have at least one reconstructed hard scattering vertex with three or more associated tracks with $p_T > 0.4$ GeV. If more than one vertex is reconstructed, the sum of the transverse momenta of all its associated tracks is calculated for each vertex, and the one with the highest sum is chosen to be the primary vertex.

5.2.2 Triggering and object definitions

In the electron channel, the candidate events are preselected by a trigger which requires three electromagnetic objects (EM) with transverse energy greater than 15 GeV (“3g15_loose”). A measurement of the trigger efficiency using data driven techniques is documented in appendix A. Definitions of the particles present in the final state $W(e\nu)\gamma\gamma$ (electron, photon, and missing transverse energy) will be introduced in the following sections.

Electron selection

Reconstructed electrons are required to pass the following requirements:

- The electron is required to have a cluster transverse energy (E_T^{el}) greater than 20 GeV, considering the threshold applied at the trigger level. The pseudo-rapidity of the electron energy cluster must be within the range $|\eta| < 2.47$,

where the crack region in the electromagnetic calorimeter, corresponding to $1.37 < |\eta| < 1.52$, is excluded.

- Calorimeter and tracking information are used to define different baseline electron identification criteria. A tight cut-based selection is used to ensure good quality of the selected electron [35].
- The electron track is also required to extend to the primary vertex of the interaction of each event. Requirements on the longitudinal and transverse impact parameters are imposed. Electrons are rejected if $|z_0 \cdot \sin \theta|^1$ coordinate is larger than 0.5 mm, or $|d_0|/\sigma(d_0)^2$ is larger than 6.
- Both track and calorimeter based isolation criteria are used for electrons to suppress hadronic jet contamination. The sum of the transverse momenta of all the tracks reconstructed in a cone within $\Delta R < 0.2$ ³ around the electron track is required to be smaller than 0.15 times the electron track p_T . In addition to this, the calorimetric isolation variable of the electron, defined as the ratio between the sum of the transverse energies deposited within $\Delta R < 0.2$ around the electron cluster and the electron E_T^{cl} , is required to be smaller than 0.2.

Photon Selection

Photon reconstruction and identification is seeded by clusters in the electromagnetic calorimeter with transverse energies exceeding 2.5 GeV, measured in towers of 3×5 cells in the second layer of the calorimeter. Clusters without matching tracks are directly classified as unconverted photon candidates. Clusters matched to tracks

¹ z_0 is the longitudinal impact parameter which is the z value at the perigee, θ is the polar angle, measured in the range $[0, \pi]$

² d_0 is the transverse impact parameter which is the distance of the closest approach (perigee) of the helix to the local z-axis, $\sigma(d_0)$ is the resolution of d_0 .

³ $\Delta R^2 = \Delta\phi^2 + \Delta\eta^2$, where $\Delta\phi = |\phi_{electron} - \phi_{track}|$, $\Delta\eta = |\eta_{electron} - \eta_{track}|$

originating from reconstructed conversion vertices seeded in the TRT or to tracks consistent with coming from a conversion are considered as converted photon ($\gamma \rightarrow e^+e^-$) candidates. The final energy measurement of the photon is made using EM clusters with 3×5 cells (3×7 cells) for non-converted photons (converted photons) in the barrel. In the endcap, a cluster size of 5×5 cells is used for all candidates.

Discriminating variables based on the calorimeter shower shapes are used in the photon identification. They are important in understanding the contamination due to hadronic jets being misidentified as photons and listed as below. The cut values are optimized and calibrated for datasets taken over different time intervals. Detailed studies of the cuts are documented in [36].

- A ratio of E_T in the first layer of the hadronic calorimeter to the E_T of the EM cluster is denoted as R_{had} . In the pseudorapidity range $0.8 < |\eta| < 1.37$ which is not covered by the first hadronic layer, it is the ratio of the E_T in the whole hadronic calorimeter to the electromagnetic E_T . An upper bound is set on R_{had} to reject showers deposited by hadronic jets with large electromagnetic energy deposit.

- **EM Calorimeter Middle Layer Variables:**

These variables are designed to select narrow electromagnetic showers.

- R_η : ratio in η of cell energies in 3×7 versus 7×7 cells.
- R_ϕ : ratio in ϕ of cell energies in 3×7 versus 7×7 cells.
- w_2 : lateral width of the shower.

- **EM Calorimeter First Layer (Strip Layer) Variables:**

These variables take advantage of fine granularity in the first layer of the EM

calorimeter to distinguish prompt photons from the photons coming from π^0 decay.

- w_{s3} : shower width for three strips around the maximum strip.
- w_{stot} : total lateral shower width.
- F_{side} : fraction of energy outside a core of 3 central strips, but within 7 strips.
- ΔE : difference between the energy of the strip with the second largest energy deposited and the energy of the strip with the smallest energy deposit between the two leading strips.
- E_{ratio} : ratio of the energy difference associated with the largest and second largest energy deposits over the sum of these energies.

For the $W\gamma\gamma$ analysis the two photon candidates are required to pass the following selections:

- A *tight* identification criteria imposing cuts on all of the variables listed above.
- A transverse energy greater than 20 GeV and $|\eta| < 1.37$ or $1.52 < |\eta| < 2.37$;
- The isolation transverse energy of the photon, defined as the transverse energy in a cone size of $\Delta R = 0.4$ surrounding the photon and excluding the photon core of $\Delta\eta \times \Delta\phi = 0.125 \times 0.175$ is required to be smaller than 4 GeV to suppress hadronic jets.
- A non-tight photon is also defined here for use in background studies: Photons that pass the selections on transverse energy and η are candidates as non-tight photon. They are required to fail at least one of the cuts on the four strip

variables F_{side} , w_{s3} , ΔE and E_{ratio} and pass cuts on the rest of the EM cluster variables. These background photon candidates will be used in data driven estimations of the major backgrounds. Details are described in Section 5.3.2.

Missing Transverse Energy

The Missing Transverse Energy (E_T^{miss}) requirement is used to select events containing a real W boson with a highly energetic neutrino. In order to reduce the contamination coming from events not containing a real neutrino, the selected events are required to have a minimum transverse missing energy (E_T^{miss}) larger than 25 GeV.

The physics objects used by the standard ATLAS reconstruction to build the E_T^{miss} are all calibrated objects. In addition, energy not associated with any physics object is also accounted for in the calculation, corresponding to the so-called soft term. Corrections (e.g. momentum smearing) are applied to leptons, photons and jets in detector simulations to better reproduce data. These are propagated into the E_T^{miss} calculation in the simulated sample. The overall missing energy in the x and y directions in the transverse plane is defined as follows:

$$-E_{x(y)}^{\text{miss}} = E_{x(y)}^{\text{miss},e} + E_{x(y)}^{\text{miss},\gamma} + E_{x(y)}^{\text{miss},\tau} + E_{x(y)}^{\text{miss,jets}} + E_{x(y)}^{\text{miss,softterm}} + E_{x(y)}^{\text{miss},\mu} \quad (5.1)$$

where each term corresponds to: electrons, photons, τ leptons, jets, soft energy deposits and muons respectively.

Jet definition and selection

Selected jets, reconstructed from topological calorimeter clusters using the anti- k_T algorithm [37] with a cone size of 0.4, are required to have $p_T > 30$ GeV at the hadronic energy scale⁴ and $|\eta| < 4.4$. Jets arising from detector noise or cosmic rays were rejected. Furthermore, the Jet Vertex Fraction (JVF), a measure of the

⁴ Hadronic energy scale calibrates the jets due to energy deposited by hadrons that is not measured by the calorimeter.

fractional p_T of the charged tracks which originate at the hard scatter vertex, is required to be larger than 0.5 for jets with transverse momenta below 50 GeV and $|\eta| < 2.4$ to suppress pile-up effects. Jets that overlap with selected leptons or photons, *i.e.* have $\Delta R(\ell/\gamma, \text{jet}) < 0.3$, are rejected.

5.2.3 Kinematic cuts

With the selection of electrons, photons and jets described above, we can now define the requirements used to isolate the $W(e\nu)\gamma\gamma$ signal events from the background. These are listed below:

- *W(eν) selection:*
 - Require an isolated electron with $p_T > 20$ GeV, passing the selection described above.
 - Events are rejected if there is a second electron with $p_T > 10$ GeV, passing all electron quality criteria discussed above with the tightest quality cut loosened to the medium one. This rejects $Z(ee)$ events with fake E_T^{miss} due to imperfect reconstruction and where one electron is misidentified as a photon due to missing matched tracks in the ID or hard bremsstrahlung of the electron.
 - Require $E_T^{\text{miss}} > 25$ GeV.
 - Require the transverse mass of the electron and neutrino system $M_T(e, \nu) > 40$ GeV.⁵
- *W(eν)γγ selection:* Once the event has passed the W boson selection, the event is required to have two isolated photons with $p_T > 20$ GeV, passing the selection described in Section 5.2.2.

⁵ $M_T(e, \nu)$ is defined as $M_T(e, \nu) = \sqrt{2p_T^{\text{el}}p_T^{\nu}(1 - \cos[\phi^{\text{el}} - \phi^{\nu}])}$.

Overlap removals among the objects are also applied. If one of the selected photons overlaps with a lepton, *i.e.* $\Delta R(\ell, \gamma) < 0.7$ with ΔR defined as $\sqrt{\Delta\eta^2 + \Delta\phi^2}$, then the photon is discarded to remove overlapped objects and reject photons radiated off leptons. Similarly if a jet overlaps with a photon or lepton, *i.e.* $\Delta R(jet, \ell \text{ or } \gamma) < 0.3$, the jet is discarded. A selection of $\Delta R(\gamma, \gamma) > 0.4$ is also applied, and the $W\gamma\gamma$ candidate is discarded if the two photons fail such a requirement.

Rejection of $Z(ee)\gamma$ background.

$Z(ee)\gamma$ events, with the photon radiated off the incoming quark (initial state radiation, ISR) or the electron (final state radiation, FSR), make a large contribution to the selected candidates with the cuts introduced above. A $Z(ee)\gamma$ event can fake a $W(e\nu)\gamma\gamma$ final state when one of the electrons is mis-identified as a photon. Although the fake rate is low, $Z(ee)\gamma$ production at the LHC is much higher than $W\gamma\gamma$, resulting in a sizable contamination in the selected candidates.

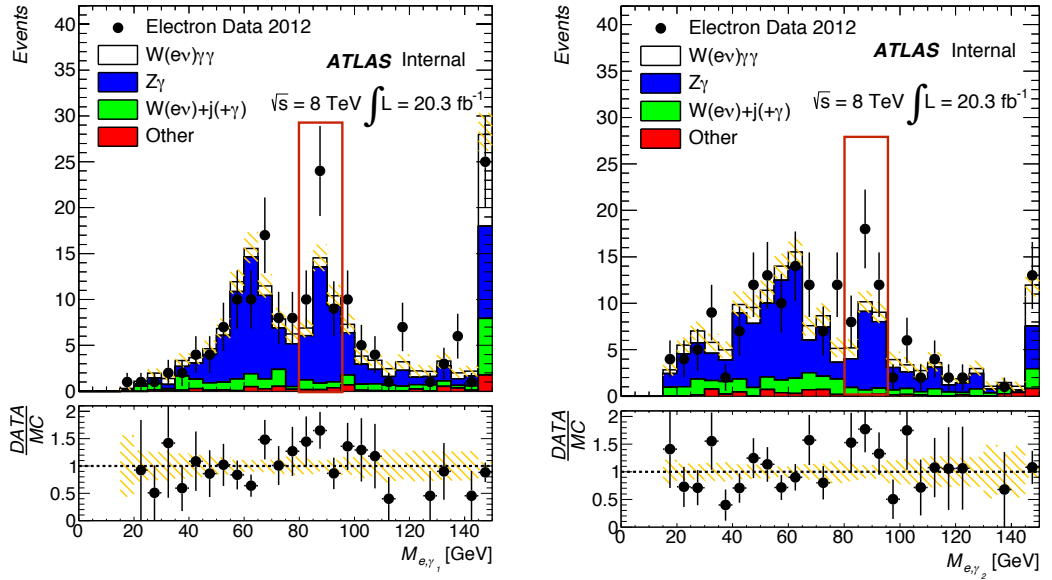
Kinematic distributions shown in Figure 5.1 were used to study how to reject this background. Figure 5.1(a) shows the two-body invariant mass of the selected electron with the selected leading and sub-leading photons. Figure 5.1(b) left plot shows the three-body invariant mass of the electron and two photons. As can be seen from these plots, the $Z(ee)\gamma$ background can be suppressed by imposing additional cuts on these variables. Generally speaking, if the photon in the $Z(ee)\gamma$ event comes from ISR, one of the $e\gamma$ invariant masses will be situated at the Z boson mass while events with FSR photon will have a $e\gamma\gamma$ mass centered at the Z mass. Choices of cuts on these variables were optimized to reject most of the $Z(ee)\gamma$ events. Another discriminating variable is the vector sum of transverse momenta of the electron and two photons system (p_T^{tot}) as shown in the right plot in Figure 5.1(b). This variable shows whether the fully reconstructed event is balanced in the transverse plane. For

$W\gamma\gamma$ events, a higher p_T^{tot} is expected because of the high energy neutrino from W boson decay while for $Z(ee)\gamma$ events the system is well balanced, resulting in a lower value of p_T^{tot} .

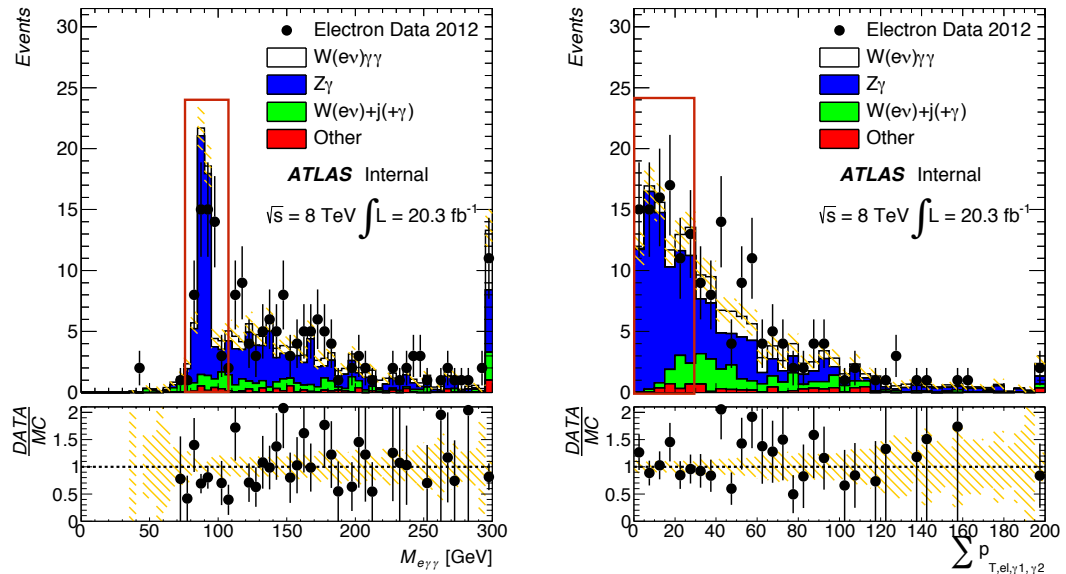
Cuts on these discriminating variables have been optimized in order to obtain the maximum background rejection with minimum signal loss. The quantity of $S/\sqrt{S+B}$ is used, where S and B represent the expected signal and background counts. $S/\sqrt{S+B}$ and the signal yield versus the cut on p_T^{tot} using simulated samples are shown at Figure 5.2. The cut is chosen to be $p_T^{tot} > 30$ GeV.

To summarize, the kinematic cuts chosen to reject $Z(ee)\gamma$ events are:

- $M(e, \gamma, \gamma) - M(Z) > 5$ GeV and $M(e, \gamma, \gamma) - M(Z) < -10$ GeV;
- $M(e, \text{leading } \gamma) - M(Z) > 3$ GeV and $M(e, \text{leading } \gamma) - M(Z) < -10$ GeV;
- $M(e, \text{sub-leading } \gamma) - M(Z) > 3$ GeV and $M(e, \text{sub-leading } \gamma) - M(Z) < -5$ GeV;
- $p_T(e\gamma\gamma) > 30$ GeV.

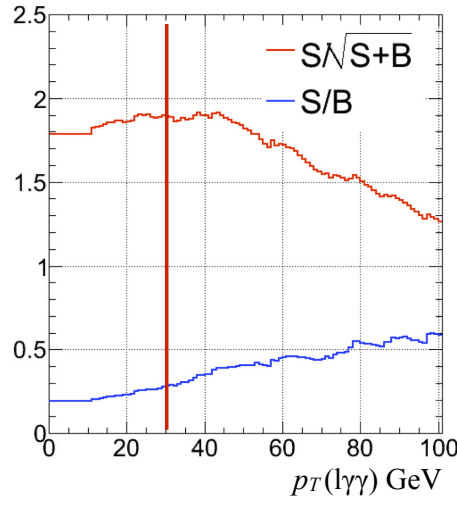


(a)

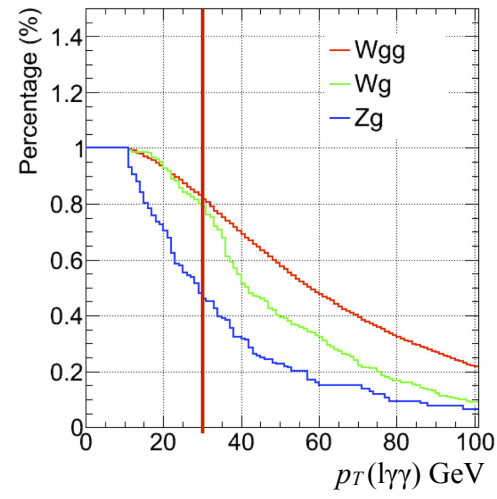


(b)

FIGURE 5.1: Invariant mass of electron and leading photon (top left), electron and sub-leading photon (top right), electron and two photons (bottom left), and total vector sum of transverse momentum of electron and two photons (bottom right). Events shaded in the box are rejected.



$S / \sqrt{S + B}$



Signal yield and background suppression

FIGURE 5.2: Optimization of the total vector sum of the transverse momentum of electron and two photons. The chosen lower cut is at 30 GeV. The right plot shows the percentage of events which survived the p_T^{tot} cut.

5.3 $W\gamma\gamma$ Signal Extraction

5.3.1 Candidate events

With the requirements described in the previous section applied, 47(15) $pp \rightarrow W(e\nu)\gamma\gamma$ candidates were found with the inclusive (exclusive) selection. Exclusive events are defined to be those with no central ($|\eta| < 4.4$) jets with $E_T > 30$ GeV. An event display of one of the selected candidates is shown in Figure 5.3.1.

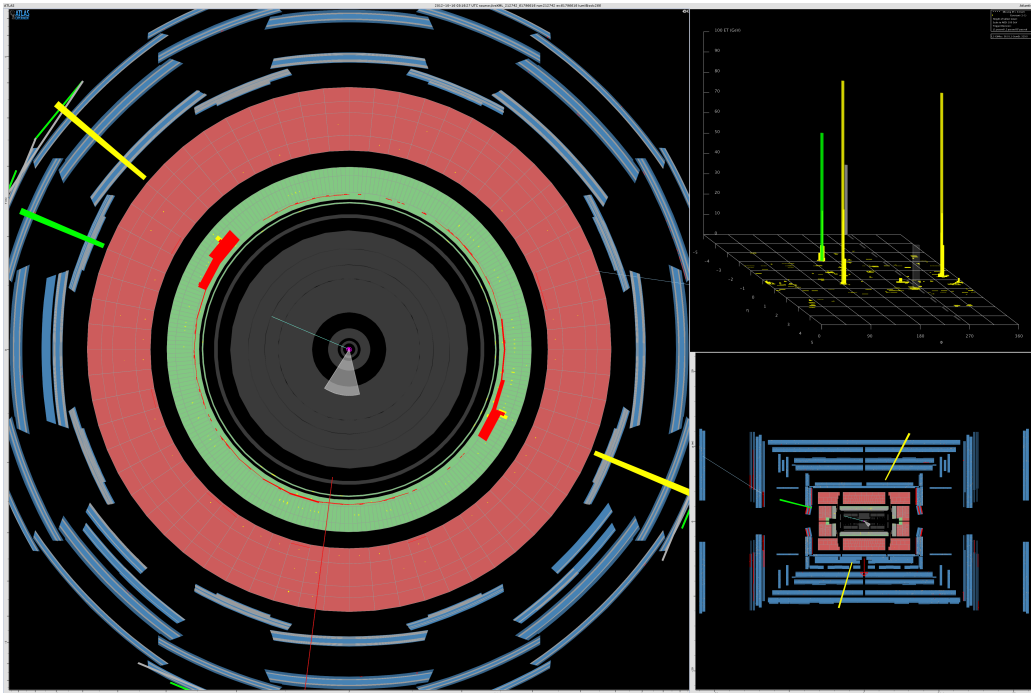


FIGURE 5.3: An event display of selected $W(e\nu)\gamma\gamma$ candidate. Photons are yellow, electrons are green and their electromagnetic showers are in red in the plot. Missing transverse energy is shown as red line. The left plot is a x - y plane cross section view, the upright plot is a log plot in η - ϕ space with the p_T shown in z coordinate. The lower right is a plot of the cross section view across the center of the detector, parallel to the beam line (η - z plane).

In these selected events, there is still contamination from other physics processes faking the signal signature with misidentified objects. The major backgrounds are from $pp \rightarrow W(e\nu)\gamma$ events with an additional hadronic jet faking one of the photons. Backgrounds with fake photon(s) are estimated using a data driven technique. This provides a correct normalization for processes with QCD jets as they generally have a sizable NLO contribution, and NLO Monte Carlo samples for these processes are not available at this time. Another reason is that hadronic jets are not perfectly modeled by ATLAS detector simulation. The baseline method performs a fit to the isolation distributions of selected photons (2D template fit method).

Contamination also come from events containing two real isolated photons and a misidentified electron. This component also must be estimated from data due to poor modeling of hadronic jets in the detector simulation. A two dimensional side-band (ABCD) method is employed to estimate this background.

5.3.2 Data-driven background estimation for fake photons and fake electrons

Evaluation of Jets faking photons

The 2D template method estimates the signal and background yields by applying an unbinned extended maximum likelihood fit simultaneously to the transverse isolation energy ($E_T^{\text{iso}1}, E_T^{\text{iso}2}$) distributions of the two photon candidates. The method and results will be described. The statistical and systematic uncertainties will also be discussed.

• Introduction to the 2D template fit method

The method uses events passing the event selection introduced above excluding the isolation requirement of the two photon candidates. These events can be divided into four different categories: events with two real photons are denoted as $\gamma\gamma$, while events with one photon candidate stemming from a jet are called γj ($j\gamma$) when

the leading (subleading) photon is real. The last category has events with both photons coming from jets and are called jj . With this categorization, the two-dimensional (E_T^{iso1} , E_T^{iso2}) distribution can be expressed by the sum of four isolation templates (F) normalized with their respective yields (W):

$$W_{tot}F_{tot}(E_T^{iso1}, E_T^{iso2}) = W_{\gamma\gamma}F_{\gamma\gamma}(E_T^{iso1}, E_T^{iso2}) + W_{\gamma j}F_{\gamma j}(E_T^{iso1}, E_T^{iso2}) \\ + W_{j\gamma}F_{j\gamma}(E_T^{iso1}, E_T^{iso2}) + W_{jj}F_{jj}(E_T^{iso1}, E_T^{iso2}). \quad (5.2)$$

If properly normalized, the templates can be considered as a two-dimensional probability density functions (PDF) of the transverse isolation energies.

Studies show that the transverse isolation energies of the two photon candidates are uncorrelated for events in the $\gamma\gamma$, γj and $j\gamma$ categories [38]. This allows us to write the corresponding PDFs as the product of two one-dimensional PDFs. For events in the jj category it was found that the correlation is not negligible. Thus the corresponding PDF cannot be factorized into products of 1D distributions and has to be modeled as a two-dimensional distribution with correlations. Therefore, Equation 5.2 can be re-written as:

$$W_{tot}F_{tot} = W_{\gamma\gamma}F_{\gamma,1}(E_T^{iso1})F_{\gamma,2}(E_T^{iso2}) + W_{\gamma j}F_{\gamma,1}(E_T^{iso1})F_{j,2}(E_T^{iso2}) \\ + W_{j\gamma}F_{j,1}(E_T^{iso1})F_{\gamma,2}(E_T^{iso2}) + W_{jj}F_{jj}(E_T^{iso1}, E_T^{iso2}), \quad (5.3)$$

where $F_{\gamma,1}(E_T^{iso1})$ and $F_{\gamma,2}(E_T^{iso2})$ are the one-dimensional real photon isolation PDFs for the leading and subleading photons, $F_{j,1}(E_T^{iso1})$ and $F_{j,2}(E_T^{iso2})$ are the one-dimensional isolation PDFs for a jet faking the leading or the subleading photon respectively, and $F_{jj}(E_T^{iso1}, E_T^{iso2})$ is the two-dimensional jj isolation PDF when both candidates are fake.

The signal ($W_{\gamma\gamma}$) and background ($W_{\gamma j}$, $W_{j\gamma}$, W_{jj}) yields can be obtained by fitting eq. 5.3 to data, i.e. by maximizing the extended likelihood function defined

as:

$$\mathcal{L}(\vec{\theta}|\vec{x}_1, \vec{x}_2, \dots) = P_{W_{tot}}(N) * \prod_{i=0}^N F_{tot}(\vec{x}_i|\vec{\theta}), \quad (5.4)$$

with $\vec{\theta} = (W_{\gamma\gamma}, W_{\gamma j}, W_{j\gamma}, W_{jj})$ given the data $\vec{x}_i = (E_T^{iso1}, E_T^{iso2})$. Here, $P_{W_{tot}}(N)$ is the poisson probability of observing N events when W_{tot} events were expected.

Once the fit is performed, by multiplying the obtained yields and the integral of the different PDFs in the region where both photons are isolated, one can extract the number of events in each category for events in the signal region.

• Application of the 2D template fit method and Results

The photon isolation PDFs $F_{\gamma,1}(E_T^{iso1})$ and $F_{\gamma,2}(E_T^{iso2})$ are determined by using $W\gamma\gamma$ Monte Carlo events with full detector simulation. These distributions (black markers) are fitted to a Crystal-Ball line-shape [39] as shown in Figure 5.4. The events are required to pass all the analysis selection criteria except the photon E_T^{iso} requirement.

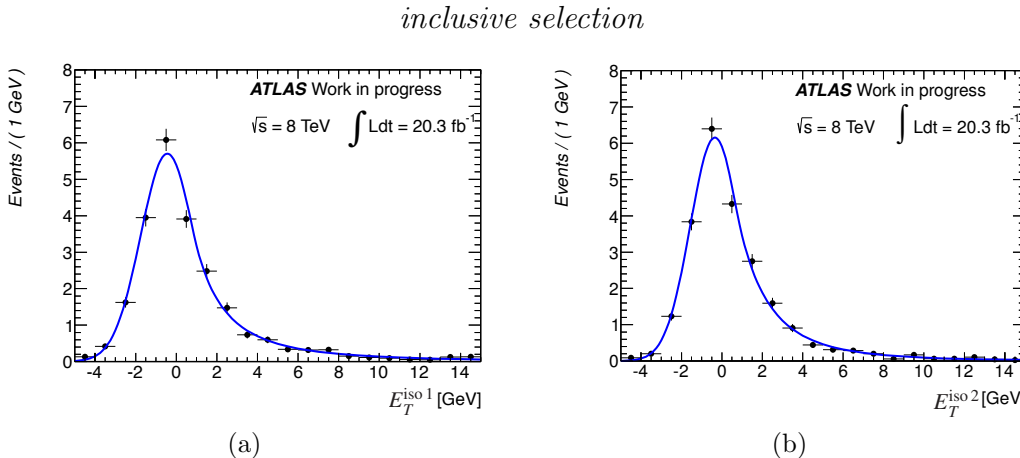


FIGURE 5.4: The E_T^{iso} distribution for the leading (left) and subleading (right) photon from simulated $W\gamma\gamma$ events using the inclusive selection are shown as black dots. The fitted photon isolation PDFs $F_{\gamma,1}(E_T^{iso1})$ and $F_{\gamma,2}(E_T^{iso2})$ are shown as solid lines.

The jet isolation PDFs $F_{j,1}(E_T^{iso1})$ and $F_{j,2}(E_T^{iso2})$ are determined from data in regions enriched with events with a jet faking a photon (control regions). In control regions, a non-tight (\tilde{T}) photon is required as introduced in Section 5.2.2. The $F_{j,1}(E_T^{iso1})$ and $F_{j,2}(E_T^{iso2})$ distributions are fitted to a Novosibirsk function [39]. The E_T^{iso} distributions and the corresponding isolation PDF's determined from the fit to the data are shown in Figure 5.5.

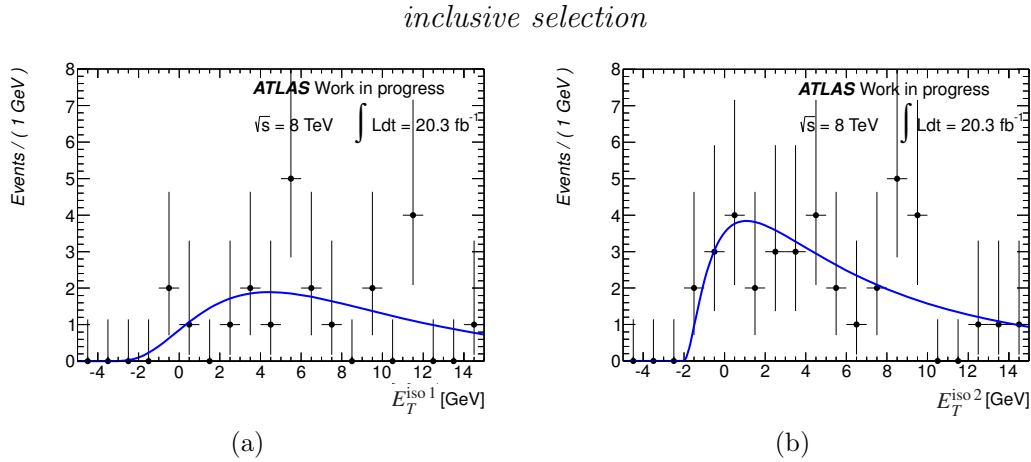


FIGURE 5.5: The jet E_T^{iso} distribution for the leading (left) and subleading (right) photon candidate from the data using the inclusive selection are shown as black dots. The fitted PDFs $F_{j,1}$ and $F_{j,2}$ are shown as solid lines.

The two-dimensional jj PDF is derived from data using the $\tilde{T}\tilde{T}$ sample, i.e. both photon candidates are required to be non-tight. This control region contains 9 events. Given the limited statistics available, the two-dimensional E_T^{iso} distribution is smoothed using an adaptive kernel estimate technique implemented in the RooFit framework [40]. The two-dimensional $F_{jj}(E_T^{iso1}, E_T^{iso2})$ distribution and the resulting smoothed PDF are shown in Figure 5.6. Effects of small leakage of signal events into the control regions are estimated by Monte Carlo simulations. More details can be found in Appendix A.

The results of the final fit to the parameters $(W_{\gamma\gamma}, W_{\gamma j}, W_{j\gamma}, W_{jj})$ are shown in

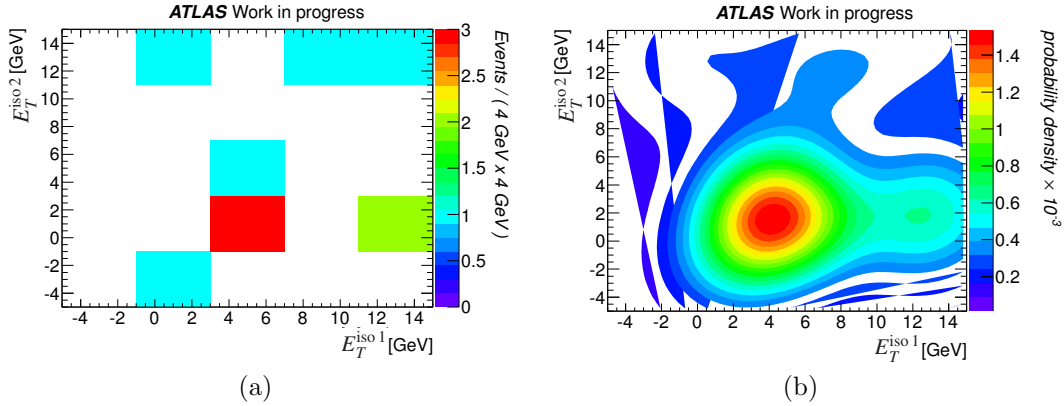


FIGURE 5.6: The two-dimensional E_T^{iso} distribution for the jj -PDF determined using the inclusive event selection. Left: $(E_T^{\text{iso}1}, E_T^{\text{iso}2})$ distribution in the $\tilde{\text{t}}\tilde{\text{t}}$ sample. Right: Corresponding smoothed PDF F_{jj} .

the first column of Table 5.1. The event yields integrated in the signal region with isolation cuts imposed on the selected photons are also provided in Table 5.1. Projections of the fitted two-dimensional function onto the transverse isolation energies of the two photon candidates are show in Figure 5.7.

Table 5.1: Results of the 2D template fit method using the inclusive event selection. For each category the result of the fit and the event yield is given. The yield column is the fitted normalizations for each component and the yield in signal region is the integrals in the isolated photon regions. The uncertainties are statistical only.

W($e\nu$) $\gamma\gamma$ inclusive channel		
category	yield	yield in signal region
$\gamma\gamma$	41 ± 10	34 ± 8
γj	20 ± 8	8 ± 3
$j\gamma$	21 ± 8	6 ± 2
jj	5 ± 9	1 ± 2

• Statistical and Systematic uncertainties

The statistical uncertainties on the fit parameters are calculated using **MINOS**⁶. It estimates the uncertainties for parameter x by finding the points in the parameter

⁶ MINOS is part of the MINUIT software package [41]

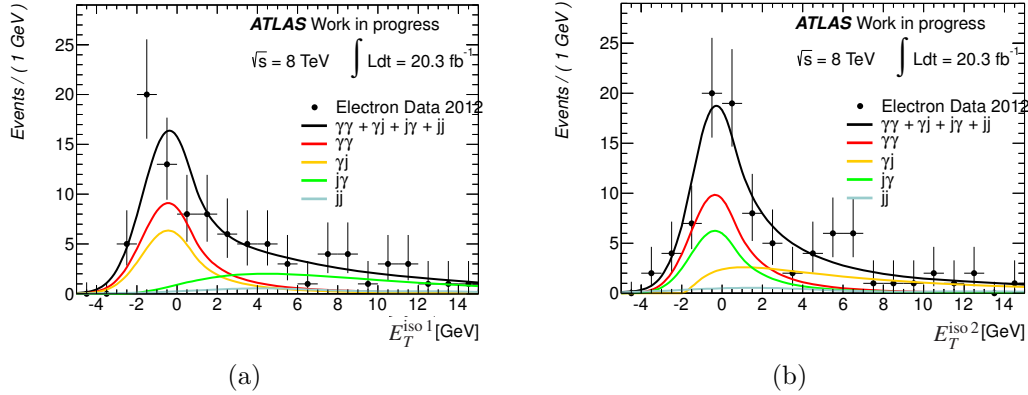


FIGURE 5.7: Projection of the two-dimensional isolation distributions onto the transverse isolation energy of the leading (left) and subleading (right) photon candidates. The black line shows the result of the final fit and the colored lines show the different components.

space at which the likelihood changes by 0.5. In each iteration the parameter x is kept fixed and all the other parameters are minimized before the likelihood is evaluated. The results from MINOS are validated with pseudo-experiments using a procedure described in detail in the Appendix A.

The resulting statistical uncertainties are summarized in Table 5.1. In the inclusive case, the relative uncertainties on fitted yield of the $\gamma\gamma$ category is 25%. The maximum corrections obtained by pseudo-experiments to the statistical uncertainties given by MINOS is applied in the jj -category and is below 10%.

Table 5.2: Expected number of background events in the electron channel with one real and one fake photon, two fake photons, and for the total fake photons background. $\gamma - jet$ category contains events with $p_T^\gamma > p_T^{jet}$, while it is the opposite for $jet - \gamma$.

	Inclusive channel	Exclusive channel
γ -jet	8 ± 3 (stat.) ± 3 (syst.)	4 ± 2 (stat.) ± 2 (syst.)
jet- γ	6 ± 3 (stat.) ± 4 (syst.)	2 ± 1 (stat.) ± 1 (syst.)
jet-jet	1 ± 2 (stat.) ± 1 (syst.)	0.3 ± 0.7 (stat.) ± 0.3 (syst.)
total fake γ	15 ± 5 (stat.) ± 5 (syst.)	6 ± 2 (stat.) ± 2 (syst.)

The systematic uncertainties in Table 5.2 arise from the modeling of the fake-photon templates, and in particular from the following effects:

- limited statistics in the control regions (events with anti-tight photons);
- functional form used for modeling the background distribution;
- definition of the control regions;
- dependence on Monte Carlo generator;
- statistical uncertainty on signal leakage.

The effect of each source of systematic uncertainty is also evaluated using pseudo-experiments, as described in Appendix A. Limited statistics in the control region results in the largest component in the systematic uncertainties.

In the electron channel exclusive case shown in Table 5.2, the limited statistics in the control regions does not allow using the 2D template fit method. In that case, the number of overall fake photon events expected is extrapolated from the inclusive measurement according to the N_{jet} distribution taken from fake lepton dominated control regions (with the electron isolation cut reversed). In addition to the systematic uncertainties listed above, a systematic related to the N_{jet} variable shape used in the extrapolation is also taken into account.

Evaluation of jet faking electrons

A 2d-sideband, also named an ABCD method, uses a two dimensional phase space to define three regions with enriched background events. Two minimally correlated sets of variables are chosen, thus the number of expected background events in signal region A can be calculated using a simple relation: $N_A = \frac{N_B * N_C}{N_D}$. The definition of the ABCD regions is shown in Figure 5.8, with detailed description in the Caption. The assumption of no correlation between the two sets of variables can be made because the majority of the background events are initiated by light flavor hadronic jets instead of a beauty hadron decay, in which case the electron is isolated, and the missing transverse energy comes from non-perfect reconstruction under high pile-up conditions. Small corrections due to the leakage of signal events into control regions and contributions from other backgrounds are estimated by simulated events and subtracted from the yields.

Tests of the correlation between two variables used in the ABCD definitions, detailed calculation with signal leakage considered and the treatment of systematic uncertainties are documented in Appendix A.

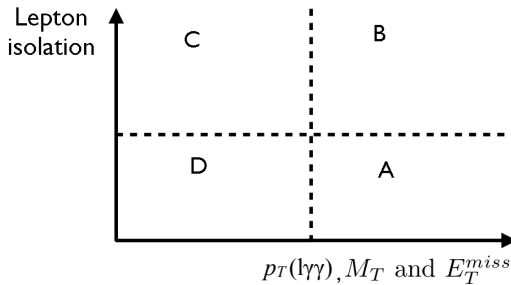


FIGURE 5.8: A sketch presentation of the signal region (A) and three control regions (B, C and D) used the ABCD method. Region A contains events with an isolated electron and high E_T^{miss} , region B has the requirement on electron isolation reversed, region C has the requirement on variables related to E_T^{miss} reversed, while region D has both requirements reversed.

The background due to a jet misidentified as an electron is found to be small,

accounting for 1.5 ± 0.6 (stat.) ± 1.0 (syst.) events in the inclusive event selection and 0.2 ± 0.2 (stat.) ± 0.2 (syst.) in the exclusive event selection. The systematic errors are estimated by varying control region definitions.

$Z(ee)\gamma + \text{jets and electron-photon misidentification}$

The production of a Z boson which subsequently decays to electrons, in association with a photon and a jet, may pass the event selection if one of the electrons is not reconstructed and the jet is misidentified as the second photon. These background events can also pass the selection if one of the leptons is misidentified as a photon. The first scenario is covered by the fake photon background estimate described above, since one of the photons is coming from a jet. The second scenario is suppressed by additional cuts introduced in event selection and is estimated from simulated sample of $Z(ee)\gamma$. The reason is that the electromagnetic response of the detector is well modeled by Monte Carlo samples passing the full detector simulation.

Other backgrounds

Other backgrounds arise from events containing a real charged lepton and two real photons or multiple leptons and photons with lepton-photon misidentification. These include diboson (WW, WZ) and top quark pair production. $W(\rightarrow \tau\nu)\gamma\gamma$ events can also fake the signal with the tau lepton decaying to electron and neutrino. These backgrounds are negligible and are taken from predictions given by Monte Carlo events passing full detector simulation because even if 100% uncertainties are assigned on these backgrounds, the effects on the signal yield are very small.

5.4 Summary of the measured $pp \rightarrow W(e\nu)\gamma\gamma + X$ signal

The number of selected $W(e\nu)\gamma\gamma$ events and all the backgrounds are summarized in the left columns of Tables 5.3 and 5.4 for the inclusive and exclusive selections. As

shown in the table, the dominate background is from jets misidentified as photons. The dominate systematic uncertainty on the total background is associated with this source. The second largest background is $Z\gamma(\gamma)$ with one of the electrons misidentified as a photon. This background is difficult to be further reduced due to the much larger production rate of the $Z\gamma$ process. The other backgrounds are shown to be negligible.

Measurements of the $pp \rightarrow W(\mu\nu)\gamma\gamma$ production are also shown in Tables 5.3 and 5.4. This analysis is performed by collaborators in the $pp \rightarrow W\gamma\gamma$ analysis team. No requirement is imposed on $M(l\gamma)$, $M(l\gamma\gamma)$ or $p_T(l\gamma\gamma)$ because the rate of muon being misidentified as a photon is much lower than in the electron channel. The same data driven techniques were employed for measuring jet faking photon and jet faking muon backgrounds. More events were observed in the muon channel due to loosened cuts and higher detection efficiency of muons with the ATLAS detector.

Table 5.3: Number of candidate events in data passing the full selection of Section 5.2 in the electron and muon channels for the inclusive case. The number of background events from misidentified photons and leptons, as estimated from data, and from MC derived backgrounds are also shown. The subtraction of these backgrounds yields the measured signal in each channel, with statistical and systematic uncertainties.

	Electron channel	Muon channel
data	49 ± 7	112 ± 11
Fake photon background	19 ± 5 (stat.) ± 8 (syst.)	33 ± 8 (stat.) ± 9 (syst.)
Fake lepton background	1.4 ± 0.6 (stat.) ± 0.8 (syst.)	10.4 ± 3.7 (stat.) ± 4.3 (syst.)
$Z\gamma(\gamma)$	11.4 ± 1.4 (stat.)	4.1 ± 0.2 (stat.)
$W(\rightarrow \tau\nu)\gamma\gamma$	0.5 ± 0.1 (stat.)	1.0 ± 0.1 (stat.)
$t\bar{t}$	1.2 ± 0.5 (stat.)	3.7 ± 2.0 (stat.)
W^+W^-	0.3 ± 0.1 (stat.)	0.4 ± 0.3 (stat.)
WZ	0.2 ± 0.1 (stat.)	2.1 ± 0.5 (stat.)
ZZ	0.1 ± 0.1 (stat.)	0.1 ± 0.1 (stat.)
N_{bkg}	34.1 ± 5.6 (stat.) ± 8.1 (syst.)	55.4 ± 9.4 (stat.) ± 9.9 (syst.)
$N_{\text{sig}} = N_{\text{data}} - N_{\text{bkg}}$	14.9 ± 9.0 (stat.) ± 8.1 (syst.)	56.6 ± 14.2 (stat.) ± 9.9 (syst.)

Table 5.4: Number of candidate events in data passing the full selection of Section 5.2 in the electron and muon channels for the exclusive case. The number of background events from misidentified photons and leptons, as estimated from data, and from MC derived backgrounds are also shown. The subtraction of these backgrounds yields the measured signal in each channel, with statistical and systematic uncertainties.

	Electron channel	Muon channel
data	16 ± 4	54.0 ± 7.3
Fake photon background	7 ± 2 (stat.) ± 3 (syst.)	15 ± 6 (stat.) ± 6 (syst.)
Fake lepton background	0.2 ± 0.2 (stat.) ± 0.2 (syst.)	4.8 ± 4.5 (stat.) ± 2.0 (syst.)
$Z\gamma(\gamma)$	2.0 ± 0.5 (stat.)	2.9 ± 0.2 (stat.)
$W(\rightarrow \tau\nu)\gamma\gamma$	0.13 ± 0.04 (stat.)	0.4 ± 0.1 (stat.)
$t\bar{t}$	≤ 0.2	≤ 0.2
W^+W^-	0.1 ± 0.1 (stat.)	0.1 ± 0.1 (stat.)
WZ	0.1 ± 0.1 (stat.)	0.8 ± 0.3 (stat.)
ZZ	≤ 0.02	≤ 0.02
N_{bkg}	9.8 ± 2.6 (stat.) ± 3.0 (syst.)	23.5 ± 7.1 (stat.) ± 6.4 (syst.)
$N_{\text{sig}} = N_{\text{data}} - N_{\text{bkg}}$	6.2 ± 4.8 (stat.) ± 3.0 (syst.)	30.5 ± 10.2 (stat.) ± 6.4 (syst.)

Figures 5.9 to 5.14 show distributions of events with inclusive $W(e\nu)\gamma\gamma$ selection. Figures 5.9 to 5.11 are p_T , η and isolation energy distributions of the two photons and the electron. Distributions of $\Delta R(\gamma; \gamma)$ and $M(\gamma; \gamma)$ are shown in Figure 5.12. Missing transverse energy, traverse mass of W boson and number of jets distributions are shown in Figures 5.13 and 5.14. The black dots represent the data candidates after the full analysis selection has been applied, whereas the solid histograms give the expected events obtained with SM Monte Carlo samples or data-driven methods. The stacked histogram show the total expected events with the hashed areas showing the total uncertainty. The $t\bar{t}$, $W(\rightarrow \tau\nu)\gamma\gamma$ and diboson (WW, WZ) contributions are combined and labelled “Other”.

As shown in the plots, all kinematic distributions are well modeled by the Monte Carlo generated events. The SM $W(e\nu)\gamma\gamma$ signal is taken from SHERPA and a scale is applied so that the overall signal plus background expectation is normalized to the number of events observed in data. The scale between SM prediction of $W\gamma\gamma$ signal from Sherpa to data was found to be 0.96 (0.93) in the inclusive (exclusive) case. The interpretation of the measured signal yield for both electron and muon channels will be discussed in the next Chapter. Cross section calculation and constraints on anomalous quartic couplings will be presented. Comparison of the cross section measurements to the SM theoretical prediction will be discussed.

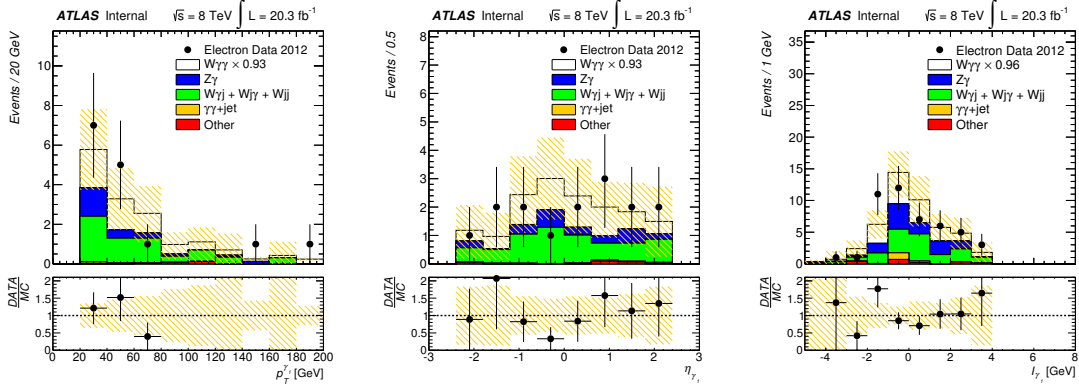


FIGURE 5.9: Leading photon E_T (left), η (middle), Isolation(right) distributions in the electron channel obtained with the inclusive selection. The $W\gamma j + Wj\gamma + Wjj$ -label denotes the fake photon background component and the fake lepton component is labelled “ $\gamma\gamma + \text{jet}$ ”. The $t\bar{t}$, $W(\rightarrow \tau\nu)\gamma\gamma$ and diboson (WW, WZ)contributions are combined and labelled as “Other”. The hashed areas show the total uncertainty on the background estimate.

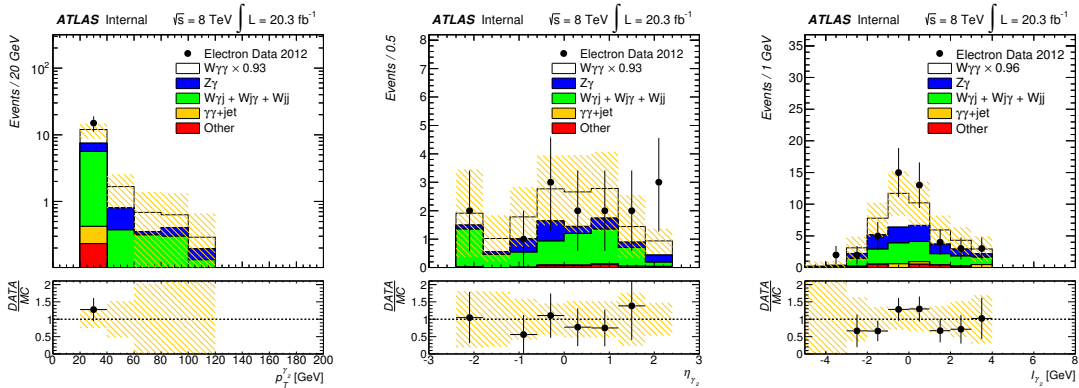


FIGURE 5.10: Subleading photon E_T (left), η (middle), Isolation(right) distributions in the electron channel obtained with the inclusive selection.

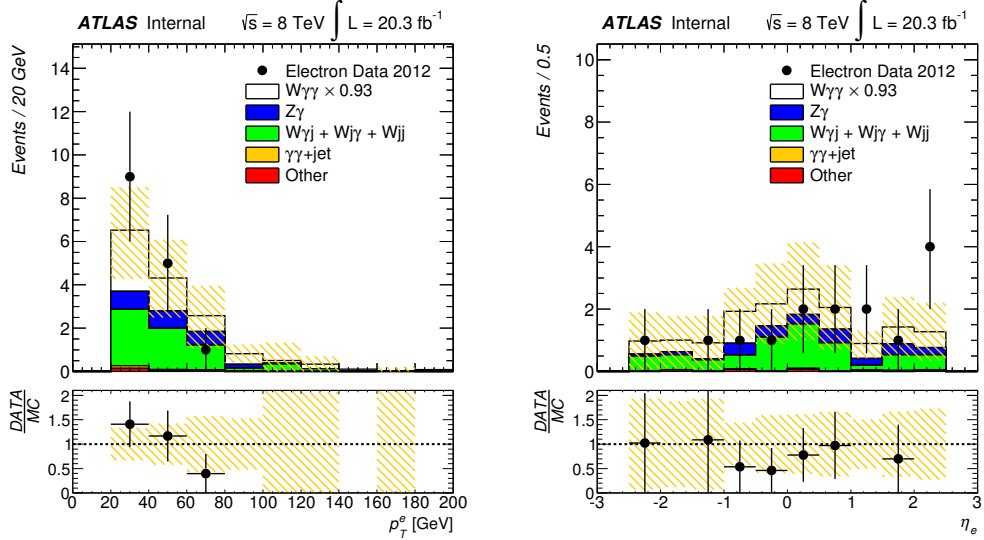


FIGURE 5.11: Leading electron p_T (left), η (right) distributions in the electron channel obtained by using the inclusive selection.

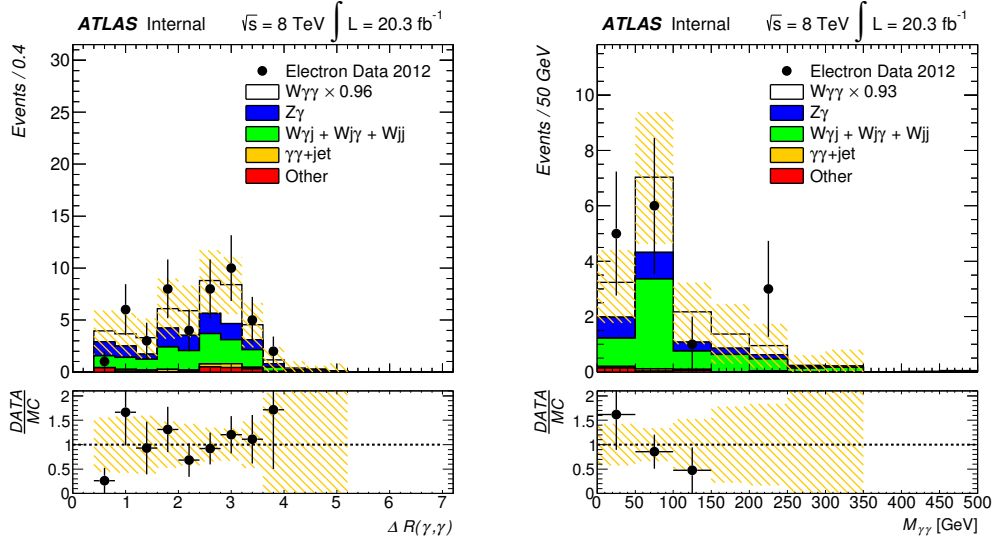


FIGURE 5.12: ΔR between leading and subleading p_T photons(left) and diphoton invariant mass distribution(right) in the electron channel.

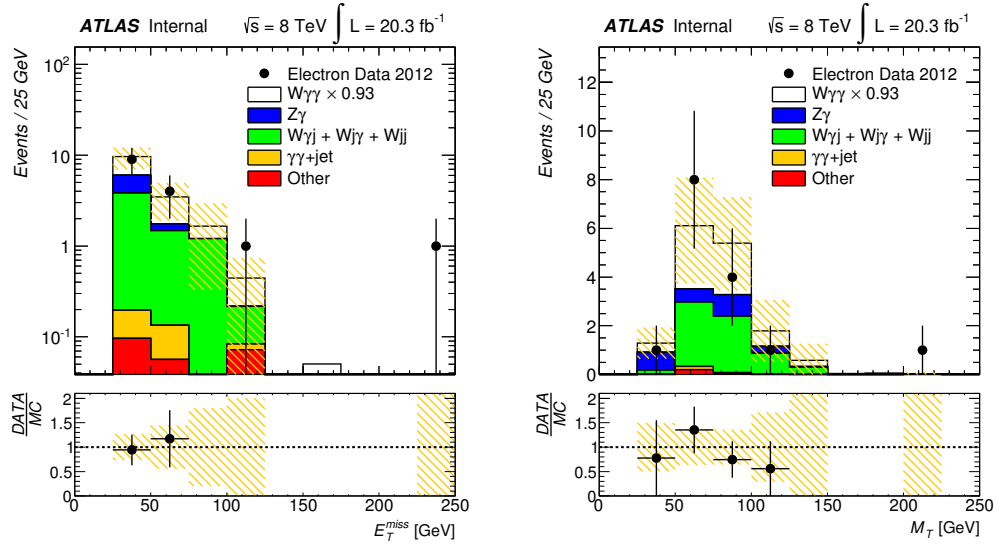


FIGURE 5.13: Missing transverse energy (left) and W transverse mass distribution (right) in the electron channel obtained by using the inclusive selection.

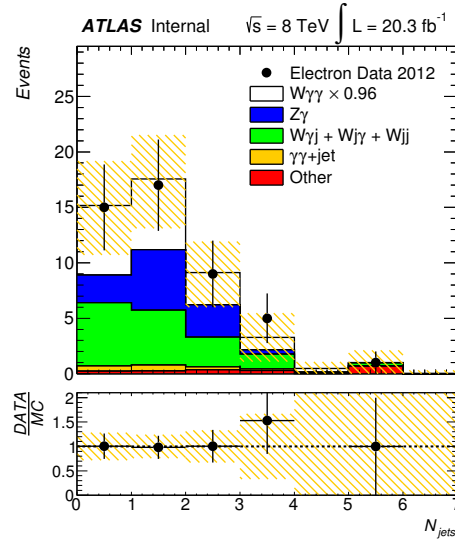


FIGURE 5.14: Number of jets distribution for the electron channel obtained by using the inclusive selection.

6

Interpretation of $\text{pp} \rightarrow W\gamma\gamma + X$ Measurement Results

This chapter describes the interpretation of the $W\gamma\gamma$ measurement results presented in Chapter 5. Cross sections are computed and compared to the next-to-leading order (NLO) SM theory predictions. Constraints on anomalous gauge boson couplings are also discussed at the end of this Chapter.

6.1 Cross section measurement

The extraction of the cross-section for $pp \rightarrow W\gamma\gamma + X$ process is presented in this section. The cross-section in a well-defined fiducial phase space is computed in the following way:

$$\sigma_{W\gamma\gamma}^{fid} = \frac{N_{l\nu\gamma\gamma}^{obs} - N_{l\nu\gamma\gamma}^{bkg}}{\int \mathcal{L} dt \times A_{W\gamma\gamma \rightarrow l\nu\gamma\gamma} \times C_{W\gamma\gamma \rightarrow l\nu\gamma\gamma}} \quad (6.1)$$

$N_{l\nu\gamma\gamma}^{obs}$ and $N_{l\nu\gamma\gamma}^{bkg}$ denote the number of selected candidates and expected background events. $\int \mathcal{L} dt$ is the integrated luminosity. $A_{W\gamma\gamma \rightarrow l\nu\gamma\gamma}$ is the acceptance factor which extrapolates the fiducial region used for the measurements to an extended fiducial region. $C_{W\gamma\gamma \rightarrow l\nu\gamma\gamma}$ is the factor which represents the detection efficiency in our experiment.

The fiducial phase space is defined in Section 6.1.1. The calculation of $A_{W\gamma\gamma \rightarrow l\nu\gamma\gamma}$ and $C_{W\gamma\gamma \rightarrow l\nu\gamma\gamma}$ will be presented in Section 6.1.2. A profile maximum-likelihood method used to calculate the fiducial cross section will be described in Section 6.1.3. Measurements are compared to SM theoretical predictions in Section 6.1.4.

6.1.1 Fiducial Region Definition

A fiducial phase space definition can be found in Table 6.1. It is common to $W(e\nu)\gamma\gamma$ and $W(\mu\nu)\gamma\gamma$ channels so that these two measurements can be combined. This requires a small extrapolation over the calorimeter crack region, which is excluded for reconstructed electrons and photons ($1.37 < |\eta| < 1.52$). For muons the range $|\eta| < 2.5$ is fully covered by the detector.

The fiducial region is defined at truth particle level¹ after the parton shower. An *anti* – k_t jet clustering algorithm with a cone size of $\Delta R = 0.4$ is used to define

¹ Events generated by the Monte Carlo generators are passed through parton shower (cascades of radiation produced from QCD processes and interactions) to model QCD jets, the resulting events are referred to be at 'truth level'.

jets. The requirement on the isolation fraction of the photons is defined as the ratio between the energy carried by the closest jet (with $\Delta R(\gamma, \text{jet}) < 0.4$) to the photon and the energy carried by the photon. The exclusive $W\gamma\gamma + X$ channel is defined by vetoing events containing jets passing the selection defined in Table 6.1.

Table 6.1: Definition of the fiducial region where the cross-section is evaluated. p_T^ν is the transverse momentum of the neutrino coming from the W decay. The jet veto is only applied in the exclusive selection.

Extended Fiducial Region	
Cuts	$pp \rightarrow \ell\nu\gamma\gamma$
Lepton	$p_T^\ell > 20 \text{ GeV}$ $p_T^\nu > 25 \text{ GeV}$ $ \eta^\ell < 2.5$
W-Boson	$m_T > 40 \text{ GeV}$
Photon	$E_T^\gamma > 20 \text{ GeV}$ $ \eta^\gamma < 2.37$
$\Delta R(\ell, \gamma) > 0.7$ $\Delta R(\gamma, \gamma) > 0.4$ iso. fraction $\epsilon_h^p < 0.5$	
Jets	$p_T^{\text{jet}} > 30 \text{ GeV}$ $ \eta^{\text{jet}} < 4.4$ $\Delta R(\ell, \text{jet}) > 0.3$ $\Delta R(\gamma, \text{jet}) > 0.3$ Exclusive selection: $N_{\text{jet}} = 0$

6.1.2 Acceptance and Efficiency

Computation of Acceptance and Efficiency

A correction factor, $\epsilon = A \times C$, is obtained from Monte Carlo simulation of $W\gamma\gamma + X$ events. The LO generator SHERPA is used to generate the baseline sample and ALPGEN is used as a cross-check. ϵ is defined as the ratio of the number of reconstructed events passing the analysis selection as defined in Section 5.2 to the number of events passing the requirements of the fiducial region (defined in Table 6.1)

at truth particle level:

$$\epsilon = \frac{N_{reco}}{N_{truth, fid}}. \quad (6.2)$$

The correction factor ϵ can be written as the product of A and C :

$$\epsilon = A \times C = \frac{N_{truth, restricted fid}}{N_{truth, fid}} \times \frac{N_{reco}}{N_{truth, restricted fid}}. \quad (6.3)$$

Here $N_{truth, restricted fid}$ represents the number of truth-level events falling inside the “restricted” fiducial volume, *i.e.* the measured phase space before any extrapolation is performed over the crack region in the calorimeter. The uncertainties on the detection of the particles in the final state contribute to the uncertainties on the efficiency C . In order to estimate this effect, the momentum or detection efficiency of a reconstructed object is varied by one sigma (up or down) and the corresponding event selection efficiency C_{sys} is calculated. A relative systematic error is defined as $\sigma_C = \frac{C_{sys} - C_{nom}}{C_{nom}}$. The total systematic error is obtained by adding the larger error out of the up and down-variations in quadrature. Details on this is documented in Appendix B.

Results of computed correction factors for the $W(e\nu)\gamma\gamma$ channel can be found in Table 6.2. The inclusive selection manifests a large difference (6.9%) between two Monte Carlo generators used (see Table 6.2 last entry in the left column). This is due to the fact that ALPGEN simulates 2 additional partons while SHERPA produces up to three. Therefore discrepancy in the inclusive channel is expected while the difference in the exclusive case with zero additional parton is negligible (1%). The uncertainties on the particle detection are also summarized in Table 6.2. Most of the uncertainties arise from corrections to fix the discrepancies between Monte Carlo simulated samples and data. The dominate systematic error sources, EM and jet energy scale to correct for the discrepancy in energy measurements between Monte Carlo simulated samples and data, are listed in Table 6.2 for up (first item) or

down(second item) one sigma variations. A complete list of systematic sources are documented in Appendix B.

Table 6.2: Correction factor for the inclusive and the exclusive selection along with their statistical and relative systematic uncertainty in the electron channel. The statistical uncertainty on the systematic component is also given for completeness.

	Inclusive Selection		Exclusive Selection	
Correction Factor ϵ	$(19.6 \pm 0.5 \text{ (stat.)} \pm 1.3 \text{ (sys.)}) \%$		$(15.1 \pm 0.7 \text{ (stat.)} \pm 1.3 \text{ (sys.)}) \%$	
Acceptance A	$(82.5 \pm 0.4 \text{ (stat.)}) \%$		$(82.5 \pm 0.6 \text{ (stat.)}) \%$	
Efficiency C	$(23.7 \pm 0.6 \text{ (stat.)}) \%$		$(18.4 \pm 0.8 \text{ (stat.)}) \%$	
EM Energy Scale	2.4 (up)	0.8 (down)	4.5 (up)	1.6 (down)
Jet Energy Scale	5.3 (up)	2.0 (down)	6.2 (up)	3.3 (down)
Relative deviation to ALPGEN of C [%]	6.9		1.0	

6.1.3 The Fiducial Cross-Section Measurement

A maximum log-likelihood approach is used to calculate the individual and combined $W(e\nu)\gamma\gamma$ and $W(\mu\nu)\gamma\gamma$ cross-sections. This method takes into account the Poisson statistics of the samples. And the propagation of the systematic uncertainties considers correlations between the two channels. The calculation and treatment of systematic uncertainties are discussed in this section.

Fiducial Cross-Section Calculation

The number of expected candidates can be written as

$$N_{exp}^i = N_s^i + N_b^i. \quad (6.4)$$

where N_b^i is the number of predicted background events, and N_s^i is the number of expected signal events.

The number of signal events can be written as a function of the fiducial cross-section defined in Equation 6.1:

$$N_s^i(\sigma_{W\gamma\gamma}^{fid}) = \sigma_{W\gamma\gamma}^{fid} \times A_{W\gamma\gamma \rightarrow l\nu\gamma\gamma}^i \times C_{W\gamma\gamma \rightarrow l\nu\gamma\gamma}^i \times \int \mathcal{L} dt, \quad (6.5)$$

where $A_{W\gamma\gamma \rightarrow l\nu\gamma\gamma}^i$ and $C_{W\gamma\gamma \rightarrow l\nu\gamma\gamma}^i$ are the acceptance and efficiency factors computed in the last section. $\int \mathcal{L} dt$ is the integrated luminosity. Index i iterates over electron and muon channels for the combined cross section.

In order to take into account the impact of systematic uncertainties, the number of predicted signal and background events are written as:

$$N_s^i(\sigma_{W\gamma\gamma}^{fid}, \{x_k\}) = \sigma_{W\gamma\gamma}^{fid} \times A_{W\gamma\gamma \rightarrow l\nu\gamma\gamma}^i \times C_{W\gamma\gamma \rightarrow l\nu\gamma\gamma}^i \times \int \mathcal{L} dt \times (1 + \sum_{k=1}^n x_k S_k^i) \quad (6.6)$$

$$N_b^i(\{x_k\}) = N_b^i(1 + \sum_{k=1}^n x_k B_k^i). \quad (6.7)$$

In equations 6.6 and 6.7, S_k^i and B_k^i are the standard deviation of the k^{th} systematic uncertainty in channel i . Each systematic uncertainty is assumed to have a normal distribution with zero mean and unit variance, $D(x_k) \sim e^{-x_k^2/2}$.

A negative log-likelihood function is constructed as (from now on $\sigma \equiv \sigma_{W\gamma\gamma}^{fid}$):

$$-\ln L(\sigma, \{x_k\}) = \sum_{i=1}^2 -\ln \left(\frac{e^{-(N_s^i(\sigma, \{x_k\}) + N_b^i(\{x_k\}))} \times (N_s^i(\sigma, \{x_k\}) + N_b^i(\{x_k\}))^{N_{obs}^i}}{(N_{obs}^i)!} \right) + \sum_{k=1}^n \frac{x_k^2}{2}. \quad (6.8)$$

The part inside the natural logarithm is a Poisson function which describes the probability of observing N_{obs}^i events in channel i given the expected number of signal and background events $(N_s^i(\sigma, \{x_k\}) + N_b^i(\{x_k\}))$. The second term takes care of the gaussian constraints on the nuisance parameters x_k . Each systematic k is ascribed to an independent source. The linear sum of two systematic sources is put in as one x_k if they are correlated.² A single random variable x_k is used over all channels in signal and background as the effect of each systematic is 100% correlated across electron and muon channels, and between signal and background components.

² Considering the case of uncertainties on electron energy scale (x_1) and photon energy scale (x_2), they are correlated since both are derived from measurements based on EM calorimeter. In this case, $(x_1 + x_2)^2$ generates the correlation term $x_1 \times x_2$

To find the most probable value of σ , the log-likelihood function is minimized by letting σ and all the nuisance parameters x_k float in the fit. The fit provides a total uncertainty that includes both statistical and systematic components. By subtracting the systematic component in quadrature from the total uncertainty, one obtains the statistical uncertainty component. The minimization and error calculation is performed by using the Minuit package [41].

Estimation of Systematic Uncertainties on the Fiducial Cross-Section

In order to estimate the systematic uncertainties on the measurement, a series of minimizations of the log-likelihood is performed. In each of these minimizations, all the nuisance parameters are free to float except the $k - th$ parameter being fixed at up or down one sigma variation. The difference between the resulting cross-section and the nominal value is taken as the systematic uncertainty due to the $k - th$ source.

Measurement Results

The maximum log-likelihood method is applied in $W(e\nu)\gamma\gamma$ and $W(\mu\nu)\gamma\gamma$ individually and combined. The results for both inclusive and exclusive categories are summarized in Table 6.3. The statistical and systematic uncertainties are obtained with the procedure described above. All systematic uncertainties except the one associated with luminosity are added in quadrature and is shown as the systematic uncertainty in the table. The asymmetry in the uncertainties comes from the positive and negative variations in the calculation of systematic uncertainties. The significance of the measurements can be estimated by dividing the central value with the total uncertainty. A simple calculation gives 3.5σ (2.3σ) for the inclusive(exclusive) measurement. These significance numbers agree with those obtained with pseudo-experiments.

Table 6.3: Fiducial cross-section measurements of the $pp \rightarrow l\nu\gamma\gamma$ process for two isolated photons with $p_T > 20$ GeV.

	σ^{fid} [fb] ($N_{jet} \geq 0$)
$pp \rightarrow \mu\nu\gamma\gamma$	$7.1 + 1.3 -1.2$ (Stat.) $+ 1.6 - 1.5$ (Syst.) ± 0.2 (Lumi.)
$pp \rightarrow e\nu\gamma\gamma$	$4.3 + 1.8 -1.6$ (Stat.) $+ 1.9 - 1.8$ (Syst.) ± 0.2 (Lumi.)
$pp \rightarrow \ell\nu\gamma\gamma$	$6.3 + 1.1 -1.0$ (Stat.) $+ 1.5 - 1.4$ (Syst.) ± 0.2 (Lumi.)
	σ^{fid} [fb] ($N_{jet} = 0$)
$pp \rightarrow \mu\nu\gamma\gamma$	3.5 ± 0.9 (Stat.) $+ 1.2 - 1.1$ (Syst.) ± 0.1 (Lumi.)
$pp \rightarrow e\nu\gamma\gamma$	$1.9 + 1.4 -1.1$ (Stat.) ± 1.2 (Syst.) ± 0.1 (Lumi.)
$pp \rightarrow \ell\nu\gamma\gamma$	$2.9 + 0.8 -0.7$ (Stat.) $+ 1.1 - 1.0$ (Syst.) ± 0.1 (Lumi.)

6.1.4 Comparison to the SM theory prediction

Next-to-leading order (NLO) parton-level predictions

The NLO SM predictions for $pp \rightarrow W^\pm \gamma\gamma + X$ production are obtained using the events generated by MCFM [25]. The sources of photons include initial state radiation (ISR) from the colliding quarks, final state radiation (FSR) from the charged lepton in the $W \rightarrow l\nu$ decay, and the photons directly radiated from the W boson's triple and quartic gauge couplings. The advantage of using MCFM for the NLO SM predictions is that contributions of photons from quark/qluon fragmentation are included as part of the ISR.

To compare the SM predictions to the measurements of $pp \rightarrow W\gamma\gamma + X$, MCFM parton-level events were generated using the particle-level phase space chosen for extended fiducial cross section measurements as shown in Table 6.1. In order to make a comparison of these SM cross section predictions to the measured cross sections, the difference between jets defined at parton level and jets defined with jet clustering algorithm after parton shower needs to be corrected. The effect of the different jet definitions can be estimated by calculating parton to particle level correction factors $C^{*parton \rightarrow particle}$ using Monte Carlo samples.

ALPGEN+HERWIG and SHERPA $pp \rightarrow W\gamma\gamma + X$ LO event generators were used to estimate parton to particle level corrections. These events have both truth-level partons and hadrons that can be used to form $anti-k_t$ -clustered jets. SHERPA is used as the baseline.

The parton to particle level correction factor $C^{*parton \rightarrow particle}$ can be factorized according to

$$C^{*parton \rightarrow particle} = T_{N_{jet}} * T_{\gamma_{iso}}. \quad (6.9)$$

$T_{N_{jet}}$ and $T_{\gamma_{iso}}$ reflect the impact of the object definitions at parton level in comparison to the particle level on the number of jets and the photon isolation fraction ϵ_h

respectively. They are defined as following:

$$T_{N_{\text{jet}}} = \frac{N(\text{jet}_{\text{parton}}, \gamma_{\text{iso} - \text{particle}})}{N(\text{jet}_{\text{particle}}, \gamma_{\text{iso} - \text{particle}})}, \quad (6.10)$$

$$T_{\gamma_{\text{iso}}} = \frac{N(\text{jet}_{\text{parton}}, \gamma_{\text{iso} - \text{parton}})}{N(\text{jet}_{\text{parton}}, \gamma_{\text{iso} - \text{particle}})}. \quad (6.11)$$

Here $N(\text{jet}_i, \gamma_{\text{iso} - j})$ stands for the number of events in the fiducial region, where the jets and photon isolation are defined as indicated by the indices i, j ; i.e. at parton or particle level. The values of $C^{*\text{parton} \rightarrow \text{particle}}$ obtained for the different signal regions can be found in Table 6.4. The systematic error is dominated by the parton showering modeling and the matching between matrix element calculations and parton showering. It is evaluated by comparing the value of $C^{*\text{parton} \rightarrow \text{particle}}$ obtained from SHERPA Monte Carlo to the one computed using ALPGEN+HERWIG, as the event generators employ different parton shower modelling. The systematic uncertainty is then taken as the difference between the values of $C^{*\text{parton} \rightarrow \text{particle}}$ from the two different generators.

Using this scale factor, the parton level SM cross-sections predictions (σ^{parton}) can be corrected to particle level (σ^{particle}) according to:

$$\sigma^{\text{particle}} = \frac{\sigma^{\text{parton}}}{C^{*\text{parton} \rightarrow \text{particle}}}. \quad (6.12)$$

Table 6.4: Parton to particle level correction factors $T_{N_{jet}}$ and $T_{\gamma_{iso}}$ for the different signal regions as obtained from SHERPA, and ALPGEN MC. In the upper part of the Table, only statistical errors are quoted. The lower part shows the SM parton to particle level correction factor averaged over both lepton flavours. SHERPA is used as the baseline and the deviation from ALPGEN is quoted as the systematic uncertainty.

Signal Region	Generator	$C^{*parton \rightarrow particle}$	$T_{N_{jet}}$	$T_{\gamma_{iso}}$
Electron Channel				
Inclusive	SHERPA	0.990 ± 0.006	-	0.990 ± 0.006
	ALPGEN	0.997 ± 0.002	-	0.997 ± 0.002
Exclusive	SHERPA	0.871 ± 0.011	0.883 ± 0.007	0.986 ± 0.009
	ALPGEN	0.900 ± 0.008	0.916 ± 0.007	0.982 ± 0.004
Lepton averaged correction factor(combined with muon channel)				
Inclusive	SHERPA	0.991 ± 0.004 (stat.) ± 0.004 (syst.)		
Exclusive	SHERPA	0.871 ± 0.007 (stat.) ± 0.028 (syst.)		

Comparison of Cross-Section Measurements to Theory Predictions

Table 6.5: Comparison of the cross-section measurements of the $pp \rightarrow l\nu\gamma\gamma$ process with the MCFM SM NLO predictions.

	σ^{fid} [fb] ($N_{jet} \geq 0$)	σ^{MCFM} [fb] ($N_{jet} \geq 0$)
$pp \rightarrow \mu\nu\gamma\gamma$	$7.1 + 1.3 - 1.2$ (Stat.) $+ 1.6 - 1.5$ (Syst.) ± 0.2 (Lumi.)	2.9 ± 0.2
$pp \rightarrow e\nu\gamma\gamma$	$4.3 + 1.8 - 1.6$ (Stat.) $+ 1.9 - 1.8$ (Syst.) ± 0.2 (Lumi.)	2.9 ± 0.2
$pp \rightarrow \ell\nu\gamma\gamma$	$6.3 + 1.1 - 1.0$ (Stat.) $+ 1.5 - 1.4$ (Syst.) ± 0.2 (Lumi.)	2.9 ± 0.2
	σ^{fid} [fb] ($N_{jet} = 0$)	σ^{MCFM} [fb] ($N_{jet} = 0$)
$pp \rightarrow \mu\nu\gamma\gamma$	3.5 ± 0.9 (Stat.) $+ 1.2 - 1.1$ (Syst.) ± 0.1 (Lumi.)	1.9 ± 0.2
$pp \rightarrow e\nu\gamma\gamma$	$1.9 + 1.4 - 1.1$ (Stat.) ± 1.2 (Syst.) ± 0.1 (Lumi.)	1.9 ± 0.2
$pp \rightarrow \ell\nu\gamma\gamma$	$2.9 + 0.8 - 0.7$ (Stat.) $+ 1.1 - 1.0$ (Syst.) ± 0.1 (Lumi.)	1.9 ± 0.2

A comparison of the measured cross section results with the SM theoretical prediction computed using MCFM at NLO is provided in Table 6.5. The systematic errors on the theoretical predictions are obtained by varying the QCD scale³, PDF⁴ and photon fragmentation functions⁵. The inclusive measurements are higher than the MCFM SM predictions at NLO. The difference is within measurement uncertainties (1.8σ). Moreover, the difference observed in the inclusive case when comparing the measurement with the corresponding MCFM prediction is expected, since MCFM is only Leading-Order in α_s with only one radiated quark or gluon. The exclusive cross section measurements, with contributions from events with additional quark or gluon suppressed, agree with the SM predictions within uncertainties.

³ QCD scale is the energy scale that the coupling constant (determines the magnitude of the force) depends on.

⁴ Parton Distribution Function (PDF) describes the momentum distribution functions of the partons within the incoming proton. They are measured with dedicated analyses at hadron colliders.

⁵ Photon fragmentation function describes the process of $q \rightarrow \gamma$. This process is difficult to calculate in theory and has to be constrained by dedicated experiment measurements.

6.2 Anomalous quartic coupling (aQGC) analysis

As introduced in Chapter 2, the $pp \rightarrow W\gamma\gamma + X$ measurement can also be used to set constraints on new physics in the form of anomalous quartic couplings (aQGC). The procedure of extracting 95% Confidence Level (CL) limits on the anomalous coupling parameters will be described in this section. Results and comparison with previous results from other experiments will also be discussed.

6.2.1 *Limits extraction procedure*

Cross sections with aQGC are generated by the VBFNLO event generator [26, 42, 43]. The number of expected events are obtained with correction factors and the integrated luminosity. A 95 % Confidence Level (CL) limit is extracted from the measurements based on a likelihood construction. Each step will be discussed below in detail.

aQGC cross sections

The exclusive $W\gamma\gamma$ cross-section measurement is used to assign limits on the parameters f_{M2} , f_{M3} and f_{T0} introduced in Chapter 2, Section 2.4. They generate anomalous couplings which enhance $W\gamma\gamma$ production. The diphoton invariant mass $m_{\gamma\gamma}$ is required to be larger than 300 GeV to maximize the sensitivity to aQGC. The aQGC terms are added linearly to the SM amplitude A_0 at the matrix element (ME) level and the cross section is proportional to the square of the ME:

$$|A_0 + \sum f_{M_i} \times A_i|^2 \quad (6.13)$$

Therefore the aQGC cross-sections with non-zero aQGC parameter f can be expressed as a quadratic function of f :

$$\sigma_{pp \rightarrow l\nu\gamma\gamma+X}(f) = p_2 f^2 + p_1 f + p_0. \quad (6.14)$$

Here p_0 represents the SM contribution, while p_1 and p_2 parametrize the aQGC contributions. The coefficients p_i 's are obtained from a fit to generated aQGC cross-section points as shown in Figure 6.1. The number of expected events can be written as:

$$N(f) = A \times C \times \int \mathcal{L} dt \times (p_2 f^2 + p_1 f + p_0) \quad (6.15)$$

where A and C are the acceptance and detection efficiency factors for the kinematic region requiring $m_{\gamma\gamma} > 300$ GeV and $\int \mathcal{L} dt$ is the integrated luminosity. The correction factors are recomputed using `Madgraph` [44] generated aQGC events passing full detector simulation in the region with $m_{\gamma\gamma} > 300$ GeV. This is documented in Appendix B.

Profile likelihood formalism

A frequentist approach [45] using a profile likelihood fit is used to derive the 95% Confidence Level (CL) limits on the aQGC parameters. A similar likelihood function to Equation 6.8 can be constructed as following:

$$L(f, \{x_k\}) = \prod_{i=1}^2 \left(\frac{e^{-(N_s^i(f, \{x_k\}) + N_b^i(\{x_k\}))} \times (N_s^i(f, \{x_k\}) + N_b^i(\{x_k\}))^{N_{obs}^i}}{(N_{obs}^i)!} \right) \times \prod_{k=1}^n e^{-x_k^2/2}. \quad (6.16)$$

with $N_s^i(f, \{x_k\})$ and $N_b^i(\{x_k\})$ defined as following (same as in Eq 6.6):

$$N_s^i(f, \{x_k\}) = (p_2 f^2 + p_1 f + p_0) \times A_{W\gamma\gamma \rightarrow l\nu\gamma\gamma}^i \times C_{W\gamma\gamma \rightarrow l\nu\gamma\gamma}^i \times \int \mathcal{L} dt \times (1 + \sum_{k=1}^n x_k S_k^i) \quad (6.17)$$

$$N_b^i(\{x_k\}) = N_b^i(1 + \sum_{k=1}^n x_k B_k^i). \quad (6.18)$$

Here the parameter of interest f is one of the selected aQGC parameters (f_{T0} , f_{M2} , f_{M3}). p 's are determined by the parabolic fit. Index i runs over electron and muon

channels while index k runs over the sources of systematic uncertainties. The correction factors (A and C) are recomputed for the aQGC region (with $M\gamma\gamma > 300$ GeV.) In order to avoid writing Equation 6.16 repeatedly in the following section to define the 95% CL level, one can write:

$$N_s^i(f, \{x_k\}) + N_b^i(\{x_k\}) = N_{exp}^i(f, \boldsymbol{\theta}) \quad (6.19)$$

with $\boldsymbol{\theta}$ defined as the vector of systematic sources $\boldsymbol{\theta} = \begin{pmatrix} \boldsymbol{\theta}_1 \\ \boldsymbol{\theta}_2 \end{pmatrix}$, where $\boldsymbol{\theta}_1$ ($\boldsymbol{\theta}_2$) gives the fractional systematic uncertainties on the signal and each background component for electron (muon) channel. If the systematic error associated with a source on a specific component is irrelevant, it is set to be 0 in the matrix. For example, the uncertainty due to muon momentum resolution on the signal yield in the electron channel is obviously 0.

Therefore Equation 6.16 can be simplified as :

$$L(f, \boldsymbol{\theta}) = \prod_{i=1}^2 \text{Poisson}(N_{data}^i, N_{exp}^i(f, \boldsymbol{\theta})) \times e^{-\frac{1}{2}(\boldsymbol{\theta} \cdot C^{-1} \cdot \boldsymbol{\theta})} \quad (6.20)$$

Pseudo Experiments and 95% CL limits

Test statistics can be constructed for pseudo-experiments based on the likelihood function constructed in the last Section. A 95% CL limit can then be defined with the test statistics.

In each pseudo experiment, the number of data N_{ps}^i following a Poisson distribution with the mean of $N_{sig}^i(f_{test}) + N_{bkg}^i$ is generated. The estimation of N_{sig}^i and N_{bkg}^i of each pseudo experiment is done by shifting the nuisance parameter to non-zero value of θ_0 following the Gaussian distribution. The likelihood function of the pseudo experiment is:

$$L(N_{ps}^i, \boldsymbol{\theta}_0; \mathbf{f}, \boldsymbol{\theta}) = \prod_{i=1}^2 \text{Poisson}(N_{ps}^i, \psi^i(\mathbf{f}, \boldsymbol{\theta})) \times e^{-\frac{1}{2}((\boldsymbol{\theta} - \boldsymbol{\theta}_0) \cdot C^{-1} \cdot (\boldsymbol{\theta} - \boldsymbol{\theta}_0))}, \quad (6.21)$$

The profile likelihood ratio is defined to be:

$$\lambda(N_{\text{ps}}^i, \boldsymbol{\theta}_0; f_{\text{test}}) = \frac{L(N_{\text{ps}}^i, \boldsymbol{\theta}_0; f_{\text{test}}, \hat{\boldsymbol{\theta}})}{L(N_{\text{ps}}^i, \boldsymbol{\theta}_0; \hat{\mathbf{f}}, \hat{\boldsymbol{\theta}})}. \quad (6.22)$$

Here, the values f and θ which maximizes the likelihood are denoted by \hat{f} and $\hat{\theta}$ and $\hat{\theta}$ denotes the value of θ which maximizes the likelihood for a fixed value of f as f_{test} . The pseudo experiment is considered less likely than actual if its profile likelihood ratio is smaller than that of actual data:

$$\lambda(N_{\text{ps}}^i, \boldsymbol{\theta}_0; f_{\text{test}}) < \lambda(N_{\text{data}}^i, \mathbf{0}; f_{\text{test}}) \quad (6.23)$$

The p-value of a test value f_{test} , $p(f_{\text{test}})$, is defined as the ratio of the number of pseudo experiments which are less likely than actual to the total number of pseudo experiments generated. The upper 95% CL limit is the value of f_{test} which has the $p(f_{\text{test}})$ less than 5%. 10000 pseudo experiments were generated, corresponding to a statistical uncertainty of $\pm 0.2\%$ on a p-value of 5%.

6.2.2 Unitarity constraint

As introduced in Chapter 2, the effective Lagrangian terms of the aQGCs generate diverging cross sections at high energy region (unitarity violation). To preserve unitarity up to high energy scales, the conventional procedure is to modify the coupling parameters with an energy dependent form factor. A typical choice is the dipole form factor which modifies the aQGC parameters in the following way:

$$f \rightarrow \left(1 + \frac{s}{\Lambda_{\text{FF}}^2}\right)^{-n} \times f. \quad (6.24)$$

where s is the energy scale of the process which is equivalent to the invariant mass of $W\gamma\gamma$ system. For values of s above the form factor scale, Λ_{FF} , it reduces aQGC

contributions to restore SM predictions. For large n the form factor is effectively a cutoff on the effects of the anomalous couplings at Λ_{FF} , so that for $s > \Lambda_{\text{FF}}$ any distribution becomes constrained to its SM expectation. The undesirable consequence of introducing such a form factor is that any limits found will depend on the choices of n and Λ_{FF} . The appropriate value of Λ_{FF} is chosen with the help of the `calc_formfactor` program [46]. $\Lambda_{\text{FF}} = 500$ GeV (600 GeV) was used to compute the limits for f_{M2} , f_{M3} (f_{T0}). The process studied here is a $2 \rightarrow 3$ process, while the calculation of the largest form factor scale ensuring unitarity above is based on $2 \rightarrow 2$ inelastic scattering processes. Therefore the choice of $n = 2$ is too conservative for $W\gamma\gamma$ -production. An exponent of $n = 1$ was used in the final calculation.

6.2.3 Results

The parabolic fit to express the cross-section as a function of the aQGC parameters (f_{M2} , f_{M3} and f_{T0}) are shown in Figure 6.1. By using the statistical method described in Section 6.2.1, one can extract the expected limits using simulated number of signal events and observed limits using observed signal events in data. The expected and observed limits are shown in Table 6.6. Results were obtained for the electron and muon channels and also their combination.

6.2.4 Comparison to other experiments

Limits on anomalous quartic gauge couplings have been set by the L3 [47], D0 [48] and CMS [49, 50] experiments. The limits summarized in Table 6.6 have to be transformed to account for a different parameterization of the aQGCs between VBFNL0 and `MadGraph` [51]. The limits on f_{M2} and f_{M3} are converted to a_0^W and a_C^W using the relations shown in Equation 2.8 in Chapter 2. The comparison to other experiments is summarized in Figure 6.2.

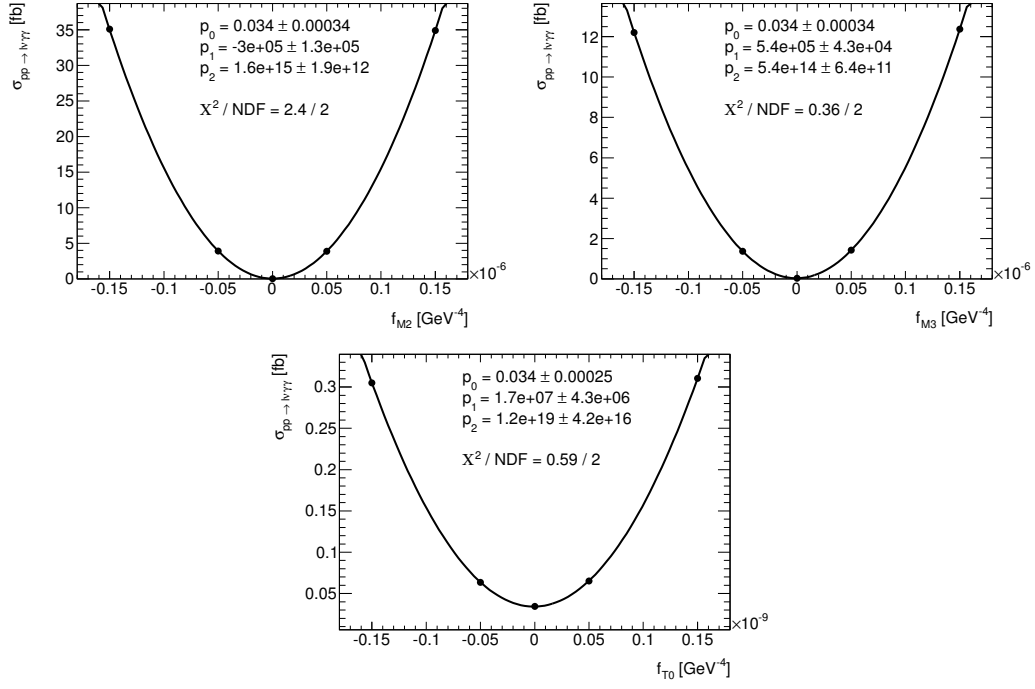


FIGURE 6.1: Cross-section and parabolic fit as a function of the coupling for the three operators F_{M2} , F_{M3} and F_{T0} . The parameters and goodness of the fit are given in the graphs.

Table 6.6: Expected and observed 95% limits obtained analyzing the full 2012 data sample for the f_{M2} , f_{M3} and f_{T0} aQGC parameters in each of the two decay channels studied and for the combination of the two.

Expected limits				
	$e\nu\gamma\gamma$	$\mu\nu\gamma\gamma$	$\ell\nu\gamma\gamma$	
n=1	f_{M2}	$[-8.6, 8.7] \times 10^{-8}$	$[-7.5, 7.7] \times 10^{-8}$	$[-5.7, 5.9] \times 10^{-8}$
	f_{M3}	$[-1.7, 1.6] \times 10^{-7}$	$[-1.5, 1.4] \times 10^{-7}$	$[-1.1, 1.0] \times 10^{-7}$
	f_{T0}	$[-1.5, 1.4] \times 10^{-9}$	$[-1.3, 1.3] \times 10^{-9}$	$[-9.6, 9.5] \times 10^{-10}$
Observed limits				
	$e\nu\gamma\gamma$	$\mu\nu\gamma\gamma$	$\ell\nu\gamma\gamma$	
n=1	f_{M2}	$[-7.3, 7.4] \times 10^{-8}$	$[-6.2, 6.5] \times 10^{-8}$	$[-4.4, 4.6] \times 10^{-8}$
	f_{M3}	$[-1.4, 1.3] \times 10^{-7}$	$[-1.2, 1.2] \times 10^{-7}$	$[-8.9, 8.0] \times 10^{-8}$
	f_{T0}	$[-1.2, 1.2] \times 10^{-9}$	$[-1.1, 1.0] \times 10^{-9}$	$[-7.6, 7.3] \times 10^{-10}$

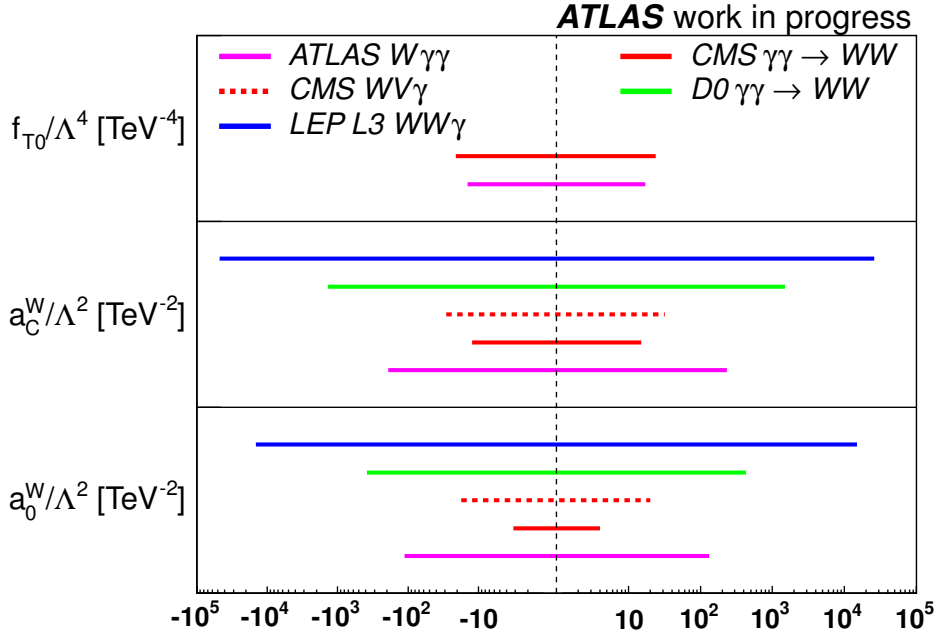


FIGURE 6.2: Comparison of the 95% exclusion limits on f_{M2} , f_{M3} and f_{T0} obtained from different measurements.

Comparison of ATLAS measurement to LEP The 95% confidence level limits on a_0^W and a_c^W presented by the OPAL experiment [52] at LEP are:

$$-0.020 \text{ GeV}^{-2} < a_0^W < 0.020 \text{ GeV}^{-2}, \quad (6.25)$$

$$-0.052 \text{ GeV}^{-2} < a_c^W < 0.037 \text{ GeV}^{-2}. \quad (6.26)$$

Translated to the limits on FM2 and FM3:

$$-48.1 \times 10^{-9} \text{ GeV}^{-4} < f_{M2} < 48.1 \times 10^{-9} \text{ GeV}^{-4}, \quad (6.27)$$

$$-125.1 \times 10^{-9} \text{ GeV}^{-4} < f_{M3} < 89.0 \times 10^{-9} \text{ GeV}^{-4}. \quad (6.28)$$

The limits found in this analysis are significantly improved compared to LEP.

Comparison of ATLAS measurement to CMS The $WW\gamma\gamma$ coupling has been studied in the $W(l\nu)V(jj)\gamma$ process at the CMS [53]. The $W\gamma\gamma$ results are less constraining on f_{M2} and f_{M3} than the previous ones due to different sensitivities in

the $W\gamma\gamma$ and $WV\gamma$ final states. However this analysis does not provide limits on f_{T0} . The $\gamma\gamma \rightarrow WW$ analysis also studied anomalous quartic couplings and provided limits on f_{M2} , f_{M3} and f_{T0} . The limit on f_{T0} from the ATLAS $W\gamma\gamma$ measurement is improved compared to the CMS $\gamma\gamma \rightarrow WW$ analysis.

6.3 Results and Conclusions

The first observation of $W\gamma\gamma$ production at the LHC was performed by analyzing 20.3 fb^{-1} of ATLAS data collected from proton-proton collisions at $\sqrt{s} = 8 \text{ TeV}$. Fiducial cross sections are measured for the “inclusive” case, where no jet requirement is applied, and for the “exclusive” case, where there is no reconstructed jet ($p_T(\text{jet}) > 30 \text{ GeV}$, $|\eta(\text{jet})| < 4.4$) in the final state. The measurement compares well, within uncertainties, in the exclusive case with the SM theoretical prediction given by the MCFM Next-to-Leading-Order calculations. Moreover, the difference observed in the inclusive case when comparing the measurement with the corresponding MCFM prediction is expected, since MCFM is only Leading-Order in α_s with one radiated quark or gluon.

The exclusive fiducial measurement in a very high diphoton mass region ($M_{\gamma\gamma} > 300 \text{ GeV}$) is also used to determine the limits of the anomalous Quartic Gauge Boson Coupling parameters at the 95% confidence level. No deviations from the SM are observed.

Analysis of $W(e\nu) + \gamma$ Produced via Vector Boson Scattering in pp collisions

An analysis of $W(e\nu) + \gamma$ events produced with two energetic forward/backward hadronic jets that are initiated by incoming quarks (VBS $W(e\nu) + \gamma$ production) is presented in this Chapter. The selection criteria of events produced with this topology is reviewed along with the results of the data analysis. The expected significance of the measurement is also discussed.

7.1 Analysis strategy

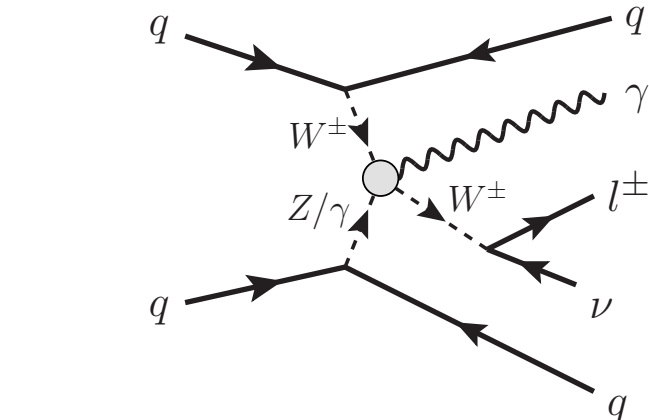


FIGURE 7.1: Vector boson scattering producing $W\gamma$ events.

The process of interest, $W\gamma$ VBS, is shown in Figure 7.1. The incoming quarks inside the protons colliding with an energy of 4 TeV are very energetic and can emit an EWK boson. The main background to this process comes from $W\gamma$ events, where the photon is produced via initial state radiation off the incoming quark, final state radiation off the lepton or triple gauge boson coupling. A $W\gamma$ event with lower order EWK diagrams¹ can be misidentified as a signal event if there are two hadronic jets present in the final state. These are referred to as $W\gamma$ QCD events.

The analysis starts with a sample of inclusive $W\gamma$ events and a subset events with two additional hadronic jets. Data analysis is performed on these two samples in order to understand backgrounds due to misidentified objects, such as $W+jets$ with a jet faking the photon. In order to separate $W\gamma$ QCD events and $W\gamma$ VBS events, cuts are applied on the kinematic variables of the two jets based on their features of being very energetic and forward. Optimization of these variables to separate VBS $W\gamma$ events from $W\gamma$ QCD events is carefully performed to maximize the measurement sensitivity.

¹ The $W\gamma$ VBS process of interest is of order 5 in the EWK coupling.

7.2 Event Selection and Signal Region Definitions

In order to select events with $W(e\nu)\gamma$ candidates, the same dataset is used from pp collisions taken in 2012 as introduced in Chapter 5, Section 5.1. As introduced in Chapter 2, for the Standard Model simulation of the $W\gamma$ QCD and $W\gamma$ VBS processes, the leading order generator **SHERPA 1.3.1** [24] is used. The **SHERPA** samples are generated with up to three additional jets. All generated events are then passed through full detector simulation.

Events are required to pass the event quality selection described in Chapter 5, Section 5.2.1. A single object trigger is used requiring one electromagnetic object with transverse energy greater than 24 GeV. An electron passing the requirement shown in Chapter 5, Section 5.2.2 is required to be present in the final state. However the tight quality requirement is changed to a likelihood based electron ID [28]. Definitions of the selection criteria on photons, missing transverse energy, transverse mass of the W boson and hadronic jets also follow the description in Chapter 5. The p_T cut value of the electron and the photon differ from what is used in $W\gamma\gamma$ analysis because different triggers are used.

Selected $W(e\nu)\gamma$ candidates are divided into three categories: inclusive events, events with two jets and events in the vector boson scattering (VBS) region. The criteria used to categorize these three regions are listed below:

- Inclusive $W(e\nu) + \gamma$ selection:
 - Require an isolated electron with $p_T > 25$ GeV, passing the quality selection cuts.
 - Events are rejected if there is a second electron with $p_T > 10$ GeV, passing all electron quality criteria discussed above with the tightest quality cut loosened to the medium one. This rejects $Z(ee)$ events with fake E_T^{miss}

due to imperfect reconstruction and where one electron is misidentified as a photon due to missing matched tracks in the ID or hard bremsstrahlung of the electron.

- Require $E_T^{miss} > 35$ GeV.
- Require the transverse mass of the electron and neutrino system $M_T(e, \nu) > 40$ GeV. ²
- Require one isolated photon with $p_T > 15$ GeV, passing the selection described in Section 5.2.2.
- 2 jet $W(e\nu)\gamma$ selection : $W(e\nu)\gamma$ events with two jets with $p_T > 30$ GeV and $|\eta| < 4.4$.
- VBS $W(e\nu)\gamma$ selection : 2 jet events with $M_{jj} > 600$ GeV, $dY_{jj} > 2.0$, and pt balance < 0.1. Here M_{jj} is the invariant mass of the selected two jets, Y stands for rapidity defined as $\frac{1}{2}\ln\frac{E+p_{zc}}{E-p_{zc}}$, and dY_{jj} is the rapidity difference between the two jets. pt balance is defined as the vector sum of the \vec{p}_T of the selected electron, E_T^{miss} , photon and two jets, divided by the $|\vec{p}_T|$ scalar sum.

While the additional requirement in the 2 jet selection is obvious, the selection criteria to define the VBS region is carefully studied in order to optimize the sensitivity to events produced via the QGC couplings as shown in Figure 7.1. These events have a distinctive signature with two energetic forward jets initiated by the incoming quarks resulting in large M_{jj} and dY_{jj} compared to an event with additional jets initiated by gluon radiation. Studies show that M_{jj} and dY_{jj} are highly correlated. Therefore a two dimensional optimization study was performed. The results are shown in Figure 7.2. The significance is defined as S/\sqrt{B} , where S is the number of

² $M_T(e, \nu)$ is defined as $M_T(e, \nu) = \sqrt{2p_T^{el}p_T^\nu(1 - \cos[\phi^{el} - \phi^\nu])}$.

signal events predicted by the Monte Carlo simulated samples and B is the sum of the backgrounds taken from Monte Carlo simulation or data driven methods³. Pt balance shows additional separation after M_{jj} and dY_{jj} cuts were imposed as shown in Figure 7.3. An optimal point of $M_{jj} > 600$ GeV, $dY_{jj} > 2$, pt balance < 0.1 was chosen, resulting in an expected significance of 3.7 for electron channel only.

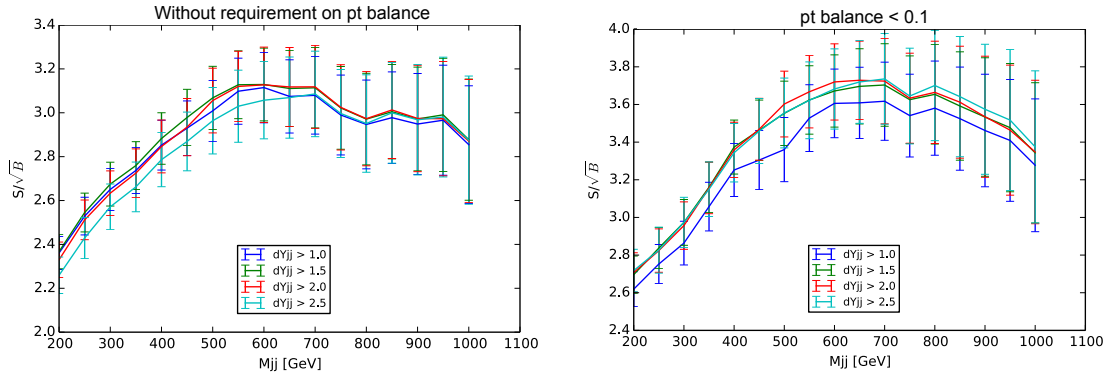


FIGURE 7.2: Optimization of the VBS region. Significance is defined as S/\sqrt{B} , where S is the number of signal events predicted by the Monte Carlo simulated samples, B is the sum of the backgrounds taken from Monte Carlo simulation or data driven methods. It is calculated for different M_{jj} and dY_{jj} sets of cuts.

7.3 Background analysis

A robust background analysis using data driven techniques in the inclusive and two jet regions are essential in understanding the backgrounds due to fake objects. It is difficult to perform data driven methods directly in the VBS region due to limited statistics in this very restricted phase space. These backgrounds are extrapolated

³ γ +jet background is not considered in the optimization studies. The reason is that at the time of writing, the estimation of this background has large associated statistical uncertainty, resulting in fluctuation in the calculated significance. This background is expected to be understood better using Monte Carlo simulated sample with enriched statistics. Omitting this background should not impact the optimal choice of M_{jj} and dY_{jj} , since these variables are studied mainly to suppress $W\gamma$ QCD background.

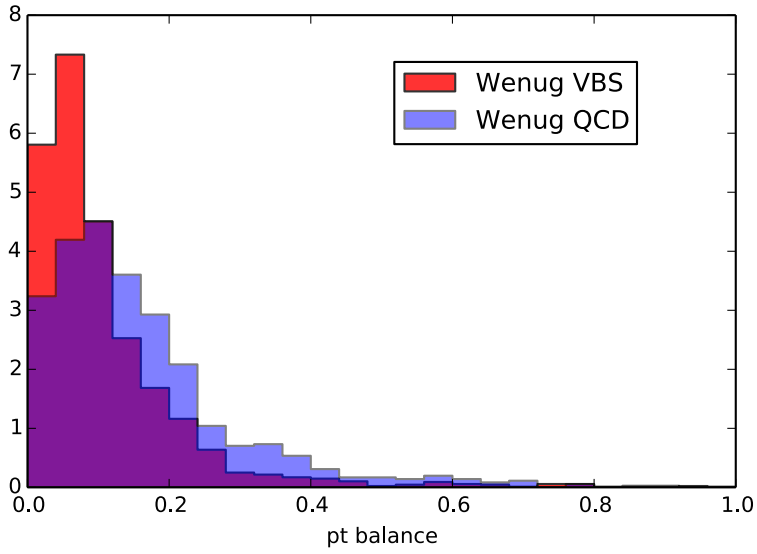


FIGURE 7.3: Pt balance distributions of $W(e\nu)\gamma$ VBS, $W(e\nu)\gamma$ QCD events after requiring $M_{jj} > 600$ GeV, $dY_{jj} > 2$. A selection cut for VBS events is applied at pt balance < 0.1 .

from the measurement in the two jet region. The data-driven estimates for the three regions are summarized in the following sections.

7.3.1 Inclusive selection of $W(e\nu)\gamma$

In selected inclusive $W(e\nu)\gamma$ events, the major contamination from other physics processes are from $pp \rightarrow W(e\nu) + jets$ events with a hadronic jet faking the photon and $\gamma + jets$ events with a jet faking the electron. Both of these backgrounds are estimated using the ABCD data driven method described in Chapter 5, Section 5.3, with different definitions of the control regions. This method provides correct normalizations for processes with additional QCD jets. NLO Monte Carlo samples with full detector simulation for these processes are not available at this time due to the complexity of NLO parton shower calculation. Another reason for using a data-driven method is that hadronic jets are not perfectly modeled by the ATLAS detector simulation.

The fake electron background estimate coming from $\gamma + jets$ events uses the same definition described in Chapter 5, Section 5.3.2 with the requirement on $P_T(l\gamma\gamma)$ removed as it is irrelevant in this analysis. The fake photon background coming from $W(e\nu) + jets$ uses the photon identification and photon isolation energy to define the control regions. It is safe to assume there is no correlation between these two variables as the identification uses a narrow electromagnetic shower which is reconstructed in towers of roughly 0.1×0.1 in $\Delta\eta \times \Delta\phi$ (the exact size depends on which specific part of the EM calorimeter one is looking at), while a cone size of 0.4 is used for the calculation of the isolation energy. This assumption can also be tested with the Monte Carlo simulation of $W(e\nu) + jets$ events. Details of the application of the ABCD method in these two cases can be found in Appendix A.

The production of a Z boson which subsequently decays to electrons, in association with or without a photon, may pass the event selection if one of the leptons is not

reconstructed, and one additional jet fakes the photon or if one of the electrons is misidentified as a photon. The first scenario is covered by the fake photon background estimate described above, since the photon is coming from a jet. The second scenario is estimated from simulated samples of $Z(ee)(\gamma)$ events. The reason this can be used is that the electromagnetic response of the detector is well modeled by Monte Carlo samples passing the full detector simulation.

Other backgrounds arise from events containing a real charged lepton and one real photon or multiple leptons and photons with lepton-photon misidentification. These include single top quark production with an additional photon and top quark pair production. These backgrounds are very small and are taken from predictions using Monte Carlo generated events passing full detector simulation. Even if 100% uncertainties are assigned on these backgrounds, the effects on the signal yield are very small.

7.3.2 2 jet region of $W(e\nu)\gamma$

When two additional hadronic jets are required in the final state, the background estimation procedures described above still apply. However one expects a very different distribution in the number of jets for $W\gamma$ events and background processes with misidentified objects as shown in Figure 7.4. For example, one expects more jets from the top quark pair decays as each top quark decays to a W boson and a b quark (detected as a b hadron). And the rate of $W(e\nu)\gamma$ QCD production with one additional hadronic jet initiated by gluon radiation is reduced by a factor of α_s associated with the strong coupling vertex. Therefor one expects a larger fraction of events with zero additional jets in $W\gamma$ QCD events. Figure 7.4 also shows that $W\gamma$ VBS signal is not visible without requirement imposed on the di-jet kinematic variables. The same data driven techniques used for the inclusive analysis were employed to estimate backgrounds with jets misidentified as the photon or the electron.

Details are documented in Appendix A.

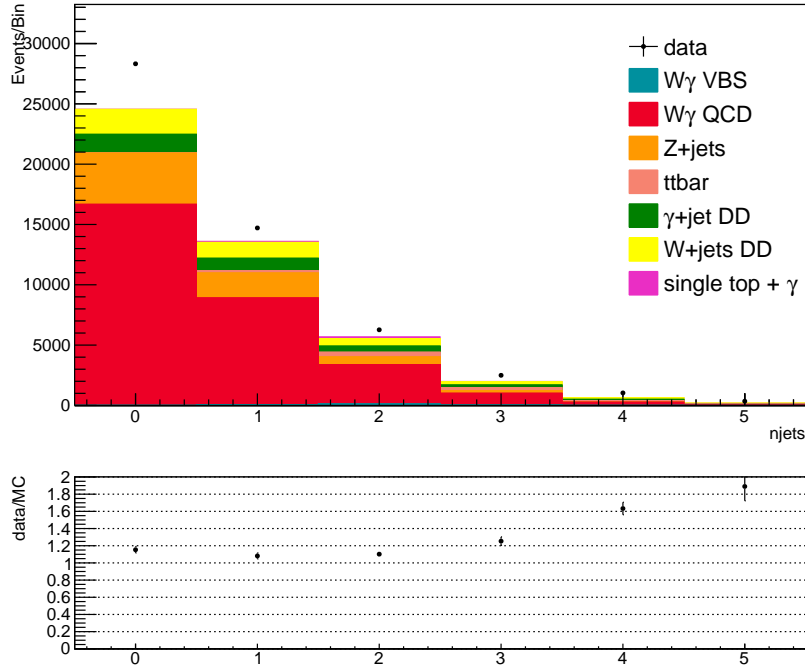


FIGURE 7.4: Distribution of number of jets for selected inclusive $W(e\nu)\gamma$ candidates. 'DD' stands for data driven.

7.3.3 VBS region of $W(e\nu)\gamma$

In order to select $W(e\nu)\gamma$ events, selection cuts on M_{jj} , dY_{jj} and pt balance are imposed. $W + jets$ and $\gamma + jets$ become less dominant while the contributions from single top with an additional photon and top quark pair production become larger. As data driven techniques suffer from poor statistics in the control regions in data, $W + jets$ and $\gamma + jets$ contributions are extrapolated from the 2 jet measurement.

Table 7.1: Number of candidate events in the electron channel for the inclusive, 2 jet and VBS categories. The number of background events with misidentified photons and leptons, estimated from data driven techniques, and other backgrounds from simulated samples are also shown. Row ' $N_{\text{data}} - N_{\text{bkg}}$ ' shows the sum of $W\gamma$ QCD and $W\gamma$ VBS events. Number of $W\gamma$ QCD events in VBS region is given by Monte Carlo full simulated sample generated by **SHERPA 1.3.1**. The uncertainty is statistical only.

	Inclusive	2 jet (nJets==2)	VBS
data	49085	5091	86
$W + \text{jets}$	9948.0 ± 277.7	697.9 ± 64.9	8.2 ± 2.0
$\gamma + \text{jets}$	5375.2 ± 376.4	622.6 ± 114.0	5.8 ± 3.4
$Z(\gamma)$	5448 ± 132	143 ± 5	6.0 ± 0.5
$t\bar{t}$	143 ± 5	50.1 ± 2.9	1.4 ± 0.4
single top + γ	148.9 ± 2.5	62.2 ± 1.6	6.0 ± 0.5
$N_{\text{data}} - N_{\text{bkg}}$	28022.5 ± 573.8	3132.4 ± 168.5	64.7 ± 8.4
$N_{W\gamma \text{ QCD}}$	N/A	N/A	49.0 ± 4.8
$N_{W\gamma \text{ VBS}}$	N/A	N/A	15.7 ± 9.7

7.4 Summary of the Event Yield

The numbers of observed events for the inclusive, 2 jet and VBS categories are shown in Table 7.1. The number of $W + \text{jets}$ and $\gamma + \text{jets}$ contributions are taken from data-driven estimations. Other backgrounds are taken from simulated Monte Carlo samples. VBS events are selected with the optimal cuts of $M_{jj} > 600$ GeV, $dY_{jj} > 2$ and $\text{pt balance} < 0.1$ applied. The final yield of VBS $W\gamma$ is 15.7 ± 9.7 , compared to 29 predicted by simulated VBS events generated by **SHERPA**. The statistical uncertainty on the signal yield is dominated by the $\gamma + \text{jet}$ and $W\gamma$ QCD backgrounds, expected to be reduced using Monte Carlo samples with enriched statistics in the VBS region. An improved estimation of the signal yield can then be obtained to compare with the SM theoretical predictions.

Kinematic variables from selected VBS events with cuts of $M_{jj} > 600$ GeV, $dY_{jj} > 2$ and $\text{pt balance} < 0.1$ imposed are shown in Figure 7.5. Electron p_T , missing transverse energy, transverse mass of the W boson, photon p_T and M_{jj} distributions are shown in the Figure. Backgrounds with misidentified photons and leptons are

estimated from data driven techniques and are labeled as 'DD' in the legend. Other backgrounds are taken from simulated samples. $W\gamma$ VBS events are generated by SHERPA and passed full detector simulation. As shown in the plot, γ +jet and $W\gamma$ QCD have limited statistics, smoother distributions are expected using Monte Carlo samples with enriched statistics in the VBS region.

7.5 Conclusions and plans

At the time of writing this thesis, the evaluation of the systematic uncertainties is in progress, with the majority contribution from the measurement of the di-jet system. Methods utilizing a fit to the M_{jj} templates to extract the signal yield will reduce this systematic uncertainty and are under investigation.

This analysis is also performed by collaborators with the W boson decaying to a muon and a neutrino. The muon channel exhibits improved statistics due to higher detection efficiency of the muons compared to electrons. Another reason is that no requirement is imposed on $M(\mu; \gamma)$ as the chance of an muon misidentified as an photon is significantly smaller than for electrons. The cross section and aQGC limits will be derived with the measurements from both electron and muon channels of the W boson decay.

As of December 2014, studies of WW produced in vector boson scattering published by the ATLAS and CMS collaborations [54] [55] are the only experimental evidence for di-boson produced via VBS. No results on $W\gamma$ production via vector boson scattering have been published. As shown in this Chapter, it is promising to have a first observation of the $W\gamma$ VBS process with the pp collision data set collected by the ATLAS detector in 2012.

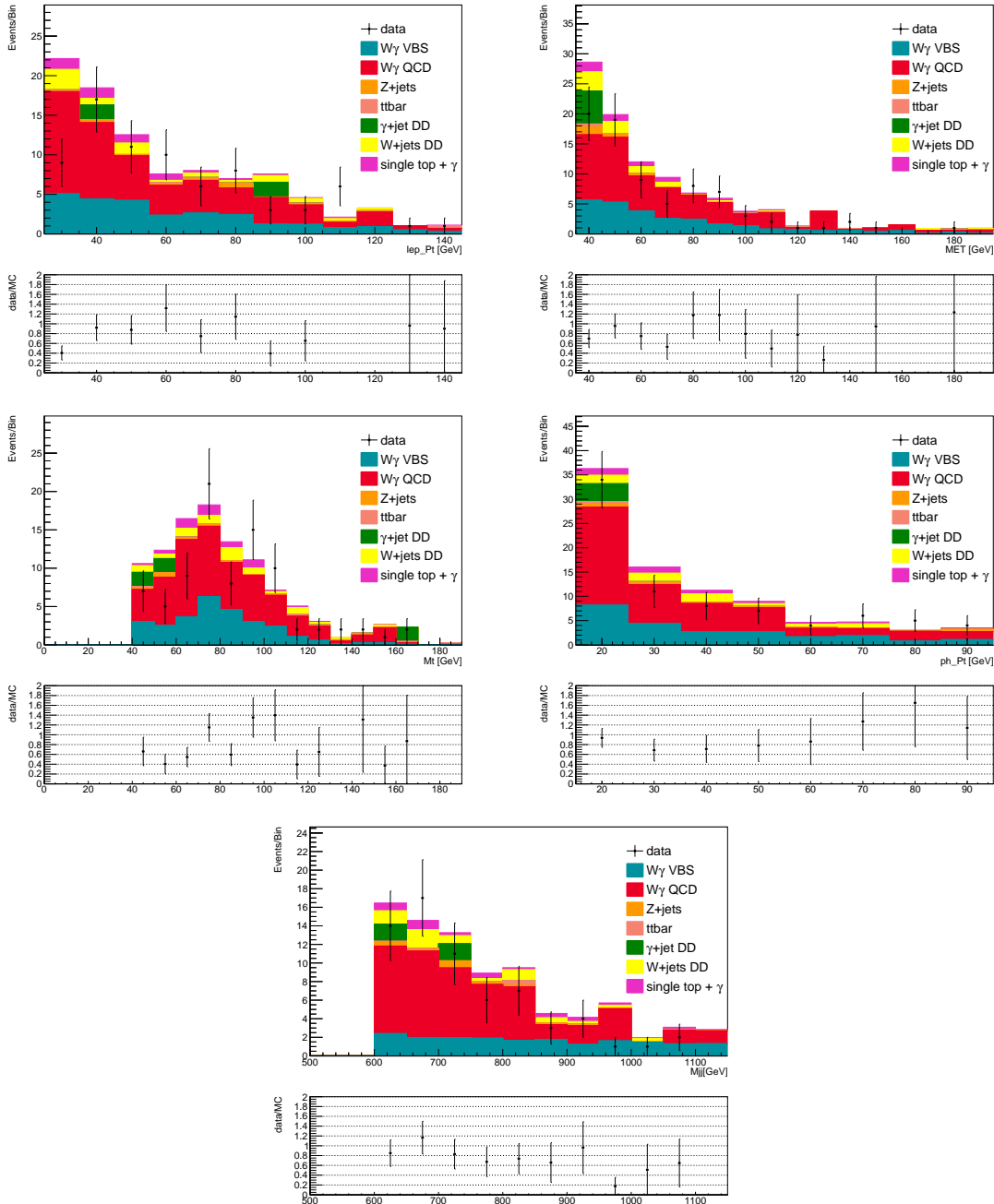


FIGURE 7.5: Selected kinematic distributions of VBS $W\gamma$ events with $M_{jj} > 600$ GeV, $dY_{jj} > 2$ and pt balance < 0.1 imposed. Backgrounds with misidentified photons and leptons are estimated from data driven techniques and are labeled as 'DD' in the legend. Other backgrounds are taken from simulated samples. Electron p_T (first row, left), missing transverse energy (first row, right), transverse mass of the W boson (second row, left), photon p_T (second row, right) and M_{jj} (bottom) distributions are shown.

8

Conclusions

The Standard Model is a gauge theory with its structure determined by the underlying $SU(3)_C \times SU(2)_L \times U(1)_Y$ symmetry. The $SU(2)_L \times U(1)_Y$ electroweak (EWK) sector predicts self-couplings between the gauge bosons (W, Z and γ), which generate signatures of multi-bosons at hadron collider experiments. Studies of these processes directly probe the gauge structure of the SM and provide insights into new physics which generates anomalous contributions to multi-boson production.

A first measurement of $pp \rightarrow W\gamma\gamma + X$ production has been presented. A dataset of 20.3 fb^{-1} pp collisions was used with a center of mass energy at 8 TeV collected by the ATLAS detector at the LHC. It is a first observation of tri-boson production predicted by the SM EWK sector, probing quartic gauge boson couplings which have not been studied experimentally. The measured cross sections agree with the SM predictions within uncertainties. Constraints are also provided on anomalous quartic couplings that are forbidden by the SM but can receive contributions from beyond Standard Model physics.

Measuring the production of $W\gamma$ in vector boson scattering (VBS) probes the QGC in a unique topology with two energetic forward jets. A preliminary sensitivity

study shows that it is a promising first measurement of VBS producing $V\gamma$ processes. At the time of writing, the LHC is scheduled to restart in June 2015 and expected to deliver pp collisions data with a center of mass energy at 13 TeV. The goal is to collect 100 fb^{-1} data by the next scheduled shutdown in 2018. This much larger dataset with higher center of mass energy provides opportunities of studying multi-boson production and vector boson scattering processes more precisely in a new energy range.

Appendix A

Experimental data-driven methods

Experimental data-driven techniques used in this thesis are described with more details in this Appendix. The Tag and probe method, ABCD method and 2D template fit method are summarized. Details on their applications to the studies documented in this thesis are also included.

A.1 Tag and Probe method

A.1.1 General Method

Tag and probe is a data driven technique generally used to calculate efficiencies. In order to do this, one needs a mass resonance (such as Z boson mass peak). The Tag is often a particle that has very tight selection applied to ensure its quality, the Probe has looser criteria. If the tag and probe pair pass additional selections, the probe is considered to be an unbiased sample that represents the real particles under study. Take electrons from Z decay for example, the probe is considered as a real electron if the mass of the tag and probe pair is close to the Z mass peak. The probe electrons are thus an unbiased sample from data. Efficiency of the probe can be calculated

by the number of probes passing the selection criteria under study divided by the total number of probes. This method is used to compute the electron reconstruction and identification efficiency as documented in [28] [35], and for photons in [36]. The application of getting the trigger efficiency in $W\gamma\gamma$ is described briefly as below.

A.1.2 Trigger efficiency in $W\gamma\gamma$

In $W\gamma\gamma$ analysis, the combined triggers “3g15_loose” and “mu18_2g10_medium” are used in the electron and muon channels respectively. The efficiency of g15_loose and g10_medium photon triggers are computed with photons from the radiative decay of the Z boson [56]. For tight isolated photons with $p_T > 20$ GeV, the overall efficiency of g15_loose is found to be $99.62^{+0.05\%}_{-0.06\%}$ and the efficiency of g10_medium $99.63^{+0.05\%}_{-0.06\%}$. Combined trigger efficiencies are estimated by multiplying the efficiencies of the single photon triggers.

A.2 ABCD method

A.2.1 General Formunilam

The ABCD method relies on definitions of three control regions (B, C and D) enriched in background events, and one signal region (A). Two minimally correlated variables are chosen to define regions B,C,D, therefore a simple relation can be given for background events:

$$N_A = N_C \frac{N_B}{N_D}, \quad (\text{A.1})$$

This relation can be tested with Monte Carlo simulated background samples. The ABCD method is often employed when background events are not well modeled by Monte Carlo simulated samples, for example processes with hadronic jets. The normalization of these processes are often not well understood and accurate detector response to hadronic jets is difficult to obtain in simulation.

The application of this method has to consider the fact that there are signal events and other background events in the control regions, as well as the fact that there is small correlation between the two variables used to define regions B,C,D. Contributions from other backgrounds are often taken from the Monte Carlo predictions and are subtracted from control regions. For signal events, the normalization is unknown. This has to be taken into consideration in control regions as well. The formula considering all of these factors is given as below.

With the assumption that the selections are minimally correlated, neglecting signal events leaked into the control regions, one can write the number of signal (N_A^S) and background events in region A (N_A^F) as

$$N_A^S = N_A - N_A^F - N_A^{\text{Other}} = N_A - (N_C - N_C^{\text{Other}}) \cdot \left(\frac{N_B - N_B^{\text{Other}}}{N_D - N_D^{\text{Other}}} \right) - N_A^{\text{Other}}, \quad (\text{A.2})$$

where N_i is the number of events measured in region i and N_i^{Other} is the number of events in region i from other processes estimated with Monte Carlo. Monte Carlo studies often show that the amount of signal events in the control regions is not negligible. To account for this, the number of events is corrected using the signal leakage from Monte Carlo simulated signal samples. With this correction, Equation (A.2) changes to

$$N_A^S = N_A - N_A^F - N_A^{\text{Other}} = N_A - (N_C - N_C^{\text{Other}} - c_C N_A^S) \cdot \left(\frac{N_B - N_B^{\text{Other}} - c_B N_A^S}{N_D - N_D^{\text{Other}} - c_D N_A^S} \right) - N_A^{\text{Other}}, \quad (\text{A.3})$$

where the c_i is the signal leakage into region i . It is derived from Monte Carlo defined as:

$$c_i = \frac{N_i^{\text{Signal,MC}}}{N_A^{\text{Signal,MC}}}. \quad (\text{A.4})$$

In order to account for the bias due to correlations between the two variables , a

correlation factor R , is introduced:

$$R = \frac{N_D^F \cdot N_B^F}{N_A^F \cdot N_C^F} \quad (\text{A.5})$$

and is derived from background Monte Carlo. The R factor is often set to one in calculating the central value. This is based on the fact that the MC estimation for R factor is often not reliable due to large uncertainties with low statistic samples. A systematic uncertainty is assigned by varying the R factor from one to the value give by the MC simulation.

The analytical solution of Equation A.3 is:

$$N_A^F = N_A - N_A^{\text{Other}} - \frac{E \cdot (-1 + \sqrt{1 + F})}{G} \quad (\text{A.6})$$

$$E = N_C - N_C^{\text{Other}} + c_C(N_A - N_A^{\text{Other}}) - \frac{c_B}{R}(N_D - N_D^{\text{Other}}) - \frac{c_D}{R}(N_B - N_B^{\text{Other}}) \quad (\text{A.7})$$

$$F = \frac{4}{E^2} \left(\frac{c_B c_C}{R} - c_D \right) ((N_A - N_A^{\text{Other}})(N_C - N_C^{\text{Other}}) - \frac{1}{R}(N_B - N_B^{\text{Other}})(N_D - N_D^{\text{Other}})) \quad (\text{A.8})$$

$$G = 2 \left(\frac{c_B c_C}{R} - c_D \right) \quad (\text{A.9})$$

The applications of this method in $W\gamma\gamma$ to estimate the jet faking electron background and in vector boson scattering $W\gamma$ events to estimate the jet faking electron or jet faking photon backgrounds are documented in the following sections.

A.2.2 Jet faking electrons in $W\gamma\gamma$

In the electron channel, the signal selection includes a requirement on the total transverse momentum of the lepton and photons system p_T^{tot} (cf. Section 3.5), which is also used in the definition of the regions, in addition to M_T and E_T^{miss} . In addition, the low M_T and low E_T^{miss} or p_T^{tot} control region with tight isolated electrons (region D) are dominated by $Z\gamma$ events. Therefore some electron quality requirements are also reversed to suppress these events containing real electrons and enhance the

fraction of fake electrons. The inverted electron variables used in the definition of control regions C and D are:

- **Calo strip variables:**

- w_2 : lateral width of the electron shower
- w_{stot} : total lateral electron shower width
- $Eratio$: ratio of the energy difference between the largest and second largest energy deposits over the sum of these energies.

- **Track quality variables:**

- d_0 : electron track impact parameter
- E/p : ratio of electron energy measured in EM calorimeter and track momentum
- $\Delta\eta$: matching criteria between track and EM calorimeter shower position in η
- $\Delta\phi$: matching criteria between track and EM calorimeter shower position in ϕ

The definition of the four regions used in the electron channel is summarized in Table A.1. The number of events observed in data as well as the number of events from Monte Carlo is given in Table A.2 for each of the four regions. The signal leakage parameters are given in Table A.3.

The estimation of the fake-electron background is subject to different sources of systematic uncertainties. The assumption that the distribution of the variables used

Table A.1: Definition of signal (A) and control regions (B, C, D) using electron isolation, missing transverse energy, transverse mass and total transverse momentum requirements. The track quality requirements are relaxed for non-isolated control region B and C to increase statistics in these regions. The electron calo strip and EM calorimeter track matching variables are inverted to suppress the $Z\gamma$ background in low M_T and low E_T^{miss} or low p_T^{tot} control region (C, D) in which this background is dominant

Electron Channel				
Requirement	A (Signal region)	B	C	D
Electron isolation	isolated	non-isolated	non-isolated	isolated
Electron ID:				
Baseline requirement	tightPP	tightPP	tightPP	tightPP
Relax track quality	No	Yes	Yes	No
Invert calo strip cuts	No	No	Yes	Yes
Invert track matching cuts	No	No	Yes	Yes
E_T^{miss} [GeV]	> 25	> 25	< 25	< 25
p_T^{tot} [GeV]	> 30	> 30	< 30	< 30
M_T [GeV]	> 40	> 40	< 40	< 40

to define the sidebands is uncorrelated is one of these sources. The R -factor was found to be 0.8 ± 0.6 (stat.) and 0.7 ± 1.2 (stat.) for inclusive and exclusive measurement, respectively, using simulated events. Given the large uncertainty of R , the nominal background estimate is calculated using $R = 1.0$. The difference to the background estimated calculated with $R_{\text{syst}} = 0.8$ (0.7) for inclusive (exclusive) measurement is treated as systematic uncertainties. The estimated backgrounds using

Table A.2: The number of observed events in data and the contribution from EW processes with real electron (N^{EW}) predicted by MC simulation in control region A, B, C and D. The MC estimations are normalized to the process cross section and luminosity.

Electron Channel				
	A	B	C	D
$W\gamma\gamma$	18.6 ± 0.5	0.15 ± 0.05	0.01 ± 0.01	0.4 ± 0.1
$W\gamma$	16.0 ± 1.6	0	0.09 ± 0.09	0.3 ± 0.2
$Z\gamma$	11.7 ± 1.4	0	0.2 ± 0.2	3.3 ± 0.8
$t\bar{t}$ bar	2.3 ± 0.8	0	0.01 ± 0.01	0
Total EW events (N^{EW})	48.6 ± 2.3	0.15 ± 0.05	0.31 ± 0.2	4.0 ± 0.8
Observed data	49 ± 7	7 ± 3	263 ± 16	60 ± 8

Table A.3: Signal leakage parameters used to calculate the fake-electron background.

Electron Channel		
	Inclusive	Exclusive
c_B	0.008 ± 0.003	0.005 ± 0.004
c_C	0	0
c_D	0.022 ± 0.004	0.03 ± 0.01

R_{syst} are 1.8 ± 0.6 (stat.) and 0.3 ± 0.2 (stat.) for inclusive and exclusive measurements, respectively. Another systematic uncertainty is due to the definition of the control regions. The control region definitions are modified and the number of estimated fake-electron events is recalculated. The difference from the nominal value is taken as the systematic uncertainty. Control region definitions used and the resulting fake-electron estimates are summarized in Table A.4.

Table A.4: Results of the fake-electron background estimation with the ABCD method for several different choices of the control region definitions. The deviation is taken as an systematic uncertainty on the nominal value.

Electron Channel				
	Modified Control Region		inclusive	exclusive
Electron Quality	Invert Calo Strip Cuts		2 ± 1 (stat.)	-
	Invert Track Matching Cuts		1.4 ± 0.7 (stat.)	0.1 ± 0.1 (stat.)
Low MET	$E_{\text{T}}^{\text{miss}} < 20$ GeV			
	$p_{\text{T}}^{\text{tot}} < 25$ GeV		1.3 ± 0.5 (stat.)	0.2 ± 0.2 (stat.)
Tighter Isolation	$M_{\text{T}} < 35$ GeV			
	$E_{\text{T}}^{\text{iso}}/E_{\text{T}} > 0.25$			
	$p_{\text{T}}^{\text{iso}}/p_{\text{T}} > 0.2$		1.0 ± 0.6 (stat.)	0.3 ± 0.3 (stat.)

The results for the fake-electron background using the inclusive selection is

$$N_{\text{fake-electron}}^{\text{incl}} = 1.4 \pm 0.6 \text{ (stat.)} \pm 0.8 \text{ (syst.)} .$$

For the exclusive selection it is

$$N_{\text{fake-electron}}^{\text{excl}} = 0.2 \pm 0.2 \text{ (stat.)} \pm 0.2 \text{ (syst.)} .$$

A breakdown of the systematic uncertainties is given in Table A.5.

Table A.5: Breakdown of the size of the systematic uncertainties affecting the fake-electron background estimation for the inclusive and exclusive selection.

Electron Channel		
Uncertainty	<i>inclusive</i>	<i>exclusive</i>
R-factor	29 %	50 %
Electron Quality	43 %	50 %
Low MET	7 %	50 %
Tighter Isolation	29 %	50 %
Total	57 %	100 %

A.2.3 Jet faking electron and photon background in Vector Boson Scattering $W\gamma$

The ABCD method is used to estimate both the jet faking electron and photon background for the inclusive and two jet selections of $W\gamma$ events. The control regions used to estimate the fake photon background is labeled as B, C, D regions. Control regions for jet faking electron estimate are labeled as B' , C' , D' regions. The definitions of the control regions are summarized in Tables A.6 and A.7. Data driven estimations using these definitions are applied in data and the results are summarized in Table A.8 for both inclusive and two jet selections.

Table A.6: Control region definitions for jet faking photons. non-isolated region is defined by reversing photon isolation cut, i.e. $Iso > 6GeV$, non-tight region is defined the same way by requiring a non-tight photon passing the requirement in Chapter 5 in the event.

Regions	A (Signal region)	B	C	D
Requirement	isolated	non-isolated	non-tight	non-isolated and non-tight

Table A.7: Control region definitions for electron faking photons. non-isolated region is defined by reversing electron isolation cut, i.e. $Iso/p_T > 0.1$, low-MET regions is defined to be : $MET < 20GeV, M_T < 20GeV$.

Regions	A (Signal region)	B'	C'	D'
Requirement	isolated	non-isolated	low MET	non-isolated and low MET

Table A.8: The event counts in signal and control regions for different processes from data and Monte Carlo simulated samples. Monte Carlo closure tests and signal leakage parameters as well as the results from ABCD data driven method.

Process	Inclusive selection			D'		
	A	B	C	D	B'	C'
data	49085 \pm 222	13766 \pm 117	15622 \pm 125	11335 \pm 106	1455 \pm 38	19801 \pm 141
$W(e\nu)\gamma\nu$ bs	204.0 \pm 2.9	34.4 \pm 1.2	14.6 \pm 0.8	3.2 \pm 0.4	2.70 \pm 0.33	11.7 \pm 0.7
$W(e\nu)\gamma$	28699 \pm 113	2476 \pm 33	2528 \pm 33	279 \pm 11	316 \pm 12	2145 \pm 31
$W(e\nu)\bar{t}$	5190 \pm 256	2452 \pm 157	4583 \pm 239	3054 \pm 165	52 \pm 30	232 \pm 54
zee	5448 \pm 132	1868 \pm 79	890 \pm 53	397 \pm 36	48 \pm 13	7403 \pm 162
dp	5631 \pm 1233	2334 \pm 758	756 \pm 405	1320 \pm 494	1791 \pm 593	2743 \pm 832
$t\bar{t}$	143 \pm 5	36.3 \pm 2.6	32.4 \pm 2.3	25.3 \pm 2.0	2.5 \pm 0.8	2.3 \pm 0.7
$t\gamma$	148.9 \pm 2.5	11.9 \pm 0.7	10.5 \pm 0.7	1.49 \pm 0.25	1.34 \pm 0.24	5.8 \pm 0.5
Data driven method						
R	C_B	C_C	C_D	R'	C'_B	C'_D
1.41 \pm 0.16	0.0863 \pm 0.0012	0.0881 \pm 0.0012	0.0097 \pm 0.0004	0.6 \pm 0.5	0.0110 \pm 0.0004	0.0748 \pm 0.0011
MC closure and signal leakage parameters						
W+jets	9948.0 \pm 277.7	γ +jets	5375.2 \pm 376.4	28022.5 \pm 573.8	Signal yield	0.00074 ± 0.00011
Process	Exclusive two jet selection			D'		
	A	B	C	D	B'	C'
data	5091 \pm 71	1683 \pm 41	1249 \pm 35	1343 \pm 37	1.92 \pm 14	1440 \pm 38
$W(e\nu)\gamma\nu$ bs	103.7 \pm 2.1	9.7 \pm 0.6	6.1 \pm 0.5	0.73 \pm 0.17	0.99 \pm 0.21	4.9 \pm 0.5
$W(e\nu)\gamma$	2889 \pm 36	338 \pm 12	200 \pm 9	33 \pm 4	33 \pm 4	220 \pm 10
$W(e\nu)\bar{t}$	364 \pm 55	259 \pm 41	247 \pm 41	289 \pm 49	5 \pm 5	12 \pm 9
zee	526 \pm 42	192 \pm 27	92 \pm 17	45 \pm 11	0.000000 \pm 0	0.000000 \pm 0
dp	1832 \pm 709	869 \pm 501	265 \pm 249	28 \pm 20	234 \pm 157	478 \pm 41
$t\bar{t}$	50.1 \pm 2.9	12.1 \pm 1.5	9.8 \pm 1.2	8.4 \pm 1.2	0.5 \pm 0.4	454 \pm 409
$t\gamma$	62.2 \pm 1.6	3.1 \pm 0.4	3.7 \pm 0.4	0.35 \pm 0.13	0.67 \pm 0.17	1.3 \pm 0.5
Data driven method						
R	C_B	C_C	C_D	R'	C'_B	C'_D
1.6 \pm 0.5	0.117 \pm 0.004	0.0691 \pm 0.0034	0.0114 \pm 0.0013	0.000000 \pm 0	0.0114 \pm 0.0013	0.0761 ± 0.0035
MC closure and signal leakage parameters						
W+jets	738.0 \pm 65.3	γ +jets	622.6 \pm 114.0	3092.3 \pm 168.4	Signal yield	0.00077 ± 0.00032

A.3 2D Template Fit Method

The 2D template fit method estimates the signal and background yields by applying an unbinned extended maximum likelihood fit simultaneously to the transverse isolation energy ($E_T^{\text{iso}\,1}$, $E_T^{\text{iso}\,2}$) distributions of the two photon candidates. The method was developed for the ATLAS diphoton cross-section measurement [38, 57]. In the following the method is described and the results obtained are summarized. The treatment of the statistical and systematic uncertainties is also provided.

The 2D template fit method is applied in the electron channel inclusive selection. For the exclusive selection, the statistics in the control-regions is too small to perform a stable fit. In this case the fake-photon background is extrapolated from the results of the inclusive measurement. This is discussed at the end of this section.

A.3.1 General Method

The general method is described in Chapter 5.

A.3.2 Template Determination

This is described in Chapter 5.

A.3.3 Signal-Leakage Corrections

The control regions contain a small but non-negligible amount of real photon events. This “signal-leakage” into the fake-photon control regions can be estimated using Monte Carlo simulated samples. The templates obtained from the background control region (F_b , F_{bb}) can be written as a sum of the real- and fake-photon PDFs

$$F_{b,i} = \alpha_i F_{\gamma,i} + (1 - \alpha_i) F_{j,i} \quad i \in \{1, 2\}, \quad (\text{A.10})$$

$$F_{bb} = (1 - \alpha'_1 - \alpha'_2 - \alpha'_3) F_{jj} + \alpha'_1 F_{\gamma,1} F_{j,2} + \alpha'_2 F_{j,1} F_{\gamma,2} + \alpha'_3 F_{\gamma,1} F_{\gamma,2}, \quad (\text{A.11})$$

where α_1 (α_2) is the fraction of $\gamma\gamma$ events in the $\tilde{\mathbf{T}}\mathbf{T}$ ($\mathbf{T}\tilde{\mathbf{T}}$) sample and α'_1 (α'_2 , α'_3) is the fraction of γj ($j\gamma$, $\gamma\gamma$) events in the $\tilde{\mathbf{T}}\tilde{\mathbf{T}}$ sample.

After reordering the different terms of the sum one obtains Equation 5.3 as function of the measured templates $F_{\gamma,\{1,2\}}$, $F_{b,\{1,2\}}$ and F_{bb} :

$$W_{tot}F_{tot} = w_{\gamma\gamma}F_{\gamma,1}F_{\gamma,2} + w_{\gamma j}F_{\gamma,1}F_{b,2} + w_{j\gamma}F_{b,1}F_{\gamma,2} + w_{jj}F_{bb} \quad (\text{A.12})$$

with

$$\begin{aligned} w_{\gamma\gamma} &= W_{\gamma\gamma} \\ &\quad - \frac{\alpha'_3}{1 - \alpha'_1 - \alpha'_2 - \alpha'_3} W_{jj} \\ &\quad - \frac{\alpha_1}{1 - \alpha_1} \left(W_{\gamma j} - \frac{\alpha'_1}{1 - \alpha'_1 - \alpha'_2 - \alpha'_3} W_{jj} \right) \\ &\quad - \frac{\alpha_2}{1 - \alpha_2} \left(W_{j\gamma} - \frac{\alpha'_2}{1 - \alpha'_1 - \alpha'_2 - \alpha'_3} W_{jj} \right) \\ w_{\gamma j} &= \frac{1}{1 - \alpha_1} \left(W_{\gamma j} - \frac{\alpha'_1}{1 - \alpha'_1 - \alpha'_2 - \alpha'_3} W_{jj} \right) \\ w_{j\gamma} &= \frac{1}{1 - \alpha_2} \left(W_{j\gamma} - \frac{\alpha'_2}{1 - \alpha'_1 - \alpha'_2 - \alpha'_3} W_{jj} \right) \\ w_{jj} &= \frac{1}{1 - \alpha'_1 - \alpha'_2 - \alpha'_3} W_{jj} \end{aligned}$$

The fractions of real photon events α can be written as a function of the yields W and by taking the efficiency of the **NON-TIGHT** selection from simulated events

$$\alpha_1 = \frac{N_{\gamma\gamma,MC}^{\tilde{\mathbf{T}}\mathbf{T}}}{N_{\gamma\gamma,MC}^{\mathbf{T}\mathbf{T}}} \frac{W_{\gamma\gamma}}{N_{\gamma\gamma,MC}^{\tilde{\mathbf{T}}\tilde{\mathbf{T}}}} \quad (\text{A.13})$$

$$\alpha_2 = \frac{N_{\gamma\gamma,MC}^{\mathbf{T}\tilde{\mathbf{T}}}}{N_{\gamma\gamma,MC}^{\mathbf{T}\mathbf{T}}} \frac{W_{\gamma\gamma}}{N_{\gamma\gamma,MC}^{\tilde{\mathbf{T}}\tilde{\mathbf{T}}}} \quad (\text{A.14})$$

$$\alpha'_1 = \frac{N_{\gamma j,MC}^{\tilde{\mathbf{T}}\tilde{\mathbf{T}}}}{N_{\gamma j,MC}^{\mathbf{T}\mathbf{T}}} \frac{W_{\gamma j}}{N_{\gamma j,MC}^{\tilde{\mathbf{T}}\tilde{\mathbf{T}}}} \quad (\text{A.15})$$

$$\alpha'_2 = \frac{N_{j\gamma,MC}^{\tilde{\mathbf{T}}\tilde{\mathbf{T}}}}{N_{j\gamma,MC}^{\mathbf{T}\mathbf{T}}} \frac{W_{j\gamma}}{N_{j\gamma,MC}^{\tilde{\mathbf{T}}\tilde{\mathbf{T}}}} \quad (\text{A.16})$$

$$\alpha'_3 = \frac{N_{\gamma\gamma,MC}^{\tilde{\mathbf{T}}\tilde{\mathbf{T}}}}{N_{\gamma\gamma,MC}^{\mathbf{T}\mathbf{T}}} \frac{W_{\gamma\gamma}}{N_{\gamma\gamma,MC}^{\tilde{\mathbf{T}}\tilde{\mathbf{T}}}}. \quad (\text{A.17})$$

Here $N_{ij,MC}^X$ is the number of events of category ij in the sample X measured in Monte Carlo and N^X is the number of events in the sample X measured in the data. Table A.9 summarizes the inputs used for the signal-leakage corrections derived from $W\gamma\gamma$ MC and Table A.10 shows the inputs derived from $W\gamma + \text{jets}$ MC using the inclusive selection. For the first set of inputs the results from **SHERPA** and **ALPGEN** are shown, for the second set only **ALPGEN** was available. The **NON-TIGHT** ratios obtained from different Monte Carlo samples agree within their statistical uncertainties. Table A.11 lists the number of events measured in the control regions using the inclusive and exclusive selection.

Table A.9: Input for the signal leakage correction derived from $W\gamma\gamma$ MC using the inclusive selection. The uncertainties shown are statistical only.

coefficient	NON-TIGHT ratio(electron)	
	SHERPA	ALPGEN
$\frac{N_{\gamma\gamma,MC}^{\tilde{\mathbf{T}}\tilde{\mathbf{T}}}}{N_{\gamma\gamma,MC}^{\mathbf{T}\mathbf{T}}}$	0.036 ± 0.005	0.035 ± 0.004
$\frac{N_{\gamma\gamma,MC}^{\mathbf{T}\mathbf{T}}}{N_{\gamma\gamma,MC}^{\tilde{\mathbf{T}}\tilde{\mathbf{T}}}}$	0.067 ± 0.007	0.064 ± 0.005
$\frac{N_{\gamma\gamma,MC}^{\tilde{\mathbf{T}}\tilde{\mathbf{T}}}}{N_{\gamma\gamma,MC}^{\mathbf{T}\mathbf{T}}}$	0.002 ± 0.001	0.004 ± 0.001

Table A.10: Inputs for Monte Carlo for signal leakage correction derived from $W\gamma + \text{jets}$ MC using the inclusive selection. The uncertainties shown are statistical only.

coefficient	NON-TIGHT ratio
$\frac{N_{\gamma j,MC}^{\tilde{\mathbf{T}}\tilde{\mathbf{T}}}}{N_{\gamma j,MC}^{\mathbf{T}\mathbf{T}}}$	0.009 ± 0.005
$\frac{N_{\gamma j,MC}^{\mathbf{T}\mathbf{T}}}{N_{\gamma j,MC}^{\tilde{\mathbf{T}}\tilde{\mathbf{T}}}}$	0.082 ± 0.036

Table A.11: Number of events in the control regions used for the calculation of the signal-leakage corrections.

control region	number of events
$\tilde{T}T$	22
$T\tilde{T}$	38
$\tilde{T}\tilde{T}$	10

A.3.4 Template Fit Method Results

Template fit method results are shown this section. Analysis of the muon channel performed by collaborators are also given for completeness. The results of the final two-dimensional fit, performed on the 181 events (51 events) in the **TT** sample selected in the muon (electron) channel using the inclusive selection, are shown in Table A.12. The event yields after extrapolating to the signal region are provided as well. Projections of the resulting two-dimensional E_T^{iso} distributions on the transverse isolation energies of the two photon candidates are show in Figure A.1. The results using the 78 events selected in the **TT** sample using the exclusive selection in the muon channel are summarized in Table A.13 and Figure A.2.

Table A.12: Results of the 2D fit method using the inclusive selection. For each category the result of the fit and the event yield is given. The uncertainties are statistical only. Details on how the statistical uncertainties are obtained can be found in Section A.3.5.

Muon Channel (<i>incl.</i>)		Electron Channel (<i>incl.</i>)		
category	yield	yield in signal region	yield	yield in signal region
$\gamma\gamma$	91 ± 16	76 ± 13	39 ± 10	33 ± 8
γj	37 ± 13	17 ± 7	25 ± 8	11 ± 4
$j\gamma$	28 ± 11	11 ± 5	24 ± 8	7 ± 2
jj	20 ± 9	5 ± 3	4 ± 8	1 ± 3

Table A.13: Results of the 2D fit method using the exclusive selection. For each category the result of the fit and the event yield is given. The uncertainties are statistical only. Details on how the statistical uncertainties are obtained can be found in Section A.3.5. The results for the electron channel is extrapolated from the N_{jet} distribution as described in Section A.3.7.

Muon Channel (<i>excl.</i>)		
category	yield	yield in signal region
$\gamma\gamma$	46 ± 11	39 ± 9
γj	18 ± 7	8 ± 4
$j\gamma$	11 ± 7	4 ± 3
jj	10 ± 6	3 ± 2

inclusive selection

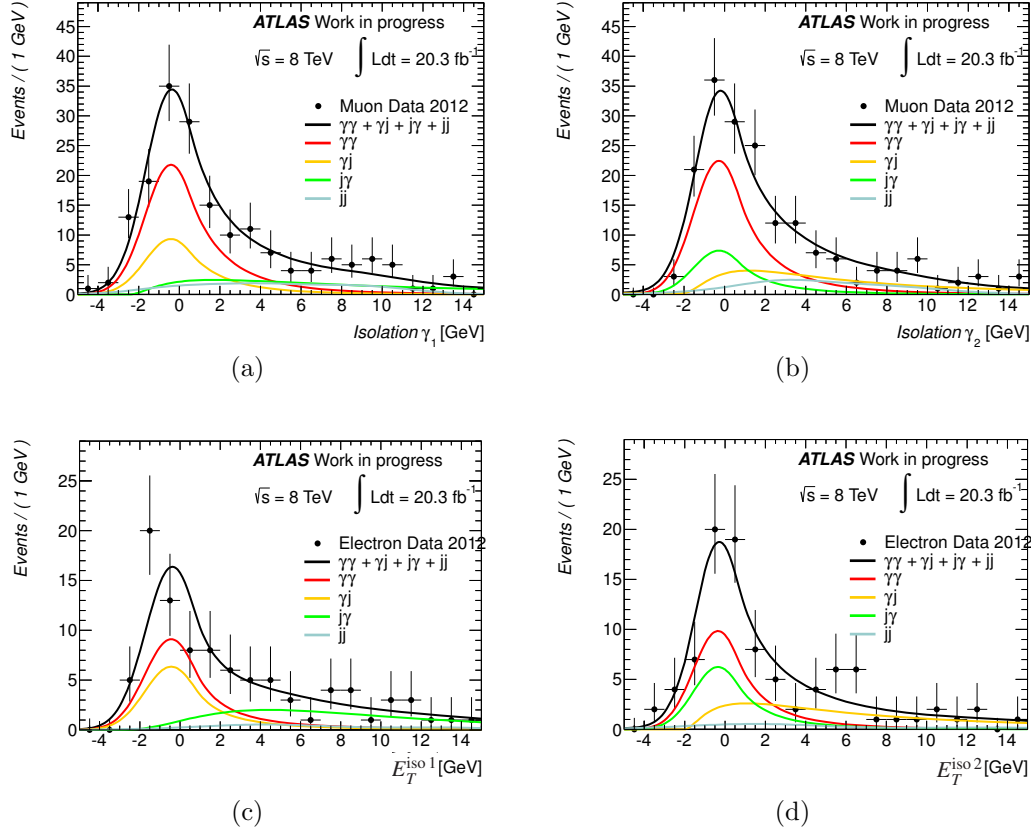


FIGURE A.1: Projection of the two-dimensional isolation distributions on the transverse isolation energy of the leading (left) and subleading (right) photon candidate for the muon channel (top) and the electron channel (bottom). The black dots represent the data selected using the inclusive selection. The black line shows the result of the fit and the colored lines show the different components.

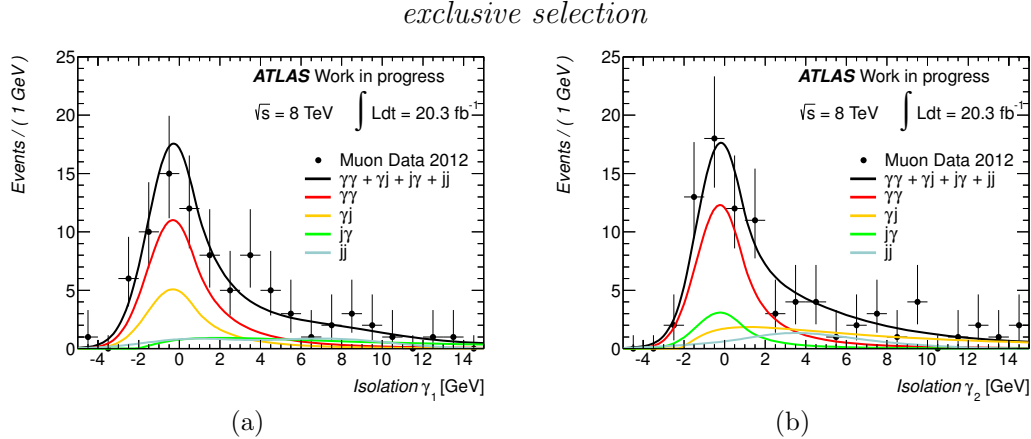


FIGURE A.2: Projection of the two-dimensional isolation distributions on the transverse isolation energy of the leading (left) and subleading (right) photon candidate for the muon channel. The black dots represent the data selected using the exclusive selection. The black line shows the result of the fit and the colored lines show the different components. The results for the electron channel is extrapolated from the N_{jet} distribution as described in Section A.3.7..

A.3.5 Statistical Uncertainties Estimate

The statistical uncertainties on the fit parameters are calculated using **MINOS**. **MINOS** is part of the **MINUIT** software package [41] and estimates the uncertainties for parameter x by finding the points in the parameter space at which the likelihood changes by 0.5. In each iteration the parameter x is kept fixed and all other parameters are minimized before the likelihood is evaluated. The results from **MINOS** are validated with pseudo-experiments. Pseudo-experiments allow to study the biases arising from limited statistics in the data and MC samples.

In the first step, pseudo-data is generated according to the nominal parameterization of the isolation distributions, provided in Equation A.12, with the parameters set to the values obtained from the fit to data, and fluctuated according to a Poisson probability density function.

Each of these pseudo-datasets is fitted with the procedure described in the last section and the event yields with their corresponding uncertainties are extracted. In

addition the pull p_N for each event yield N is computed. The pull is defined as:

$$p_N = \frac{N_{pe} - N_g}{\sigma_{pe}} \quad (\text{A.18})$$

where N_g is the value used in the generation of pseudo-experiment and $N_{pe} \pm \sigma_{pe}$ is the fit result obtained. The pulls are expected to be distributed as a standard Gaussian with mean value equal to zero and width equal to one, provided that the uncertainty σ_{pe} is correctly estimated.

Any deviation from the standard Gaussian pull distribution is taken as an additional uncertainty. If the mean of the pull distribution is shifted from zero, the resulting uncertainty σ_{bias} is calculated as

$$\sigma_{bias} = \mu_{pull} \times \sigma_{fit}, \quad (\text{A.19})$$

where μ_{pull} is the mean of the pull distribution and σ_{fit} is the uncertainty of the fit as given by **MINOS**. If the width of the pull distribution is different from one the uncertainty of the fit is corrected by:

$$\sigma_{width} = \sigma_{pull} \times \sigma_{fit}, \quad (\text{A.20})$$

where σ_{pull} is the width of the pull distribution and σ_{fit} is the same as above. The total uncertainty on the event yield N is the quadratic sum of the two terms:

$$\sigma_N = \sqrt{\sigma_{bias}^2 + \sigma_{width}^2} \quad (\text{A.21})$$

Figure A.3 shows the pull distribution of the event yields in the signal region after generating 10000 pseudo-experiments. The distributions are fitted with a Gaussian with mean μ and width σ whose values are shown in the figure. For all these distributions the width of the gaussian is compatible with one within uncertainties, although they show a small bias towards negative values.

The three background components γj , $j\gamma$ and jj show non-gaussian tails towards negative values. This behaviour comes from the small statistics available in the control regions. This has been verified by performing the same test generating fifty times more events in each dataset.

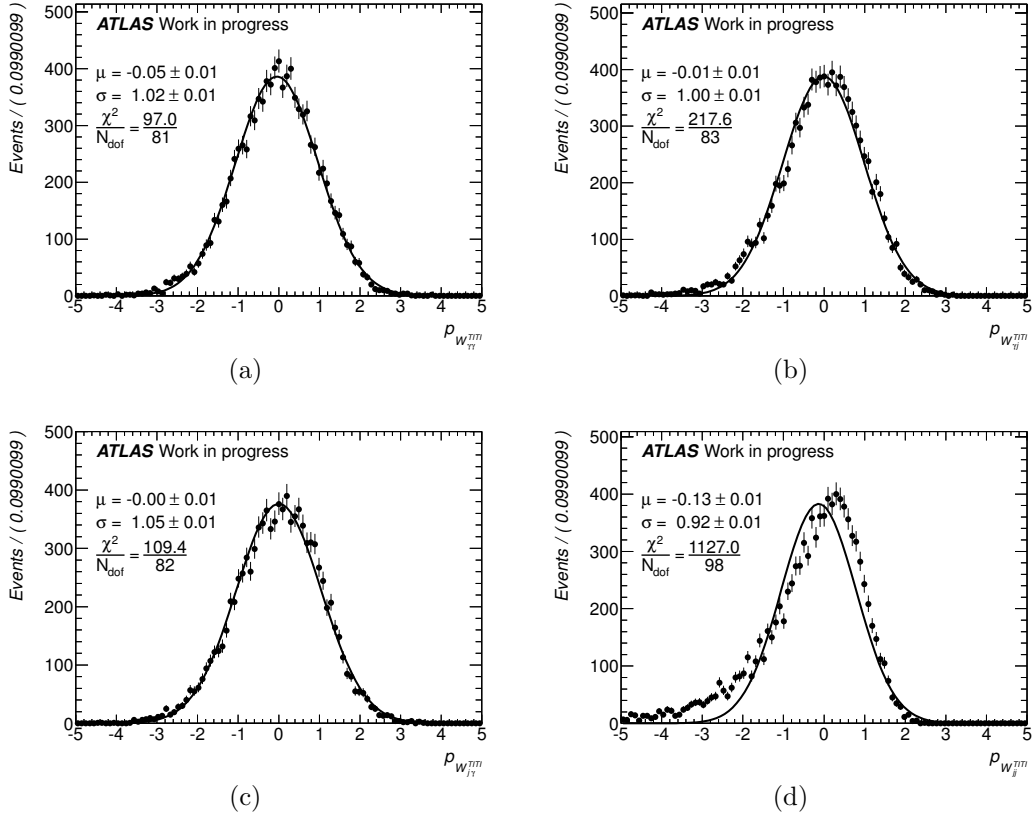


FIGURE A.3: Pull distributions for the four event yields in the signal region from 10000 pseudo-experiments. In addition the mean, width and goodness-of-fit of a gaussian fitted to these distributions is shown.

In order to account for the non-Gaussian behaviour the pull distribution is fitted again within $\pm 2\sigma$ if the probability of the first fit describing the distribution is below 5%. Then the larger mean and width of the two fits is taken for the uncertainty calculation as described above. The resulting statistical uncertainties are summarized in Table 5.1.

A.3.6 Systematic Uncertainties Estimate

The main systematic uncertainties arise from the modeling of the fake-photon templates, and in particular from the following effects:

- limited statistics in the control regions;
- functional form used for modeling the background distribution;
- definition of the control regions;
- dependance on Monte Carlo generator;
- statistical uncertainty on signal leakage.

The effect of each source of the systematic uncertainty is evaluated using pseudo-experiments, as described in Section A.3.5. Each systematic uncertainty is described in the following, with the pull distributions shown for the first systematic source as an illustration.

Limited Control Regions Statistics

This uncertainty arises from the imperfect knowledge of the templates due to the limited statistics in the control regions as well as in the Monte Carlo samples. In order to estimate it, a set of alternate templates \mathbb{T} compatible with the data in the control regions is generated. In a second step pseudo-data generated using the nominal templates is fitted using the templates from the set of alternate templates.

The corresponding pull distributions are shown in Figure A.4.

Background Model

The choice of the functional form of the fake-photon template F_b is arbitrary, therefore the related systematic uncertainty needs to be estimated. This uncertainty

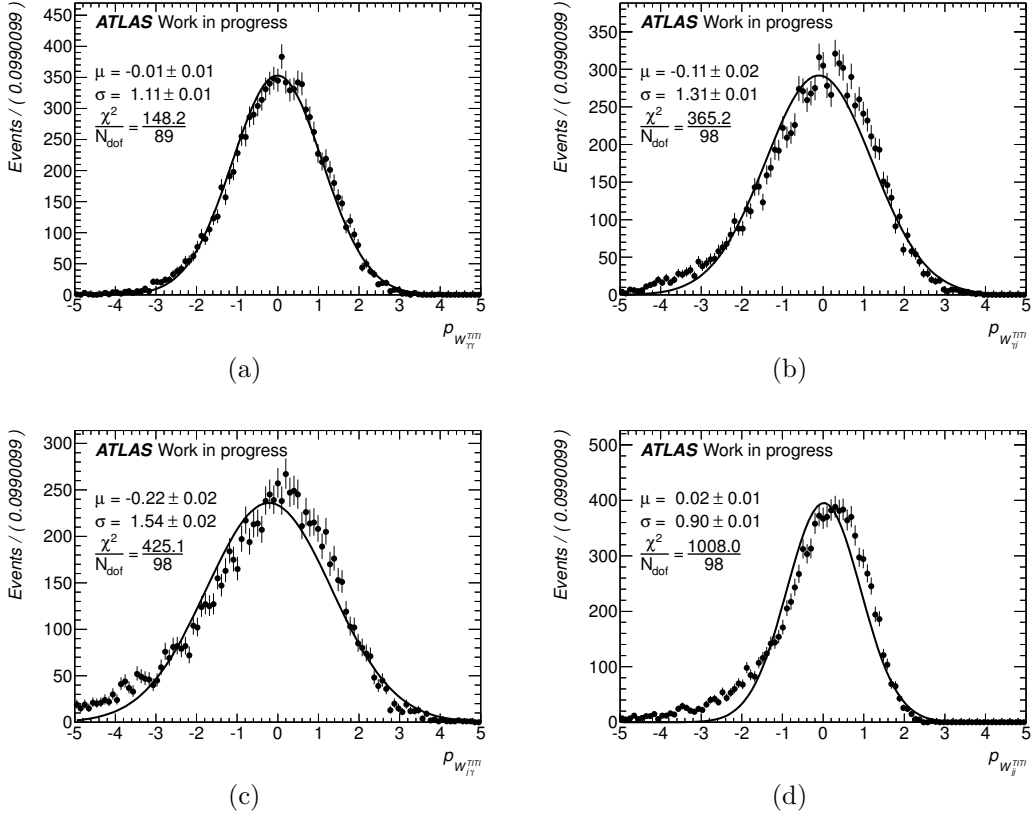


FIGURE A.4: Pull distributions from pseudo-experiments used to evaluate the systematic uncertainty due to limited control region statistics. The results are shown for the muon (a–d) and electron (e–h) channel using the inclusive selection.

is evaluated by using templates with a different functional form to fit the pseudo-datasets generated using the nominal choice. The two alternate functions considered are a Crystal-Ball line-shape and a Novosibirsk function.

Selection of the Control Regions

The definition of the **NON-TIGHT** photon selection may influence the fake-photon templates F_b and F_{bb} . In order to estimate the impact of this choice, two alternate **NON-TIGHT** definition have been tested. The first differs from the nominal definition in that it only relaxes cuts on three instead of four strip variables ($L'3$). The second one relaxes all five strip variables ($L'5$). To evaluate the uncertainty associated

with the control region definition, the pseudo-data is generated using the alternate definitions and are fitted to the nominal model.

Monte Carlo Generator Dependence

Since the real-photon templates are taken from Monte Carlo, the effect of the generator used to obtain the templates has to be tested. The pseudo-data for this test is generated using the templates obtained from events simulated with **ALPGEN**. This also takes into account differences in the description of the signal leakage parameters shown in Table A.9.

Signal Leakage Inputs

The parameters used to correct the leakage of real photons in the fake-photon control region have associated uncertainties. The events in the control regions $N^{\tilde{\mathbf{T}}\mathbf{T}}$, $N^{\mathbf{T}\tilde{\mathbf{T}}}$ and $N^{\tilde{\mathbf{T}}\tilde{\mathbf{T}}}$ and the leakage parameters α are subject to statistical fluctuations. In addition the systematic uncertainty on the photon identification efficiency are taken into account.

Systematic Uncertainties Results

The systematic uncertainties on the event yields in the signal region are given in Table A.14.

Table A.14: Systematic uncertainties for the electron channel using the inclusive selection.

source	$N_{\gamma\gamma}$	$N_{\gamma j}$	$N_{j\gamma}$	N_{jj}
Control Region Statistics	± 3.9 ($\pm 12\%$)	± 4.5 ($\pm 41\%$)	± 6 ($\pm 86\%$)	± 0.26 ($\pm 26\%$)
Background Model G+N	± 0.41 ($\pm 1.2\%$)	± 0.3 ($\pm 2.8\%$)	± 0.34 ($\pm 4.9\%$)	± 0.049 ($\pm 4.8\%$)
Background Model CB	± 0.58 ($\pm 1.7\%$)	± 0.82 ($\pm 7.5\%$)	± 1.7 ($\pm 24\%$)	± 0.33 ($\pm 33\%$)
Antitight Definition $L'5$	± 0.12 ($\pm 0.36\%$)	± 0.8 ($\pm 7.3\%$)	± 0.47 ($\pm 6.7\%$)	± 0.43 ($\pm 43\%$)
Antitight Definition $L'3^1$	— —	— —	— —	— —
MC Generator	± 0.073 ($\pm 0.22\%$)	± 1.1 ($\pm 10\%$)	± 0.033 ($\pm 0.47\%$)	± 0.13 ($\pm 13\%$)
Signal Leakage Inputs	± 1 ($\pm 3\%$)	± 1.4 ($\pm 13\%$)	± 0.053 ($\pm 0.76\%$)	± 0.081 ($\pm 8.1\%$)
total	± 4.1 ($\pm 12\%$)	± 5 ($\pm 46\%$)	± 6.3 ($\pm 90\%$)	± 0.62 ($\pm 62\%$)

A.3.7 Background Extrapolation for the Exclusive Selection in the Electron Channel

As explained earlier, the number of events available in the control regions for the exclusive selection in the electron channel is too small to apply the method outlined above. Therefore the fake-photon background has to be determined differently in this case. It is extrapolated from the inclusive measurement using the zeroth bin of the N_{jet} distribution. The extrapolation is done separately for each background event category, i.e. for γj -, $j\gamma$ - and jj -events, by using the N_{jet} distribution obtained from the corresponding control region. From these distributions the fraction of events in the zero-jet bin, f_0^{CR} , is determined and multiplied with the results of the 2D template fit method in each category given in Table A.12.

Table A.15: The result of the fake-photon background estimation using the exclusive selection in the electron channel. For each background category the estimated number of events and its statistical and systematic uncertainty is given. The numbers are obtained by using the zero-jet bin of the N_{jet} distribution obtained from data (see text).

Electron Channel (<i>excl.</i>)	
category	yield in signal region
γj	$5 \pm 2 \text{ (stat.)} \pm 2 \text{ (syst.)}$
$j\gamma$	$2 \pm 1 \text{ (stat.)} \pm 2 \text{ (syst.)}$
jj	$0.3 \pm 0.6 \text{ (stat.)} \pm 0.4 \text{ (syst.)}$

The systematic uncertainty on the number of fake-photon events obtained using the background extrapolation can be split into two categories : the normalization uncertainty on the total event yield for each of the event categories, and the shape uncertainty on the N_{jet} distribution used for the extrapolation. The first one is the systematic uncertainty on the results of the template fit method, obtained from the inclusive selection in the electron channel as described above and summarized in Table A.14. The latter is determined in the following way. The fraction of events in the zero-jet bin calculated by using the background dominated control region is compared to the number obtained when using MC. The difference is taken as a systematic uncertainty and added in quadrature to the normalization uncertainty. The result of the fake-photon background estimation is given in Table A.15 for the three background event categories.

Appendix B

More on the interpretation of the measured $pp \rightarrow W\gamma\gamma + X$ results

B.1 Correction factors

The systematic uncertainties are summarized in Table B.1 and B.2. Details on the treatment of the statistical and systematic uncertainties are given in Section B.1.1 and B.1.2.

B.1.1 Statistical Uncertainty of the Correction Factor

As the number of events selected by the nominal event selection, N_{reco} , and the number of events in the restricted/measured fiducial region, $N_{truth, restr\ fid}$, are dependent on each other, one can write the definition of the efficiency in the following way in order to calculate its statistical error.

$$C = \frac{N_{reco}}{N_{truth, restr\ fid}} = \frac{r + b}{t + b}, \quad (\text{B.1})$$

here, r (t) stands for the number of events that have been selected by the nominal measured (restricted fiducial) event selection only and b denotes the events which

Table B.1: Correction factor for the inclusive and the exclusive selection along with their statistical and relative systematic uncertainty in the muon channel.

	Inclusive Selection	Exclusive Selection
Correction Factor ϵ	$(41.64 \pm 0.71 \text{ (stat.)}) \%$	$(40.62 \pm 1.05 \text{ (stat.)}) \%$
Acceptance A	$(89.23 \pm 0.31 \text{ (stat.)}) \%$	$(89.72 \pm 0.44 \text{ (stat.)}) \%$
Efficiency C	$(46.66 \pm 0.78 \text{ (stat.)}) \%$	$(45.28 \pm 1.15 \text{ (stat.)}) \%$
Relative systematic error on the efficiency σ_ϵ [%]		
Muon Eff Scale Factor	0.01	0.01
Muon Energy Scale	0.16	0.17
Muon Isolation Eff.	0.19	0.14
Muon Resolution ID	0.07	0.09
Muon Resolution MS	2.25	1.48
Photon Energy Scale	1.00	1.21
Photon Energy Resol.	0.26	0.80
Photon ID Efficiency	1.41	1.58
MET Reso Soft Terms	0.42	0.62
MET Scale Soft Terms	0.80	0.97
Jet Energy Scale	0.67	3.73
Jet Energy Resolution	0.04	1.83
Jet Vertex Fraction	—	0.36
Pileup reweight	0.11	0.31
Trigger	0.52	0.52
Total rel. syst. error on ϵ [%]	3.12	5.09
Rel. deviation to ALPGEN of ϵ [%]	0.6	0.6

Table B.2: Correction factor for the inclusive and the exclusive selection along with their statistical and relative systematic uncertainty in the electron channel.

	Inclusive Selection	Exclusive Selection
Correction Factor ϵ	$(20.40 \pm 0.53 \text{ (stat.)}) \%$	$(15.50 \pm 0.67 \text{ (stat.)}) \%$
Acceptance A	$(82.46 \pm 0.39 \text{ (stat.)}) \%$	$(82.46 \pm 0.56 \text{ (stat.)}) \%$
Efficiency C	$(24.75 \pm 0.63 \text{ (stat.)}) \%$	$(18.80 \pm 0.81 \text{ (stat.)}) \%$
Relative systematic error on the efficiency σ_ϵ [%]		
Electron Reconstruction Eff.	0.10	0.08
Electron ID Uncert	0.24	0.22
Electron Isolation Eff.	0.04	0.04
EM Energy Scale	2.46	4.48
EM Energy Resolution	0.51	0.92
Photon ID Eff	1.62	1.69
MET Reso Soft Terms	0.61	1.14
MET Scale Soft Terms	0.48	1.31
Jet Energy Resol	0.08	2.21
Jet Energy Scale	1.07	5.11
Jet Vertex Fraction	—	0.51
Pileup Reweighting	0.08	0.16
Trigger	0.66	0.66
Total rel. syst. error on ϵ [%]	3.35	7.65
Rel. deviation to ALPGEN of ϵ [%]	6.1	0.6

pass the requirements of both selections. In this notation the subsets of events, r , t and b , are not correlated and the Gaussian laws of error propagation apply. Therefore the statistical error on C is given by:

$$\sigma_C = \frac{1}{(t+b)^2} \sqrt{(\sigma_t(r+b))^2 + (\sigma_r(t+b))^2 + (\sigma_b(t-r))^2}, \quad (\text{B.2})$$

where σ_i denotes the statistical error of the respective quantity. The statistical error on acceptance A is treated with the same procedure.

B.1.2 Systematic Uncertainty on Correction Factors

The uncertainties on the momenta or efficiencies of the objects in the final state contribute to the uncertainty on the analysis efficiency C . Using the procedure introduced in Chapter 6, the uncertainties due to these sources can be computed by varying the efficiency or momenta by one up or down one sigma variation, and combined in quadruple for independent sources. The different systematic sources in the electron channel are described as following.

Photon related uncertainties

Photon Energy Scale

An energy scale correction is applied to correct for the discrepancy between the electromagnetic response of the detector and simulation. It is defined as $E_{data} = (1 + a_{Nom})E_{mc}$. The correction has a set of systematic uncertainties δa , which are determined by independent measurement of the energy scale with data driven methods. These uncertainties are usually symmetric, so they are varied independently and the variations are summed quadratically as the total uncertainty. The correction and uncertainty is propagated to the measurement by dividing the measured energy by the factor $(1 + a_{Nom})$ where a_{Nom} is the central value of the correction. Differences between systematic uncertainty variations and the nominal correction,

$\delta a = a_{Var} - a_{Nom}$ are applied to the MC: $E_{Var} = E_{mc}(1 + \delta a)$.

Photon Energy Resolution

The energy resolution uncertainties are related to the smearing of the photon energies, and are obtained with the resolution correction being varied up or down.

Photon Identification (ID) and Isolation Efficiency

The electromagnetic shower shapes of the simulated photons are corrected by the so called fudge-factors. These are correction factors computed by comparing all shower shapes observed in 2012 data and Monte Carlo simulated samples. The systematic uncertainties also cover the difference in photon isolation distributions in data and MC.

As this analysis is studying a final state containing two photons, the photon ID uncertainty needs to account for the correlations between two photons. The uncertainty is calculated as $\delta_{ID} = \sqrt{\delta_1^2 + \delta_2^2 + 2C_{1,2}\delta_1\delta_2}$, where δ_i is the photon ID uncertainty of photon i and $C_{1,2}$ the correlation factor of the two photons. Two photons in the same eta range with the same conversion category (converted or unconverted), are considered to be fully correlated. More information about the photon ID efficiency can be found at [36].

Electron related uncertainties

Electron Energy Scale and Resolution

The uncertainties on the energy scale and resolution of the electron are obtained in the same way as for photons. The impact of the photon and electron energy scale uncertainty on the electron channel correction factor is studied simultaneously, as electrons and photons are both detected by the electromagnetic shower in the calorimeter of ATLAS.

Electron Identification (ID) Efficiency

The difference between the electron ID efficiency computed in data with tag and probe method, and from Monte Carlo simulated samples is corrected by a scale factor on the efficiency value.

Electron Reconstruction Efficiency

The electron reconstruction scale factors are computed the same way as for ID efficiency. More details are documented in [28].

Electron Isolation and Impact Parameter Efficiency

The difference between MC and data introduced by the cut on the electron isolation and impact parameter is corrected for by applying scale factors.

Jet related uncertainties

Jet Energy Scale and Resolution

The jet energy scale uncertainty is evaluated based on Monte-Carlo studies and in situ measurements [58]. The impact of jet energy scale uncertainty (JES) to the signal efficiency is estimated by varying a set of 17 components of the JES uncertainty individually by one sigma (up and down) for each jet in the event. The resulting uncertainties on the correction factor are then added in quadrature and quoted as JES uncertainty.

Jet Vertex Fraction

The Jet Vertex Fraction (or JVF) is a measure for the probability of a jet to originate from a hard scattering vertex. It helps to suppress contributions from jets that originate from the underlying event or from pile-up. The uncertainty due to this requirement is also evaluated.

Event related uncertainties

Missing transverse Energy

The missing transverse Energy (E_T^{miss}) is calculated from the sum of all energy deposits in the calorimeters. Therefore, the modifications of the object energies need to be propagated to the E_T^{miss} observable. This is done by recalculating E_T^{miss} taking the different energy scale and resolution variation of the objects into account. Uncertainties arising from the energy clusters that do not match to any objects are also considered, as these energies are also subject to scale and resolution uncertainties. More details can be found in described in [59].

Pileup

The pileup (multiple proton-proton interactions in the same bunch crossing) simulated in Monte Carlo deviate from what is observed in data. Therefore, the events of the simulated samples are weighted in order to correct for this fact. The average number of interactions $\langle \mu \rangle$ in data taken in 2012 is a factor of 1.09 larger than Monte Carlo simulations. The uncertainty on this factor is conservatively assumed to be ± 0.4 and propagated to the signal efficiency by modifying the event weights accordingly.

B.1.3 Statistical error on the systematic uncertainty

For each systematic component, the corresponding statistical error σ_{σ_C} is evaluated and quoted instead of the systematic uncertainty σ_C itself, if it exceeds the former. In order to estimate the statistical error of a systematic component, it is helpful to split the number of events N_{sys} that are accepted by the event selection on the systematically modified data set according to:

$$N_{\text{sys}} = N_{\text{nom}} + N_{\text{in}} - N_{\text{out}}. \quad (\text{B.3})$$

N_{nom} denotes the number of events, that are selected by the event selection on the unmodified (nominal) data set and N_{in} (N_{out}) is the event count of events that migrate into (out of) the signal region due to the systematic variation of the data set. Note, that N_{in} and N_{out} stand for different event subsets, i.e. events that are not correlated. The relative systematic error on the efficiency estimation can be rewritten to

$$\sigma_C = \frac{C_{sys} - C_{nom}}{C_{nom}} = \frac{N_{nom} - N_{sys}}{N_{nom}} = \frac{N_{in} - N_{out}}{N_{nom}} = \frac{N_{io}}{N_{nom}} \quad (B.4)$$

and Gaussian error propagation applies. Therefore one finds:

$$\sigma_{\sigma_C} = \sigma_C \times \sqrt{\left(\frac{\sigma_{N_{io}}}{N_{io}}\right)^2 + \left(\frac{\sigma_{N_{nom}}}{N_{nom}}\right)^2}. \quad (B.5)$$

The corresponding results can be found in Table B.1 and 6.2.

B.2 aQGC analysis

B.2.1 aQGC region optimization

Since aQGC signals enhance the production rate in high $M_{\gamma\gamma}$ region, the cut to achieve the best sensitivity of aQGC limits is studied. tail of the diphoton invariant mass distribution. Furthermore, the diphoton invariant mass can be sensitive to resonance signals from new particles. The limits on f_{M2} and f_{M3} are computed for different $M_{\gamma\gamma}$ cut. $M_{\gamma\gamma} > 300\text{GeV}$ is chosen to define the phase space used for aQGC studies.

B.2.2 Correction Factor for different aQGC scenarios

Since it is not obvious that the correction factors obtained for the phase space used for cross section computation apply for the aQGC region, they are computed with simulated samples generated by Madgraph with the following aQGC parameters (in units GeV^{-4}):

Table B.3: Expected 95% CL limits on f_{M2} and f_{M3} using different signal regions defined by lower diphoton invariant mass ($M_{\gamma\gamma}$) cuts. The numbers in parentheses are the lower and upper limits. The limits converge to minimum values starting from 300 GeV.

$M_{\gamma\gamma}$ cut (GeV)	$f_{M2} \times 10^{-8}$ (GeV $^{-4}$)	$f_{M3} \times 10^{-8}$ (GeV $^{-4}$)
0	[-32.3, 33.4]	[-53.3, 52.2]
200	[-14.2, 14.5]	[-23.8, 23.1]
240	[-12.6, 12.9]	[-21.8, 20.9]
300	[-11.8, 12.0]	[-20.2, 19.4]
360	[-11.0, 11.1]	[-19.0, 18.2]
400	[-11.1, 11.3]	[-18.5, 18.0]

- $f_{M2} = 3 \times 10^{-10}$
- $f_{M3} = 5 \times 10^{-10}$ and
- $f_{T0} = 2 \times 10^{-11}$.

The central values of the correction factors for the different Monte Carlo samples are given in tables B.4 and B.5 for the electron and muon channel. These values agree with those for cross section measurement within uncertainties. Therefore it is valid to assume the correction factors are independent of the aQGC coupling scenarios nor the $M_{\gamma\gamma}$ region.

Table B.4: Correction factor $A \times C$ for the inclusive and the exclusive electron selection for different points in the (aQGC) phase space.

	Inclusive Selection [%]	Exclusive Selection [%]
SM	20.40	15.50
f_{M2}	22.15	19.22
f_{M3}	22.55	19.64
f_{T0}	22.18	18.92

Table B.5: Correction factor $A \times C$ for the inclusive and the exclusive muon selection for different points in the (aQGC) phase space.

	Inclusive Selection [%]	Exclusive Selection [%]
SM	41.64	40.62
f_{M2}	44.69	42.71
f_{M3}	44.32	42.02
f_{T0}	44.94	42.63

Appendix C

TRT aging monitoring plots

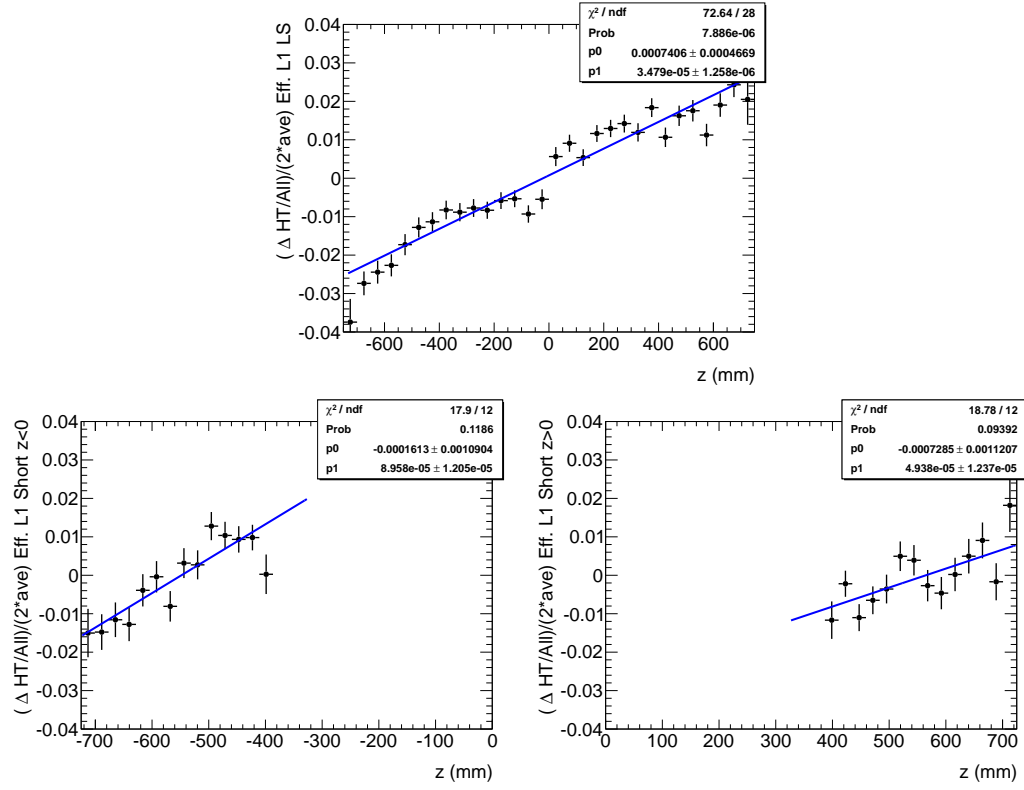


FIGURE C.1: The relative change $(\Delta HT_{ratio} / (2 \times \text{ave } HT_{ratio}))$ for Period E 2012 Data for long straws(up), short straws $z < 0$ (down left) and $z > 0$ (down right) in layer 1.

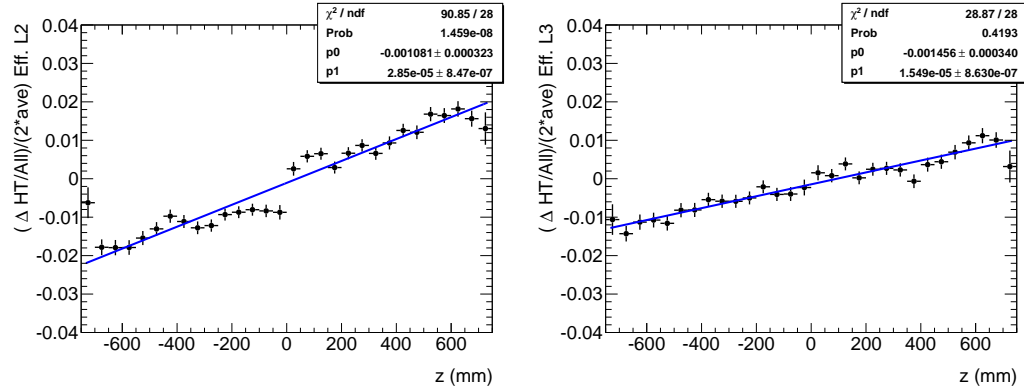


FIGURE C.2: The relative change $(\Delta HT_{ratio} / (2 \times \text{ave } HT_{ratio}))$ for Period E 2012 Data for layer 2 and 3 in Barrel.

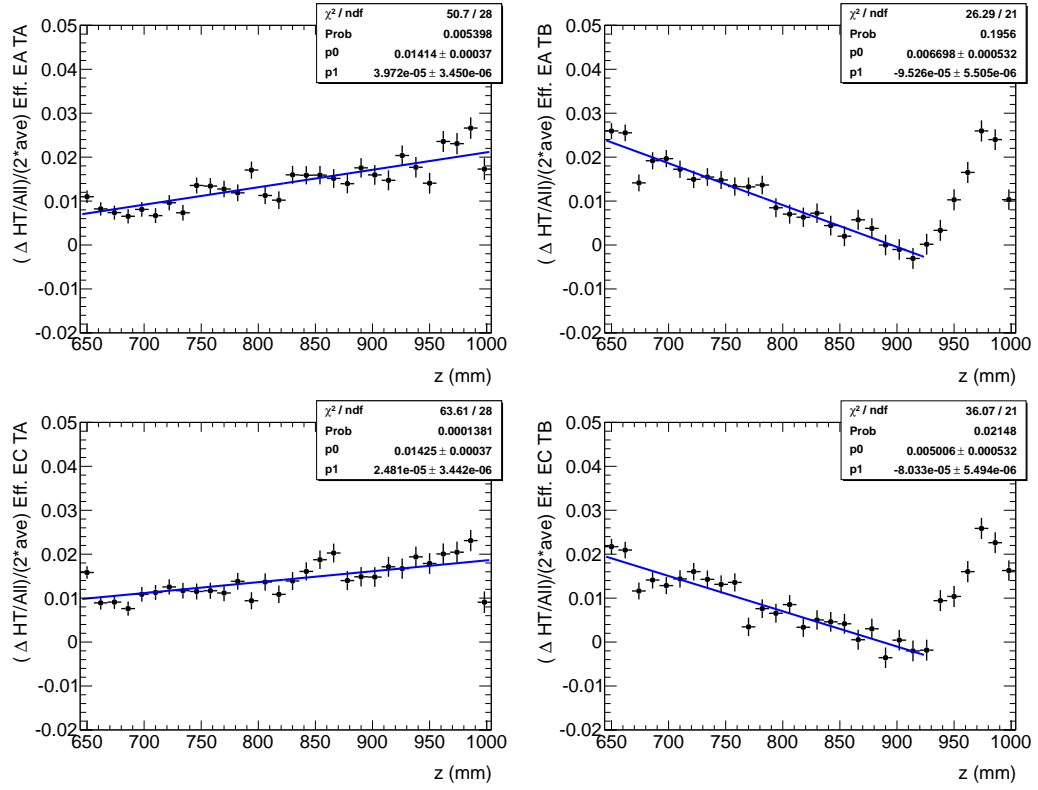


FIGURE C.3: $\Delta HT_{ratio} / (2 \times \text{average } HT_{ratio})$ for Period E 2012 Data in end-cap A. The left plot is for type-A wheels and the right plot is for type-B wheels.

Appendix D

Event selection table for $W\gamma\gamma$ analysis

Table D.1: The number of events after each selection step for the electron channel is shown. This is performed on a data set collected from period B, corresponding to an integrated luminosity of 5.3 fb^{-1} . A filtered sample is used. It is a subset of the whole dataset which has 116070903 events in total.

All Events	1316788.0
Cut1: GRL	1272370.0
Cut2:npv	1271820.0
Cut3: trigger	31586.0
Cut 3a: Good event (data only), LAr and Tile errors	31526.0
Cut4: \geq good electron	12178.0
Cut5: Second electron veto	6503.0
Cut6: MET $>25\text{GeV}$	3611.0
Cut7: Mt $>40\text{GeV}$	2475.0
Cut 8: No jets (off for now)	2475.0
Cut 9: Clean MET	2401.0
Cut 10: ≥ 1 tight isolated photon with $\text{pt} > 20\text{GeV}$	563.0
Cut 11: ≥ 2 tight isolated photon $\text{pT} > 20 \text{ GeV}$	44.0
Cut 12: Z rejection cuts	7.0

Bibliography

- [1] U. Baur, T. Han, N. Kauer, R. Sobey, and D. Zeppenfeld, *$W\gamma\gamma$ production at the Fermilab Tevatron collider: Gauge invariance and radiation amplitude zero*, Phys.Rev. **D56** (1997) 140–150, [arXiv:hep-ph/9702364](https://arxiv.org/abs/hep-ph/9702364) [hep-ph].
- [2] G. Bozzi, F. Campanario, M. Rauch, and D. Zeppenfeld, *$W^{+-}\gamma\gamma$ production with leptonic decays at NLO QCD*, Phys.Rev. **D83** (2011) 114035, [arXiv:1103.4613](https://arxiv.org/abs/1103.4613) [hep-ph].
- [3] J. Beringer et al., *Particle Data Group*, Phys. Rev. D **86** (2012).
- [4] P. W. Higgs, *Broken Symmetries and the Masses of Gauge Bosons*, Phys. Rev. Lett. **13** (Oct, 1964) 508–509.
<http://link.aps.org/doi/10.1103/PhysRevLett.13.508>.
- [5] *Observation of a new boson at a mass of 125 GeV with the {CMS} experiment at the {LHC}*, Physics Letters B **716** (2012) no. 1, 30 – 61. <http://www.sciencedirect.com/science/article/pii/S0370269312008581>.
- [6] the ATLAS collaboration., *Observation of a new particle in the search for the Standard Model Higgs boson with the {ATLAS} detector at the {LHC}*, Physics Letters B **716** (2012) no. 1, 1 – 29. <http://www.sciencedirect.com/science/article/pii/S037026931200857X>.
- [7] R. E. Taylor, *Inelastic electron-Nucleon Scattering Experiments*, .
- [8] F. Abe, H. Akimoto, A. Akopian, M. G. Albrow, S. R. Amendolia, D. Amidei, J. Antos, C. Anway-Wiese, S. Aota, G. Apollinari, and et al., *Observation of Top Quark Production in pp Collisions with the Collider Detector at Fermilab*, Physical Review Letters **74** (Apr., 1995) 2626–2631, [hep-ex/9503002](https://arxiv.org/abs/hep-ex/9503002).
- [9] S. Abachi, B. Abbott, M. Abolins, B. S. Acharya, I. Adam, D. L. Adams, M. Adams, S. Ahn, H. Aihara, G. Álvarez, and et al., *Search for High Mass Top Quark Production in pp Collisions at $s = 1.8$ TeV*, Physical Review Letters **74** (Mar., 1995) 2422–2426, [hep-ex/9411001](https://arxiv.org/abs/hep-ex/9411001).

[10] DONUT Collaboration, K. Kodama, N. Ushida, C. Andreopoulos, N. Saoulidou, G. Tzanakos, P. Yager, B. Baller, D. Boehnlein, W. Freeman, B. Lundberg, J. Morfin, R. Rameika, J. C. Yun, J. S. Song, C. S. Yoon, S. H. Chung, P. Berghaus, M. Kubantsev, N. W. Reay, R. Sidwell, N. Stanton, S. Yoshida, S. Aoki, T. Hara, J. T. Rhee, D. Ciampa, C. Erickson, M. Graham, K. Heller, R. Rusack, R. Schwienhorst, J. Sielaff, J. Trammell, J. Wilcox, K. Hoshino, H. Jiko, M. Miyanishi, M. Komatsu, M. Nakamura, T. Nakano, K. Niwa, N. Nonaka, K. Okada, O. Sato, T. Akdogan, V. Paolone, C. Rosenfeld, A. Kulik, T. Kafka, W. Oliver, T. Patzak, and J. Schneps, *Observation of tau neutrino interactions*, Physics Letters B **504** (Apr., 2001) 218–224, [hep-ex/0012035](#).

[11] F. Halzen and A. D. Martin, *QUARKS AND LEPTONS: AN INTRODUCTORY COURSE IN MODERN PARTICLE PHYSICS*. Wiley, New York, USA, 1984.

[12] T. Barklow, U. Baur, F. Cuypers, S. Dawson, D. Errede, et al., *Anomalous gauge boson couplings*, eConf **C960625** (1996) STC127, [arXiv:hep-ph/9611454](#) [hep-ph].

[13] C. Degrande, N. Greiner, W. Kilian, O. Mattelaer, H. Mebane, et al., *Effective Field Theory: A Modern Approach to Anomalous Couplings*, Annals Phys. **335** (2013) 21–32, [arXiv:1205.4231](#) [hep-ph].

[14] S. M. L. O. J. P. Eboli, M. C. Gonzalez-Garcia Phys Rev D69 (2004) 095005.

[15] O. Eboli, M. Gonzalez-Garcia, and J. Mizukoshi, *$p p \rightarrow gt; j j e+- mu+- nu nu$ and $j j e+- mu-+ nu nu$ at $O(\alpha(em)^{**6})$ and $O(\alpha(em)^{**4} \alpha(s)^{**2})$ for the study of the quartic electroweak gauge boson vertex at CERN LHC*, Phys.Rev. **D74** (2006) 073005, [arXiv:hep-ph/0606118](#) [hep-ph].

[16] A. Alboteanu, W. Kilian, and J. Reuter, *Resonances and Unitarity in Weak Boson Scattering at the LHC*, JHEP **0811** (2008) 010, [arXiv:0806.4145](#) [hep-ph].

[17] J. K. M. O. J. P. Eboli, M. C. Gonzalez-Garcia Phys Rev D74 (2006) 073005.

[18] ATLAS Collaboration Phys. Rev. D **87** (2013) 112003.

[19] CMS Collaboration CERN-PH-EP-2013-108 (submitted to Phys. Rev. D) (2013) .

[20] ATLAS Collaboration Collaboration, G. Aad et al., *Search for diphoton events with large missing transverse momentum in 7 TeV proton-proton collision data with the ATLAS detector*, Phys.Lett. **B718** (2012) 411–430, [arXiv:1209.0753](https://arxiv.org/abs/1209.0753) [hep-ex].

[21] CMS Collaboration Collaboration, S. Chatrchyan et al., *A search for WW gamma and WZ gamma production and constraints on anomalous quartic gauge couplings in pp collisions at $\sqrt{s} = 8$ TeV*, Phys.Rev. **D90** (2014) 032008, [arXiv:1404.4619](https://arxiv.org/abs/1404.4619) [hep-ex].

[22] M. L. Mangano, M. Moretti, F. Piccinini, R. Pittau, A. Polosaalpgen JHEP **0307** (2003) 001.

[23] G. Corcella et al. JHEP **0101** (2001) 010.

[24] T. Gleisberg et al. JHEP **0902** (2009) 007.

[25] J. M. Campbell and R. Ellis, *MCFM for the Tevatron and the LHC*, Nucl.Phys.Proc.Suppl. **205-206** (2010) 10–15, [arXiv:1007.3492](https://arxiv.org/abs/1007.3492) [hep-ph].

[26] K. Arnold *et al.* Comput. Phys. Commun. **180** (2009) 1661–1670, [arXiv:0811.4559](https://arxiv.org/abs/0811.4559) [hep-ph].

[27] ATLAS Collaboration, G. Aad et al., *The ATLAS Experiment at the CERN Large Hadron Collider, Chapter 4*, JINST **3** (2008) S08003.

[28] ATLAS Collaboration, *Electron efficiency measurements with the ATLAS detector using the 2012 LHC proton-proton collision data*, ATLAS-CONF-2014-032.

[29] *Letter of Intent for the Phase-I Upgrade of the ATLAS Experiment*, Tech. Rep. CERN-LHCC-2011-012. LHCC-I-020, CERN, Geneva, Nov, 2011.

[30] C. ATLAS, *Letter of Intent for the Phase-II Upgrade of the ATLAS Experiment*, Tech. Rep. CERN-LHCC-2012-022. LHCC-I-023, CERN, Geneva, Dec, 2012. Draft version for comments.

[31] M. Capeans, F. Anghinolfi, S. Baron, L. Cardiel-Sas, A. Catinaccio, et al., *Recent aging studies for the ATLAS transition radiation tracker*, IEEE Trans.Nucl.Sci. **51** (2004) 960–967.

[32] G. Sprachmann, *Aging and gas filtration studies in the ATLAS transition radiation tracker*, .

- [33] P. Cwetanski, *Straw performance studies and quality assurance for the ATLAS transition radiation tracker*, .
- [34] ATLAS TRT Collaboration Collaboration, E. Abat et al., *The ATLAS Transition Radiation Tracker (TRT) proportional drift tube: Design and performance*, *JINST* **3** (2008) P02013.
- [35] ATLAS Collaboration, *Electron reconstruction and identification efficiency measurements with the ATLAS detector using the 2011 LHC proton-proton collision data*, *Eur.Phys.J.* **C74** (2014) no. 7, 2941, [arXiv:1404.2240](https://arxiv.org/abs/1404.2240) [hep-ex].
- [36] ATLAS Collaboration, *Measurements of the photon identification efficiency with the ATLAS detector using 4.9 fb^{-1} of pp collision data collected in 2011*, *ATLAS-CONF-2012-123*.
- [37] M. Cacciari, G. P. Salam, and G. Soyez, *The Anti- $k(t)$ jet clustering algorithm*, *JHEP* **0804** (2008) 063, [arXiv:0802.1189](https://arxiv.org/abs/0802.1189) [hep-ph].
- [38] *et al.* L. Carminati, *Measurement of the isolated di-photon cross section in 4.9 fb^{-1} of pp collisions at $\sqrt{s} = 7 \text{ TeV}$ with the ATLAS detector*, Tech. Rep. ATL-COM-PHYS-2012-592, CERN, Geneva, May, 2012.
- [39] Gaiser, J.E., *Appendix-F Charmonium Spectroscopy from Radiative Decays of the J/Ψ and Ψ -Prime*. PhD thesis, Stanford University, August, 1982.
- [40] W. V. *et al.*, *The RooFit Toolkit for Data Modelling*, Available from <http://roofit.sourceforge.net> or with recent versions of the root framework available at <http://root.cern.ch>.
- [41] F. James and M. Roos, *MINUIT-a system for function minimization and analysis of the parameter errors and correlations*, *Comput. Phys. Commun.* **10** (1975) no. 6, 343–67.
- [42] K. Arnold *et al.* [arXiv:1107.4038](https://arxiv.org/abs/1107.4038) [hep-ph].
- [43] K. Arnold *et al.* [arXiv:1207.4975](https://arxiv.org/abs/1207.4975) [hep-ph].
- [44] J. Alwall, M. Herquet, F. Maltoni, O. Mattelaer and T. Stelzer *JHEP* **1106** (2011) 128.
- [45] A. L. Read, *Presentation of search results: The $CL(s)$ technique*, *J.Phys.* **G28** (2002) 2693–2704.

[46] *VBFNLO utility to calculate form factors, version 1.2.1*, <http://www.itp.kit.edu/vbfnloweb/wiki/doku.php?id=download:formfactor>.

[47] L. Collaboration, *Study of the $W^+W^-\gamma$ process and limits on anomalous quartic gauge boson couplings*, Phys.Lett. **B527** (2002) 29–38, [arXiv:0111029](https://arxiv.org/abs/0111029) [hep-ex].

[48] D0 Collaboration Collaboration, V. M. Abazov et al., *Search for anomalous quartic $WW\gamma\gamma$ couplings in dielectron and missing energy final states in $pp\bar{p}$ collisions at $\sqrt{s} = 1.96$ TeV*, Phys.Rev. **D88** (2013) 012005, [arXiv:1305.1258](https://arxiv.org/abs/1305.1258) [hep-ex].

[49] CMS Collaboration Collaboration, S. Chatrchyan et al., *Study of exclusive two-photon production of W^+W^- in pp collisions at $\sqrt{s} = 7$ TeV and constraints on anomalous quartic gauge couplings*, JHEP **1307** (2013) 116, [arXiv:1305.5596](https://arxiv.org/abs/1305.5596) [hep-ex].

[50] CMS Collaboration Collaboration, *A Search for $WW\gamma$ and $WZ\gamma$ production in pp Collisions at $\sqrt{s} = 8$ TeV.*, Tech. Rep. CMS-PAS-SMP-13-009, CERN, Geneva, 2013.

[51] *VBFNLO aQGC conventions*, <http://www.itp.kit.edu/vbfnloweb/wiki/doku.php?id=documentation:details:aqgc>.

[52] O. C. G. Abbiendi et al.. Phys Rev D70 (2004) 032005.

[53] CMS Collaboration Collaboration, *A Search for $WW\gamma\gamma$ and $WZ\gamma\gamma$ production in pp Collisions at $\sqrt{s} = 8$ TeV.*, Tech. Rep. CMS-PAS-SMP-13-009, CERN, Geneva, 2013.

[54] ATLAS Collaboration Collaboration, G. Aad et al., *Evidence for Electroweak Production of $W^\pm W^\pm jj$ in pp Collisions at $\sqrt{s} = 8$ TeV with the ATLAS Detector*, Phys.Rev.Lett. **113** (2014) no. 14, 141803, [arXiv:1405.6241](https://arxiv.org/abs/1405.6241) [hep-ex].

[55] CMS Collaboration Collaboration, V. Khachatryan et al., *Study of vector boson scattering and search for new physics in events with two same-sign leptons and two jets*, [arXiv:1410.6315](https://arxiv.org/abs/1410.6315) [hep-ex].

[56] D. Damazio, T. Kono, F. Monticelli, and G. Pasztor, *Performance of the ATLAS Electron and Photon Triggers in $p\text{-}p$ Collisions at $\sqrt{s} = 8$ TeV in 2012*, Tech. Rep. ATL-COM-DAQ-2013-121, CERN, Geneva, Oct, 2013.

- [57] *et al.*. H. Abreu, *Measurement of isolated di-photon cross section in pp collision at $\sqrt{s} = 7$ TeV with the ATLAS detector*, Tech. Rep. ATL-COM-PHYS-2011-301, CERN, Geneva, Mar, 2011.
- [58] ATLAS Collaboration Collaboration, G. Aad et al., *Jet energy measurement and its systematic uncertainty in proton-proton collisions at $\sqrt{s} = 7$ TeV with the ATLAS detector*, [arXiv:1406.0076 \[hep-ex\]](https://arxiv.org/abs/1406.0076).
- [59] ATLAS Collaboration Collaboration, G. Aad et al., *Performance of Missing Transverse Momentum Reconstruction in Proton-Proton Collisions at 7 TeV with ATLAS*, *Eur.Phys.J.* **C72** (2012) 1844, [arXiv:1108.5602 \[hep-ex\]](https://arxiv.org/abs/1108.5602).

Biography

Date and place of birth: Dec.27.1987, Linyi, China
Phone: (919) 697-8230
Email: ml149@duke.edu

Education

- PhD program, Duke University 08/2009-01/2015.
- CERN summer student program 2008.
- B.S. Physics, Shandong University, 2009.

Employment

- PhD program, Duke University 2009–now.
- CERN summer student program 2008.

Awards, scholarships

- International Research Travel Fellowship 2013-2014, Duke University Graduate School.
- Dissertation Research Travel Award 2013-2014, Duke University Graduate School.
- Outstanding student scholarship 2005-2009, Shandong University.